Graph-Theoretical Approaches for Digital Discoveries in Quantum Optics

by

Tareq Jaouni

Thesis submitted to the University of Ottawa
in partial fulfillment of the requirements for the degree of
Master of Science
in
Physics

Ottawa-Carleton Institute of Physics
Department of Physics
University of Ottawa

Abstract

We present a theoretical study that investigates the applicability of a graph theoretical approach to realize various quantum experiments. Crucially, we may represent quantum optical experiments involving tabletop optical elements in terms of highly interpretable, coloured, weighted multi-graphs. We introduce the formalism behind this approach; then through the digital discovery framework PyTheus, we uncover over 100 different quantum experiments which realizes complex, novel quantum states. Towards enhancing our interpretation of the AI-based framework's solutions, we also leverage eXplainable-AI (XAI) techniques from computer vision to investigate what a trained neural network learns about quantum experiments. Crucially, we find that we are able to conceptualize the learned strategies which the neural network applies to optimize for a target quantum property, and discover how the network conceives of its solution. We conclude by presenting an experimental proposal which yields realizable solutions that, for the first time, solves high-dimensional variants of a quantum retrodiction puzzle known as the Mean King's Problem. We, therefore, present a case study which investigates the potential for new scientific discoveries through a joint collaboration between human and artificial intelligence.

Acknowledgements

My first interaction with my supervisor, Prof. Ebrahim Karimi, was during his undergraduate course on electrodynamics. Of the words that would describe me, 'proactive' and 'outgoing' would not be among them: I was a quiet person, even at the best of times, and although he had this unnatural ability to somehow make a three-hours-long lecture about electromagnetism engaging (or basically anything tangentially related to quantum optics, as I would come to learn throughout my graduate studies), I nevertheless had my difficulties in participating in-class, a ubiquitous constant throughout nearly all of my courses. I had banked on the possibility that my academic performance would solely get me noticed. Unsurprisingly, it didn't work, save for one exception. This exception is the reason why I am here to present the work therein, so I would like to thank my supervisor for taking that chance on me!

I acknowledge the financial support of the Canada Research Council (CRC) and of the National Sciences and Engineering Research Council of Canada (NSERC).

I would like to give my thanks to the previous and current members of the Structured Quantum Optics (SQO) group for fostering an engaging space for scientific discussions, and for corrupting me to the dark side of espresso. In particular, I would like to thank Xiaoqin Gao, Francesco Di Colandrea, and Manuel Ferrer for their insightful feedback on the thesis (I would also like to thank Manuel Ferrer for the figures showcasing the optical elements). I would also like to give special thanks to my interim supervisor, Prof. Mario Krenn, and the group members of the Artificial Scientist Lab (ASL) group for their continued support and guidance, even well after my departure from Germany, and for enlightening me on the intersection of physics and artificial intelligence.

I would like to thank my family for their support and for being my constant haven throughout my degree.

My experience as a Master's student offered me a chance to meet so many people from different backgrounds around the world. However slight were our interactions, I would like to thank everyone for sharing their experiences with me!

Statement of originality and collaborative contributions

The author hereby certifies that this thesis is entirely his own original work except where otherwise indicated. He further declares that the work described in this Master's thesis constitutes original research in the field of physics. He is aware of the University of Ottawa regulations concerning plagiarism, including those regarding consequent disciplinary actions. Any use of the works of any other author, in any form, is properly acknowledged at their point of use.

We provide the collaborative contributions of each participant for every chapter.

M. K. initiated the work of Chapter 2. M.K., S.A., and C.R-G., initialized the work on 100 experiments. T. J. formalized the section on quantum measurements and contributed to the manuscript of the two- and three-dimensional Mean King's Problem. S.A., C.R-G. and J. P. maintained the PyTheus coding framework. All authors contributed to the text of the manuscript and discussed the results.

M.K. and T.J. initiated the work of Chapter 3. T. J., C.R-G, and S.A. designed the code and carried out the analysis of the results. All authors contributed to the text of the manuscript and discussed the results.

E. K. initiated the work of Chapter 4. T. J., X. G., and S. A. formalized the generalized scheme to the high-dimensional Mean King's Problem. T.J. designed the code and carried out the analysis of the results. All authors contributed to the text of the manuscript and discussed the results.

N.D., A.D., and E.K. conceived the idea and devised the experiment. N.D., under the supervision of A.D., performed the experiment and analyzed the data. N.D. and T.J. performed the theoretical simulations. E.K. supervised the project. A.D., N.D., and T.J. prepared the first draft of the manuscript. All authors discussed the results and the final version of the manuscript.

CV

Publications

Jaouni, Tareq, Xiaoqin Gao, Sören Arlt, Mario Krenn, and Ebrahim Karimi. "Experimental Solutions to the High Dimensional Mean King's Problem." *Optica Quantum 1 (2)* (2023): 49 - 54

Jaouni, Tareq, Sören Arlt, Carlos Ruiz-Gonzalez, Ebrahim Karimi, Xuemei Gu, and Mario Krenn. "Deep Quantum Graph Dreaming: Deciphering Neural Network Insights into Quantum Experiments." *Machine Learning: Science and Technology 5 (1)* (2024): 015029

Ruiz-Gonzalez, Carlos, Sören Arlt, Jan Petermann, Sharareh Sayyad, **Tareq Jaouni**, Ebrahim Karimi, Nora Tischler, Xuemei Gu, and Mario Krenn. "Digital Discovery of 100 Diverse Quantum Experiments with PyTheus." *Quantum 7* (2023): 1204

Dehghan, Nazanin, Alessio D'Errico, **Tareq Jaouni**, and Ebrahim Karimi. "Effect of Aberrations on 3D Optical Topologies." *Communication Physics 6 (1)* (2023): 357

Table of Contents

List of Figures

Chapter 1

Introduction

1.1 Overview

The twentieth century saw scientists gradually unearth the various properties of Quantum Mechanics: the principles of superpositions of quantum states, the disturbances of measurement, and quantum entanglement – 'spooky action at a distance' [2]. These principles helped explain phenomena at the microscopic level not previously achieved in the classical sense, while bringing forth a new class of technologies that could achieve the impossible. At the heart of the latter is that of Quantum Information Processing (QIP): whereas the classical analogue to this encodes information in a bit, which may be found in a deterministic state of 0 or 1, QIP represents information in terms of some physical degree of freedom (DOF), usually from a quanta such as electrons or atoms, which finds information encoded in a superposition of many possible states. This has since enabled the development of various technologies that leverage these esoteric properties, such as Quantum Communication [3], Quantum Computing [4], Quantum Simulation [5], and Quantum Metrology [6], to name a few.

The photon is the quanta that forms the crux behind modern QIP tasks. They are fast, environmentally robust, and do not decohere. Information remains encoded in a photon, even over vast distances [7, 8]. Moreover, the photon possesses various possible DOFs, such as path and temporal modes, and the photon's spin and orbital angular momentum, on which information can be encoded. The majority of these DOFs are particularly enticing as we may represent information in a theoretically unbounded number of ways, which increases the photons' information capacity while also making it more robust to noise [9]. This makes various QIP phenomena realizable in the lab through arrangements of

tabletop, linear optical elements (LOEs). Interest in QIP over the past few decades has led to the discovery of increasingly complicated processing tasks and, with it, proportionally elaborate permutations of LOEs required to realize these tasks.

Here, we explore a promising graph-theoretical method to navigate the vast combinatorical space of quantum optical experiments required to solve new challenges in QIP. As we shall see in Chapter 2, we find that we may express any experiment utilizing LOEs and probabilistic pair sources (such as beamsplitters or nonlinear processes) in terms of coloured, weighted multi-graphs [10, 11]. Assisted by the digital discovery framework PyTheus, we come up with 100 different novel quantum experiments for various interesting tasks. We also exploit the readily interpretable nature of these representations to determine if we may discover new physics from the framework's discoveries. In chapter 3, we demonstrate preliminary results for an interpretability tool that utilizes the *deep dreaming* technique from computer vision to discover what an artificial neural network learns about quantum experiments. In chapter 4, we collaborate alongside PyTheus to discover first-of-their-kind experimental solutions to a quantum retrodiction puzzle known as the Mean King's Problem. We give some concluding remarks on this new representation's practicality in Chapter 5.

1.2 Description of Quantum States

We begin by introducing the density matrix formulation for a quantum system S. Quantum states ψ are themselves vectors, which we represent in Dirac notation as $|\psi\rangle$. Let $\{\ |\psi_i\rangle\}$ denotes a set of orthonormal states, i.e. $\langle\psi_i|\psi_j\rangle = \delta_{i,j}$, in which we may find the quantum system. Let p_i denote the probability that we find the system in a state $|\psi_i\rangle$ such that $\sum_i p_i = 1$. Then we define the *density matrix representation* of the quantum system by,

$$\rho = \sum_i p_i \left|\psi_i\right\rangle \left\langle\psi_i\right| . \tag{1.1}$$

In other words, we may generally describe a quantum system as a statistical ensemble of quantum states.

We can also describe *multipartite systems* – an n-fold composition of quantum systems – in terms of the density matrix formulation. Let us consider, for instance, a bipartite quantum system $S^{AB} = S^A \otimes S^B$. Let $\mathcal{H}_A$ and $\mathcal{H}_B$ refer to the *Hilbert spaces* in subsystems A and B, and let $\{\ |\psi_i\rangle\}$ and $\{\ |\varphi_i\rangle\}$ denote orthonormal bases in $\mathcal{H}_A$ and $\mathcal{H}_B$, respectively.

We may define a state, ρ^{AB}, as

$$\rho^{AB} = \sum_{i,j} p_{i,j}(|\psi_i\rangle \langle\psi_i| \otimes |\varphi_j\rangle \langle\varphi_j|). \tag{1.2}$$

.

Let us define the *partial trace* over a subsystem A as

$$\rho^A \equiv \mathrm{tr}_B(\rho^{AB}) = \sum_j \langle\varphi_i| \rho^{AB} |\varphi_i\rangle . \tag{1.3}$$

That is, ρ^A, as well as, $\rho^B = \mathrm{tr}_A(\rho^{AB})$ denote the density matrix representation in S^A and S^B, respectively. We may, therefore, represent the bipartite system as a *convex combination* of quantum states

$$\rho^{AB} = \sum_{i=0} p_i(\rho^A \otimes \rho^B). \tag{1.4}$$

The notation to arbitrarily multipartite systems, where we consider many subsystems $S^{A_1}, S^{A_2}, ...$, can be defined as a

$$\rho^{A_1,A_2,\cdots} = \sum_{i=0} p_i(\rho^{A_1} \otimes \rho^{A_2} \otimes \rho^{A_3} ....). \tag{1.5}$$

Having motivated the density matrix representation of quantum states, we can now define *pure* and *mixed* states. Let us consider,

$$\begin{aligned} \mathrm{tr}(\rho^2) &= \mathrm{tr}(\sum_{i,j} p_i p_j |\psi_i\rangle \langle\psi_i|\psi_j\rangle \langle\psi_j|) \\ &= \sum_{i,j} p_i p_j |\langle\psi_i|\psi_j\rangle|^2 \\ &\leq \sum_{i,j} p_i p_j \langle\psi_i|\psi_i\rangle \langle\psi_j|\psi_j\rangle = 1, \end{aligned} \tag{1.6}$$

where in the last line we invoked the Cauchy-Schwartz inequality. If $\psi_i = \psi_j$ for all *i,j* then $\mathrm{tr}(\rho^2) = 1$ and we say that the state is **pure**. Specifically, the quantum system can be described in terms of a single state, $\rho = |\psi_i\rangle \langle\psi_i|$. Otherwise, $\mathrm{tr}(\rho^2) \leq 1$ and the state is **mixed**. In other words, the system is described by a probabilistic mixture of quantum states much more akin to the generic form as equation (1.2). We stress that the latter case

is more often encountered in nature due to quantum noise, which is introduced from the system's interaction with the environment [8, 12].

We may also quantify two quantum states' closeness to one another. Let ρ and σ denote the respective density matrices of two quantum systems, then, according to [13], we define their **fidelity** as

$$F(\rho, \sigma) = \left(\mathrm{Tr}(\sqrt{\rho^{1/2}\sigma\rho^{1/2}}) \right)^2. \tag{1.7}$$

In particular, if ρ and σ are pure states described respectively by $|\psi\rangle$ and $|\phi\rangle$, then the fidelity is

$$F(|\psi\rangle, |\phi\rangle) = |\langle\psi|\phi\rangle|^2. \tag{1.8}$$

1.3 Projective Measurement

Let us consider a Von Neumann observable described by the positive hermitian matrix M, that is diagonalized by its set of eigenvectors $|m\rangle$. More specifically,

$$\hat{M} = \sum_m m\,|m\rangle\langle m|, \tag{1.9}$$

where m is a corresponding eigenvalue. A projective measurement on the observable M acts to decompose a quantum system ρ onto the set of possible outcomes $|m\rangle$. Let $P_m = |m\rangle\langle m|$ describe the projective measurement operator onto an outcome m, then the final state after the measurement is described by

$$\frac{P_m^\dagger \rho P_m}{\sqrt{\mathrm{Tr}(\rho P_m)}} = \frac{P_m^\dagger \rho P_m}{\sqrt{\langle m|\,\psi\,|m\rangle}}. \tag{1.10}$$

We note that the expression in the denominator, $\mathrm{tr}(\rho P_m) = \langle m|\,\psi\,|m\rangle$ is a manifestation of Born's rule, which states that the probability of measuring a quantum state is given by the modulus square of the amplitude.

1.4 Quantum Entanglement

We return to considering the composite system described by the state ρ_{AB}. For this section, let us assert that our Hilbert spaces lie in D-dimensions. If we may write the state as a

tensor product of Hilbert spaces

$$\rho_{AB} = \rho_A \otimes \rho_B, \tag{1.11}$$

then we call ρ^{AB} a *product state*. In such a state, there exists no correlations between S_A and S_B. We say that the state is separable if it can be written as a convex combination of product states. A pure state that is separable is also a product state. On the other hand, a mixed state that is seperable can be written as

$$\rho_{AB} = \sum_k p_k \rho_A^k \otimes \rho_B^k, \tag{1.12}$$

where the constitute, k^{th} terms of the state follow a probability distribution described by $\{p_k\}_{i=k}$. Through this probability distribution, we may observe classical correlations between the subsystems.

If the state ρ_{AB} is not seperable, then there exists a non-classical correlation between S_A and S_B, and the states described by each system are *entangled*. ρ_{AB} is *maximally entangled* if the reduced density matrix of its subsystems is *maximally mixed*. That is, we have for each subsystem,

$$\rho_A = Tr_B(\rho_{AB}) = \frac{\mathbb{I}}{D}. \tag{1.13}$$

This is related to the *entropy of entanglement* measure associated with composite systems: the more entangled are the particles, the less information we can attain by looking at the individual subsystems of the composite system. Indeed, one instead finds information in the correlations between these subsystems [14].

Let us consider, for example, the generalized Bell state,

$$|B_{0,0}\rangle = \frac{1}{\sqrt{D}} \sum_{i=0}^{D-1} |i\rangle \otimes |i\rangle, \tag{1.14}$$

where $|i\rangle$ form the computational basis for the D-dimensional Hilbert Spaces $\mathcal{H}_{A,B}$. Com-

puting the partial trace on the first qudit gets us

$$\begin{aligned} Tr_A(|B_{00}\rangle\langle B_{0,0}| &= \frac{1}{D}(|0\rangle\langle 0|\,\mathrm{Tr}(|0\rangle\langle 0|) + |0\rangle\langle 1|\,\mathrm{Tr}(|0\rangle\langle 1|) + |1\rangle\langle 1|\,\mathrm{Tr}(|1\rangle\langle 1|) + ...) \\ &= \frac{1}{D}\sum_{i,j}^{D-1}|i\rangle\langle j|\langle i|j\rangle = \frac{1}{D}\sum_{i,j}^{D-1}|i\rangle\langle J|\,\delta_{i,j} \\ &= \frac{\mathbb{I}}{D}, \end{aligned}$$

which shows that $|B_{0,0}\rangle$ is maximally entangled.

There exists various metrics to evaluate a state's degree of entangledenss. We concern ourselves in particular with the **concurrence** between two subsystems [15, 16, 17]. Towards generalizing to multipartite, pure systems, we follow the particular definition of [17]. A bipartite system, ρ_{AB}, is said to exhibit concurrence as

$$C(\rho_{AB}) = \sqrt{2(1 - \mathrm{Tr}(\,\rho_A^2)\,)}. \tag{1.15}$$

Let $\{S_{A_1}, S_{A_2}, \ldots, S_{A_N}\}$ denote the subsystems on which the multipartite state is defined. Then the concurrence of a state $\rho_{A_1,\ldots,A_N}$ is

$$C(\rho_{A_1,\ldots,A_N}) = \sum_{i=1}^{N} C_{A_i}(\rho_{A_1,\ldots,A_N}), \tag{1.16}$$

where

$$C_{A_i}(\rho_{A_1,\ldots,A_N}) = \sqrt{2(\,1 - \mathrm{Tr}(\,\rho^2_{A_1,\ldots,A_{i-1},A_{i+1},\ldots,A_N})\,)}\,, \tag{1.17}$$

where $\rho^2_{A_1,\ldots,A_{i-1},A_{i+1},\ldots,A_N} = \rho^2_{\bar{A}_i}$ is the reduced density matrix obtained by tracing out the subsystem A_i. In the limit, when the concurrence vanishes across some bipartition of subsystems $A_i|\bar{A}$, we say that the state is *separable* across this bipartition. That is, we may write

$$\rho_{A_i|\bar{A}} = \rho_{A_i} \otimes \rho_{\bar{A}}. \tag{1.18}$$

1.5 Photonic Degrees of Freedom

When it comes to bring to physical fruition high-dimensional quantum protocols, the photon offers no shortage in the number of ways through which this can be achieved, with

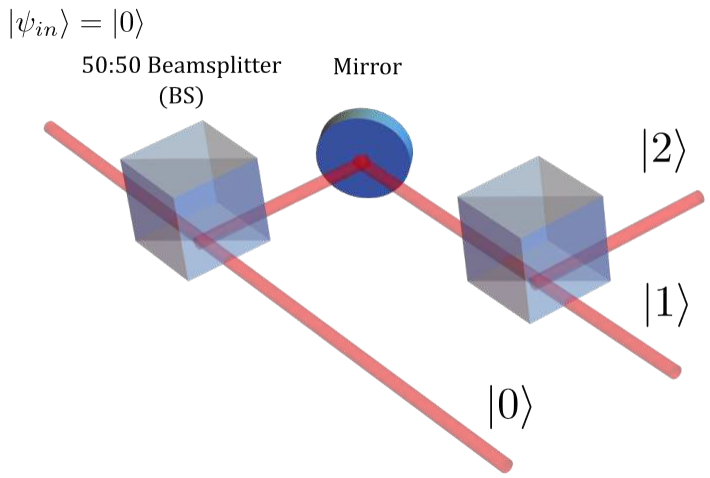

Figure 1.1: **Possible experimental setup that can encode photons to arbitrarily high dimensions in terms of path modes.** Through repeated action of a 50:50 beamsplitter, we are able to generate arbitrarily many spatially distinct paths.

physical degrees of freedom (DOFs) such as time-bin [18], and spatiotemporal modes [19] having been well-studied in this regard. For the purposes of this thesis, we focus on two particular DOFs: the photon's **path**, and the photon's **angular momentum**, which can be thought of in terms of its *spin* and *orbital* angular momentum parts.

1.5.1 Path

A photon's path simply refers to the different spatially separable paths that a photon may take. We may consider, for example, the situation outlined in Figure 1.1. A photon described by the pure state $|\psi\rangle = |0\rangle$ is incident on a 50:50 beamsplitter, whose action is to probabilistically distribute the photon onto one of two possible paths: either the photon passes straight through, remaining in the path mode $|0\rangle$, or it is reflected onto a new path $|1\rangle$. More succinctly, we may write

$$\hat{BS}\,|j\rangle \rightarrow \frac{1}{\sqrt{2}}(|j\rangle + |j+1\rangle),$$

where $|j\rangle$ stands for photon at path j. One may, therefore, generate arbitrarily many different paths and, therefore, encode the photon onto arbitrarily high paths by placing a

beamsplitter onto each new path.

1.5.2 Optical Angular Momentum

Following the treatment by [20, 21], let us consider a uniformly polarized beam of photons having electric field **E**, and a magnetic field **B**. We may represent the beam in the Lorentz gauge with the vector potential **A**,

$$\mathbf{A} = \hat{e}\, u(\mathbf{r}_\perp, z) e^{-ikz}, \tag{1.19}$$

where $k = \frac{2\pi}{\lambda}$ is the photon's wave number, $\mathbf{r}_\perp$ refers to a choice of transverse spatial coordinates and $u(\mathbf{r}_\perp, z)$ is a complex scalar function, and $\hat{e}$ is the polarization vector of the field. We may either assign a linear polarization in the $\hat{e} = \hat{x}$ or $\hat{y}$ directions, or the photon may possess circular polarization according to $\hat{e} = \frac{1}{\sqrt{2}}(\hat{x} - (\sigma_z) i\hat{y})$. In the case of the latter, we may assert that the photon has **spin angular momentum (SAM)** with a spin of $\sigma_z = \pm 1$. This polarization vector serves to encode the photon's **polarization mode DOF**.

The complex scalar amplitude, $u(\mathbf{r}_\perp, z)$, solves the **paraxial wave equation**, which is given as

$$(\nabla_\perp^2 - 2ik\frac{\partial}{\partial z})\mathbf{u}(\mathbf{r}_\perp, \mathbf{z}) = 0, \tag{1.20}$$

where $\nabla_\perp^2$ is the Laplacian operator in transverse coordinates. The scalar amplitude may take on different functional forms depending on our choice of transverse coordinates. Owing to the cylindrical symmetry of many optical components within an experimental setting, we solve the paraxial wave equation in cylindrical coordinates, $r_\perp = (r, \phi)$. The solutions to this equation are the Laguerre-Gauss (LG) modes of light, which carry Orbital Angular Momentum (OAM), given by

$$LG_{l,p}(r, \phi, z) = \frac{C_{l,p}}{w(z)} \left(\frac{r}{w(z)}\right)^{|l|} e^{-\frac{r^2}{w(z)^2}} L_p^{|l|}\left(\frac{2r^2}{w(z)^2}\right) e^{i(k(\frac{r^2}{2R(z)}+z) - \Phi(z) + l\phi)}, \tag{1.21}$$

where the integer l is known as the **azimuthal index**, whereas the non-negative integer p is known as the **radial index**, and $C_{l,p} = \frac{2^{\frac{|l|}{2}+1} p!}{(\pi(p+|l|!))^{\frac{1}{2}}}$ is a normalization constant. $w(z)$ is

the beam's radius and is given by

$$w(z) = w_0 \sqrt{1 + \left(\frac{z}{z_R}\right)^2}, \tag{1.22}$$

where $w_0 = w(0)$ is the beam's initial radius and $z_R = \frac{\pi w_o^2}{\lambda}$ is the beam's Rayleigh range. The radius of curvature, $R(z)$, is given by

$$R(z) = z\left(1 + \frac{{z_R}^2}{z}\right), \tag{1.23}$$

and the Gouy phase, $\Phi(z)$, is given by

$$\Phi(z) = (2p + |l| + 1)\arctan\frac{z}{z_R}. \tag{1.24}$$

We demonstrate the behavior of these three aforementioned functions in Figure 1.2(c).

Despite the apparent complexity of the modes, it is the azimuthal and radial indices that determines the shape of the beam. Figure 1.2 showcases what happens when we modify the indices. We see that the beam's shape and handedness are modified; in particular, we may usually encode the photon's OAM DOF in terms of the azimuthal index as $|l\rangle$. Since the azimuthal (and radial indices) are both theoretically unbounded, there are infinitely many possible encodings that can be realized (though we note that experimental realizations have thus far been bounded to l=10100 [22].) This makes the OAM a promising option to realize high-dimensional protocols over various media [9, 23, 24].

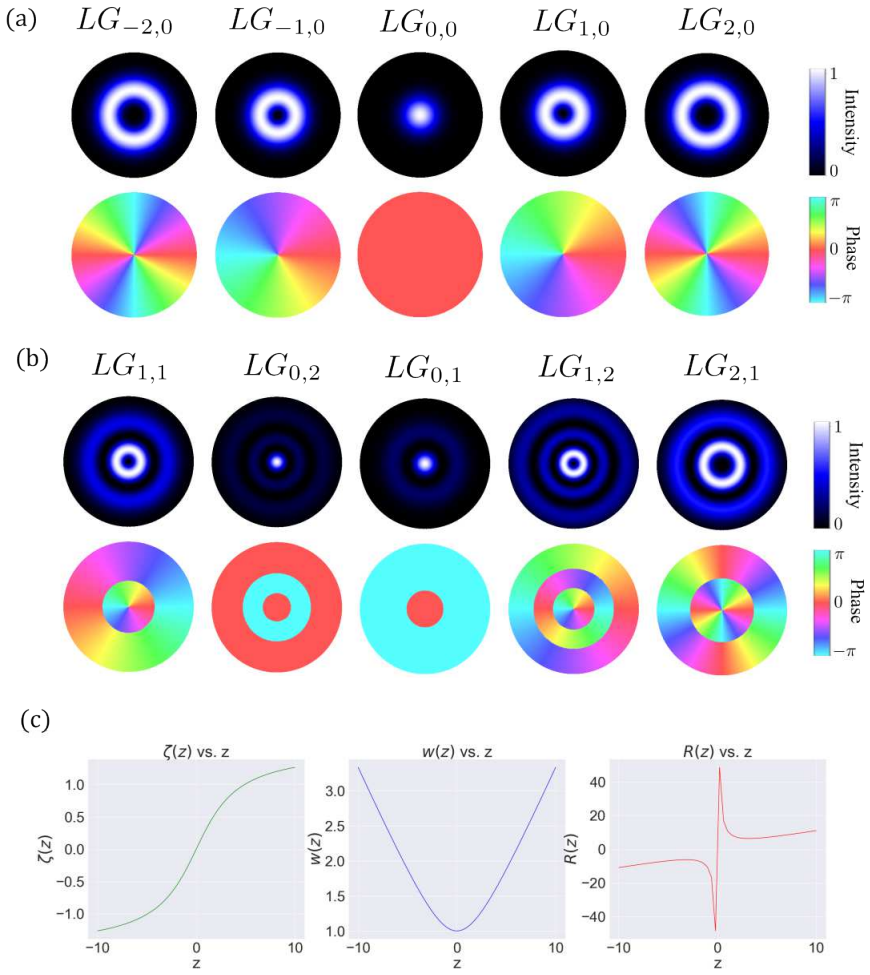

Figure 1.2: **Select examples of OAM modes.** For each example, we plot the field's (normalized) intensities and phases are plotted. In particular, we consider the effects of varying the (a) azimuthal and (b) radial modes. Note the inversion of phase in (a) between the positive and negative valued azimuthal modes. The characteristic doughnut shape of OAM modes appears in regions of undefined phases or *singularities* in which the field vanishes. (c) Plots of a Gaussian beam's Gouy Phase, $\zeta(z)$, the beam width, $w(z)$, and the radius of curvature, $R(z)$, as a function of propagation distance z.

Chapter 2

Quantum Experiments and Graphs

This chapter is based on the following publication.

Ruiz-Gonzalez, Carlos, Sören Arlt, Jan Petermann, Sharareh Sayyad, **Tareq Jaouni**, Ebrahim Karimi, Nora Tischler, Xuemei Gu, and Mario Krenn. "Digital Discovery of 100 Diverse Quantum Experiments with PyTheus." *Quantum* 7 (2023): 1204

DOI: https://doi.org/10.22331/q-2023-12-12-1204

2.1 Overview

The task of physically realizing exotic quantum phenomena, such as observing quantum entanglement for dimensions past three or generating arbitrarily multipartite states, is exacerbated in difficulty due to the vast combatorical space which accompanies the experimental design of quantum optical setups. Therefore, one may ask if the best designs lay beyond the confines of human intuition. This has prompted computed-assisted investigations in setup design [25], such as those which discover new quantum setups through evolving 'toolboxes' of setup elements [26], or by using machine learning approaches such as genetic algorithms [27] and active learning [28]. The main caveat to these methods is that the solutions found in these investigations often require additional simplifications from the human side to be made interpretable.

It was first found in 2017 by Krenn et al. [29] that one could represent quantum optical experiments bidirectionally in terms of undirected graphs $G = (V, E)$. The vertices

$V(G)$ of the graph correspond to different paths taken by a photon, while edges $E(G)$ between vertices indicate the correlation between two photons via a probabilistic pair generation event. Experimentally, if we have n detectors which each corresponds to the different photonic paths, then we condition the successful generation of the state on an n-fold detector click. In graph language, this entails finding disjoint subsets of edges known as *perfect matchings* which contains the vertices of the graph as endpoints exactly once. It was later found in [10] that we could also introduce complex-valued weights ω to the graph's edges to simulate quantum interference between states – this could be implemented experimentally through *phase shifters* – and in [30], we find that we can also colour the edges to represent different modes of some photonic DOF.

The graph-theoretic representation can be harnessed to devise experiments that observes a variety of high-dimensional, multipartite phenomena in quantum optics. Such experiments can be implemented with standard photonic technologies such as integrated photonics [31], entanglement by path identity [32], or through bulk optics, as we will illustrate in Chapter 4. Moreover, they are highly interpretable, so they lend themselves particularly well in the aforementioned context of numerical investigations. To this end, the following work introduces the PYTHON-based, Digital Discovery Framework PYTHEUS; we illustrate how it can be used to ascertain the design of one hundred quantum experiments for a variety of hereforto unrealized quantum phenomena. We also employ PYTHEUS to great effect for the theoretical investigations carried out in the following chapters.

2.2 Weight Function

We may encapsulate all the information about the quantum graph through its corresponding weight function, $\Phi(\omega)$, which maps the graph to its corresponding state $\Phi(\omega)\,|vaccum\rangle = |\Phi(\omega)\rangle$, where $|vacuum\rangle$ is a vacuum state describing no photons. Let $x, y \in V(G)$ designate the vertices of the graph G, and let $C(G)$ represent the set of possible modes or "colours" in the graph G, then we may write [33].

$$\Phi(\omega) = \sum_m \frac{1}{m!} \left(\sum_{x,y \in V(G)} \sum_{j,k \in C(G)} \omega_{x,y}^{j,k} x_j^\dagger y_k^\dagger + h.c. \right)^m . \tag{2.1}$$

Where, for example, $x_j^\dagger$ represents the creation operator for a photon in mode j and in path x, and $\omega_{x,y}^{j,k}$ represents the amplitude of the edge adjoining the vertices x, y with modes j, k. We usually only consider terms in the sum comprised of all vertices in $V(G)$,

as they correspond to the perfect matchings of the graph. The lower- and higher-order terms account for reductions in the quantum graph's experimental fidelity, since they include terms which physically correspond to partial or repeated detector clicks. For a two-dimensional, quadripartite quantum graph with vertices $V(G) = \{a, b, c, d\}$ and modes $j, k, l, m \in C(G) = \{0, 1\}$, we observe terms in the order $m = 2$ of the form $\omega^{j,k,l,m}_{a,b,c,d}(a^\dagger_j b^\dagger_k c^\dagger_l d^\dagger_m)$, where $\omega^{j,k,l,m}_{a,b,c,d} = \omega^{j,k}_{a,b}\omega^{l,m}_{c,d} + \omega^{j,l}_{a,c}\omega^{k,m}_{b,d} + \omega^{j,m}_{a,d}\omega^{k,l}_{b,c}$ represents the amplitude.

The quantum state observed by the graph is, therefore, realized through the superposition of all possible perfect matchings of the graph, as distinguished by the specification of the modes j, k, l, m (in other words, we realize the state $|j, k, l, m\rangle$) and may be denoted as $|\Phi(\omega)\rangle = \Phi(\omega)\,|vaccum\rangle$. We remark that, although finding $|\Phi(\omega)\rangle$ from the graph is straightforward, the inverse process is non-trivial as the graph representation is not unique. One possible approach is through *inverse design*: we optimize a complete quantum graph such that an objective function $\mathcal{L}$, which may correspond to a target state or property, is minimized. For example, for a target state $|\psi\rangle$, we may consider computing the *fidelity* with respect to $|\Phi(\omega)\rangle$ at each step of the optimization so that

$$\begin{aligned} \mathcal{L}(|\Phi(\omega)\rangle) &= 1 - F(|\Phi(\omega)\rangle\,, |\psi\rangle) \\ &= 1 - |\langle\langle\Phi(\omega)||\psi\rangle\rangle|^2, \end{aligned} \tag{2.2}$$

and removing edges from the graph, which minimally contribute towards optimizing the objective.

2.3 Multipartite Entangled States

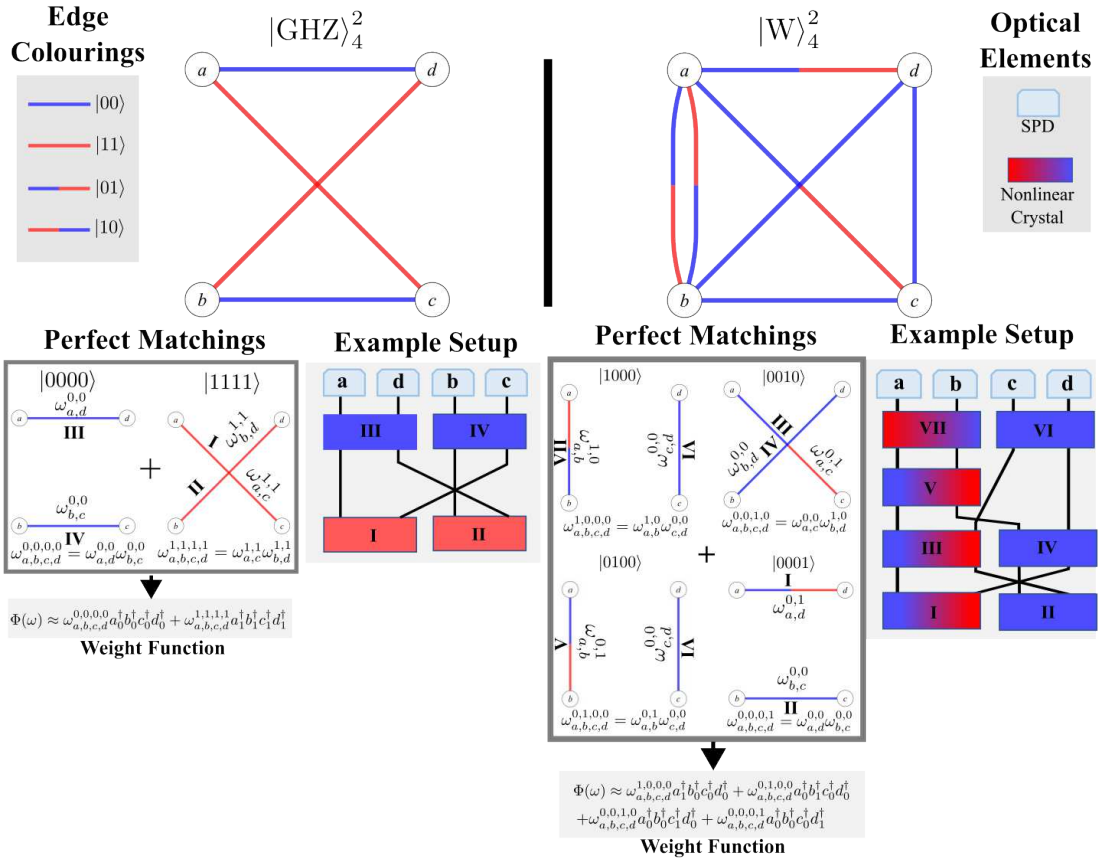

Figure 2.1: **Quantum graph representations corresponding to the GHZ and W states.** We show the full graph as well as the relevant perfect matchings. Each perfect matching contributes a term in the graph's corresponding weight function (*without normalization*), with the term's amplitude equal to the product of weights of edges that makes up the perfect matching. We also show the corresponding experimental setup based on entanglement by path identity. Edges between vertices correspond to the probabilistic firing of correlated photon pairs from nonlinear crystals. We enumerate each edge by its corresponding crystal in the experimental setup. The crystals are coloured to indicate the photon pair modes on which we post select after generation. A crystal that is entirely blue, for example, probabilistically selects the correlated state $|00\rangle$; in the experiment, we concern ourselves only with instances where this event occurs

As a case study on how we may utilize quantum graphs to generate states, we consider two particular classes of multipartite quantum entanglement. The Greenberger-Horne-Zellinger (GHZ) States, named after by the authors of the same name [2], were proposed as an extension to Bell's Theorem in the "superclassical" EPR case in which one can make definite predictions on a measurement of a particle's mode and sees application for high-dimensional, multipartite entanglement. In d-dimensions and N particles, it is defined as follows.

$$|\mathrm{GHZ}\rangle_N^d = \frac{1}{\sqrt{d}} \sum_d |d\rangle^{\otimes N} . \tag{2.3}$$

For example, the quadripartite GHZ state, $|\mathrm{GHZ}\rangle_4^2$, is defined as

$$|\mathrm{GHZ}\rangle_4^2 = \frac{1}{\sqrt{2}}(|0000\rangle + |1111\rangle).$$

Another class of multipartite states that are admissible as proof to Bell's inequality are the W states [34]. We may define a generic W state by

$$|\mathrm{W}\rangle_N^d = \frac{1}{\sqrt{N}}(|1\rangle \otimes (|0\rangle)^{N-1} + |0\rangle \otimes |1\rangle \otimes |0\rangle^{N-2} + ...). \tag{2.4}$$

For example, the quadpartite W state in two dimensions, $|\mathrm{W}\rangle_4^2$, is

$$|\mathrm{W}\rangle_4^2 = \frac{1}{\sqrt{N}}(|1000\rangle + |0100\rangle + |0010\rangle + |0001\rangle). \tag{2.5}$$

Figure 2.1 shows the corresponding graphical representation of a setup that may realize these states, along with their corresponding weight functions. The suggested setup takes inspiration from entanglement by path identity [32], in which the state is considered to be generated on the probabilistic firing of indistinguishable photons from coherently pumping light into specific pairs of crystals. For example, we realize one perfect matching on the GHZ state only if crystals I and II or crystals III and IV fire at the same time; in either case, this results in a fourfold detector click event. If, on the other hand, our coherent pumping excites crystals I and IV, then only three of the four detectors – a, b, and c – will trigger simultaneously.

2.4 Quantum Measurement

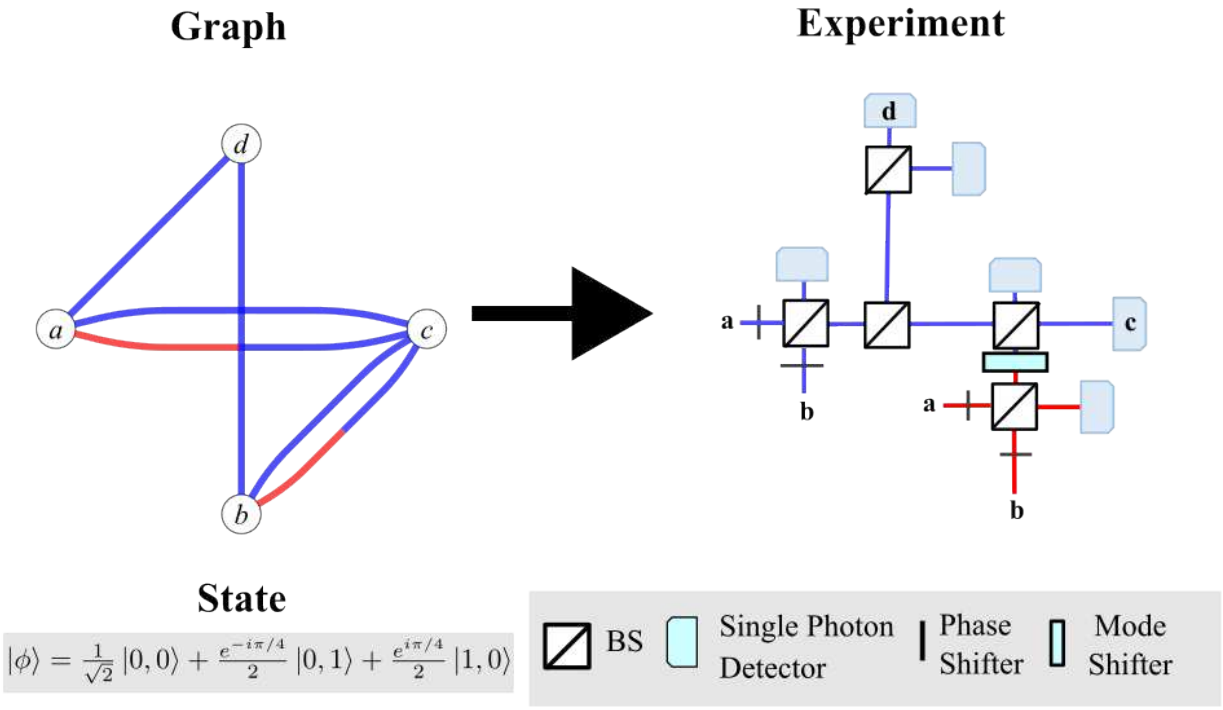

Figure 2.2: **Possible experiment for a projective measurement on $|\phi\rangle$ (see equation 2.6.)** To obtain the graph, we turn to PyTheus to optimize for the target state under the usual topological constraints specific to quantum measurements. Following Klyshko's AWP, we may chart a direct path from the input vertices a, b to the detector vertices c, d. We may encode the complex-valued weights, which are implicit in the graph, using combinations of phase shifters and beam splitters.

We have shown how to interpret quantum graphs for the creation of states, but it is possible to adapt this representation to other QIP tasks. As we will illustrate in chapter 4, we may also look to quantum graphs to represent projective measurements. While we heretofore viewed edges between vertices a and b to indicate the creation of correlated photon pairs, we may alternatively view this as a deterministic single-photon generation event. We base this on *Klyshko's Advanced Wave Picture (AWP)*, introduced in [35, 36] and observed experimentally in [37, 38]: let us suppose that we measure the coincidence detection of two photons in arbitrary modes ψ_1 and ψ_2 respectively and retrieve the joint probability

distribution $\mathcal{P}(\psi_1, \psi_2)$ out of our detections. Klyshko argues that we may obtain the same probability distribution by replacing, for example, the detector for ψ_1 with a source which creates a photon of mode ψ_1, replacing the crystal with a mirror, and allowing the photon to reflect towards detector ψ_2. We, therefore, retrieve the conditional probability distribution $\mathcal{P}(\psi_2|\psi_1) = \mathcal{P}(\psi_1, \psi_2)$ that we find the emitted photon in ψ_2, given that it was initially in ψ_1. In the quantum graphs picture, we may consider an edge which adjoins an "input" vertex a to a detector vector b. Following the AWP, this now corresponds to a direct path from photon to detector.

Let $\rho_{in} = |\psi_{in}\rangle \langle\psi_{in}|$ denote an incoming state. In principle, a quantum graph directly implements the projective measurement $P_0 |\psi_{in}\rangle P_0^\dagger + P_1 |\psi_{in}\rangle P_1^\dagger$, where $P_0 = |\phi\rangle \langle\phi|$ for a given state $|\phi\rangle$. Consider, for example, one of the two-dimensional Vaidman-Albert-Aharanov states [39]

$$|\phi\rangle = \frac{1}{\sqrt{2}} |00\rangle + \frac{e^{-i\pi/4}}{2} |01\rangle + \frac{e^{i\pi/4}}{2} |10\rangle . \tag{2.6}$$

Figure 2.2 demonstrates a possible quantum graph, along with the corresponding experimental setup, which implements the projective measurement. We topologically constrain the graph such that any edges between input vertices are excluded. We also flatten any higher-order modes using a mode-shifting element so that all photons arriving at the detector are indistinguishable with respect to one another. We condition the successful projection to $|\phi\rangle$ on the simultaneous click of detectors c and d. However, we can extend the projection to other states in the basis by using loss as an additional source of information. This entails placing detectors to capture sources of loss, which introduces additional possible twofold detector patterns.

Digital Discovery of 100 diverse Quantum Experiments with PyTheus

Carlos Ruiz-Gonzalez[§1], Sören Arlt[§1], Jan Petermann[1], Sharareh Sayyad[1], Tareq Jaouni[2], Ebrahim Karimi[1,2], Nora Tischler[3], Xuemei Gu[1], and Mario Krenn[1]

[1]Max Planck Institute for the Science of Light, Erlangen, Germany.
[2]Nexus for Quantum Technologies, University of Ottawa, K1N 6N5, ON, Ottawa, Canada.
[3]Centre for Quantum Computation and Communication Technology (Australian Research Council), Centre for Quantum Dynamics, Griffith University, Brisbane, Australia.

Photons are the physical system of choice for performing experimental tests of the foundations of quantum mechanics. Furthermore, photonic quantum technology is a main player in the second quantum revolution, promising the development of better sensors, secure communications, and quantum-enhanced computation. These endeavors require generating specific quantum states or efficiently performing quantum tasks. The design of the corresponding optical experiments was historically powered by human creativity but is recently being automated with advanced computer algorithms and artificial intelligence. While several computer-designed experiments have been experimentally realized, this approach has not yet been widely adopted by the broader photonic quantum optics community. The main roadblocks consist of most systems being closed-source, inefficient, or targeted to very specific use-cases that are difficult to generalize. Here, we overcome these problems with a highly-efficient, open-source digital discovery framework PyTheus, which can employ a wide range of experimental devices from modern quantum labs to solve various tasks. This includes the discovery of highly entangled quantum states, quantum measurement schemes, quantum communication protocols, multi-particle quantum gates, as well as the optimization of continuous and discrete properties of quantum experiments or quantum states. PyTheus produces interpretable designs for complex experimental problems which human researchers can often readily conceptualize. PyTheus is an example of a powerful framework that can lead to scientific discoveries – one of the core goals of artificial intelligence in science. We hope it will help accelerate the development of quantum optics and provide new ideas in quantum hardware and technology.

Carlos Ruiz-Gonzalez[§]: cruizgo@proton.me
Sören Arlt[§]: soeren.arlt@mpl.mpg.de
Mario Krenn: mario.krenn@mpl.mpg.de

Contents

[§]These authors contributed equally to this work. The order was decided by a coin flip.

1 Introduction

Photons, the individual particles of light, have long been used as the core player for fundamental experiments and applications in quantum information science [1]. Photons do not easily interact with their environments; therefore, they can be distributed over large distances – which makes them a key resource for long-distance quantum communication [2, 3] and experiments that require strict Einstein locality conditions [4–6]. Using advanced measurement-based quantum computing schemes, photons are among the most promising candidates for future quantum computers [7]. Entanglement between two or more photons can be produced without a vacuum or cooling, and therefore many advanced experimental results can be achieved directly with table-top setups. Furthermore, the bosonic nature of photons allows for the generation of complex entangled quantum states of indistinguishable photons that are a key resource for quantum-enhanced measurements [8]. These potential applications have lead to enormous technological advances in integrated chips for fast and precise control of photonic quantum states [9–12], high-quality single-photon sources [13–16], novel photon-pair sources [17], photon number resolving detectors [18, 19], and advanced high-quality multi-photon interference [20–23].

One question now is how to utilize these technologies to build up exciting new experiments for the foundations of quantum physics and practical quantum hardware.

Historically, the design of quantum experiments strongly relied on the intuition and creativity of human experts who leverage their experience and come up with blueprints of experiments. However, due to the unintuitive phenomena and enormous combinatorial space of the potential designs, it becomes extremely difficult for human researchers to discover more complex quantum setups. It might be possible that there are high-quality solutions to experimental design questions far outside of the region where humans' intuition fails. How could we possibly find such extraordinary solutions?

This question has sparked a strong interest in the automated discovery of quantum experiments with computers, overviewed in [24]. The invention of these tools for quantum optics experiments [25] have indeed overcome experimental limitations and allowed for new avenues in laboratories for entanglement research [26–29]. One crucial question is whether we can also learn something about physics from these tools. And indeed, several new concepts have been published that were purely discovered through automated design [25], such as a new general idea of entanglement structure [30], and generalized constructions of photonic quantum gates [31]. Those concepts were discovered by tedious analysis of the computer's solutions, which was time-consuming. The problem was that the algorithms were powerful enough to find unknown solutions but had no incentive to present a simple, human-understandable form of it.

This was solved by the invention of Theseus [32], an efficient algorithm for the discovery of new quantum experiments that can readily be interpreted by humans. The key insight was a shift in the representation. Rather than describing quantum experiments as quantum optical components on an optical table, experiments are described as graphs of correlations between photons. This representation, which has been a derivative of a computer-discovered concept itself, was developed in [33–35] – and allows working with a much more natural representation, which can be translated back at any point to an experiment consisting of optical elements. (It should be noted that the representation is independent of photonic graph states for measurement-based quantum computing [36–38], and it is so far unknown how to translate among them.)

In this paper, we introduce PyTheus[2], a highly-efficient, open-source, automated design and discovery framework for quantum optics experiments. At the core, PyTheus uses a much extended graph-based representation of quantum optics, which allows us not only to represent entanglement and quantum gates, but lets us design quantum measurements, quantum communication protocols, optimize experimental properties, and discover quantum systems that involve single-photon sources, mixed states, and states entangled in the photon-number basis. Besides the advances of the scientific scope, we note that PyTheus is written in Python, and therefore can readily be combined with machine learning frameworks such as TensorFlow and PyTorch, and allows for immediate parallelization in computer clusters.

To showcase the applicability of PyTheus, we demonstrate the discovery of 100 previously unknown or advanced implementations of quantum optics experiments, ranging from exciting new systems for entanglement research to quantum states from condensed matter physics that are interesting for quantum simulation purposes, new ways of performing quantum communication tasks such as entanglement swapping, new quantum state measurements, and quantum gates. The experiments can involve both probabilistic photon sources and deterministic single-photon sources, and many of them are readily implementable in today's modern quantum optics labs. In the GitHub repository, we present the instructions for PyTheus that discover each of the examples. We hope that PyTheus's efficiency, generality, and low entry barrier kick-starts the application of computer-discovered quantum setups in experimental laboratories worldwide, and inspires new exciting computer-inspired ideas and directions for fundamentals and applications of photonic quantum physics research.

While the goal of this paper was to demonstrate the discovery capability of PyTheus, in several cases, it was impossible *not* to *see* clear generalizations and reasons why the solutions work. We show this in some cases below. One of the exceptionally interesting concepts we discovered was a new quantum multiphoton interference effect that can simulate probabilistic multipair sources just with photon pairs. We describe this new physics concept and its application in a parallel paper [39].

The article is structured in the following way: In section 2, we introduce the graph-based representation of quantum optics, which lies at the heart of PyTheus. In section 3, we introduce the idea of the computational PyTheus framework, which we then apply to the discovery of 100 new quantum experiments in section 4. In section 5, we explain some future(istic) ideas that might lie ahead of us.

1.1 Related Work

The first automated and artificial-intelligence-driven design methods for new quantum experiments were introduced in 2016 (for a more detailed review on the topic see [24, 40]). One of them, Melvin , was focused on specific photonic quantum information tasks such as quantum state generation and quantum transformations, using discrete learning techniques [25]. The second one, *Tachikoma*, focused on the discovery of new experimental setups for quantum metrology tasks and used genetic algorithms for discrete optimization [41]. *Tachikoma* has been expanded to incorporate neural network surrogate models to speed up the search process for new quantum-enhanced measurements [42, 43]. At the same time, the ideas of Melvin have led to numerous implementations of experiments in various laboratories [26–29] and the extraction of new ideas and concepts in quantum physics [30, 31]. Automated design tools have helped to build new ways to perform quantum information tasks such as quantum cloning [44]. Compared to these tools, PyTheus does not work on the discrete search space. Discrete spaces are very challenging to navigate as gradients cannot be used. Rather, PyTheus uses domain knowledge in the form of a new physics-inspired representation that is entirely continuous.

These ideas have later been expanded by using reinforcement-learning [45, 46], for quantum communication [47, 48], recurrent neural networks [49], and deep generative models such as variational autoencoders [50] or logical AI [51]. Compared to these tools, PyTheus uses direct optimization on the outputs of a physical simulator

[2] GitHub: https://github.com/artificial-scientist-lab/PyTheus

and does not rely on learned simulators or strategies. That makes it significantly faster.

Various quantum physics groups and companies have also developed simulators and optimizers since. A main focus there is on the design of experimental settings for photonic quantum computing [52–55]. One remarkable simulator is *Strawberryfields* [53], which is focused on design and optimization tasks for continuous-variable photonic quantum computing and quantum machine learning tasks. Recent updates include auto-differentiation which significantly speeds up the rate of optimization. A related software package is [56], which allows for fast computation of tasks related to Gaussian boson sampling. Compared to these tools, the focus of PyTheus is different. PyTheus is built for discrete-variable quantum optics, and not targeted to photonic quantum computing (or boson sampling tasks). Furthermore, one main motivation is the interpretability of the discovered results, which is achieved via a topological optimization on the graph-based representation.

An alternative methodology that focuses not only on the design question but also on understanding the underlying physical concepts is Theseus [32]. There, the algorithm employs a graph-based representation to describe photonic experiments, and the final results are topologically simplified graphs that can be interpreted and conceptualized in a much more straightforward way than representations that work directly on the optimization of optical elements. Compared to Theseus, PyTheus expands this idea and applies it to many new situations, inaccessible before, such as the design of quantum measurement and communication setups via the Choi–Jamiołkowski isomorphism.

Related work has shown how quantum computers could overcome the enormous computational of designing quantum optical hardware [57]. PyTheus relies, for now, on classical computers, but recent hardware advances might enable the execution of tools like PyTheus on quantum hardware [58].

2 Graphs and Quantum Experiments

The connection between quantum optical experiments and graph theory was discovered a few years ago [33–35] and has been further developed as a design algorithm Theseus for new quantum experiments [32]. In the graph-experiment representation, each colored weighted graph corresponds to a quantum experimental setup, and *vice versa*. Each edge and each vertex of the graph represent a correlated photon pair and a photon path, respectively. Its complex weight denotes the amplitude of the photon pair, and the edge color represents a photon's internal mode number for a given path, which corresponds to the photon's degree of freedom such as polarization [59], path [10, 60, 12], transverse spatial modes [61–64], time-bin [65] or frequency [66, 17]. This abstract graph representation allows us to have the full information of quantum optical experiments and has been used for discovering quantum states and transformations [32]. At first glance, it might seem that there is fundamentally no difference between the path degree of freedom (which is encoded as vertices) and the internal degrees of freedom of photons (which are encoded as colors of edges). However, this is only true information theoretically. Physically, the path degree of freedom is exceptional, because it allows to add spatially separation between photons and thereby perform non-locality experiments.

Here we significantly extend the bridge be-

Graph theory		**Experiment**
color weighted graph		quantum experiment
vertex		path to photodetector
		heralded optical path*
		single photon source
		incoming photon
		ancillary photodetector
		number resolving detector
		environment interaction
edge	color	internal mode number
	weight $\in \mathbb{C}$	amplitude**
		negative amplitude
		correlated photon pair
		single photon path

Table 1: The correspondence between graph theory and quantum experiments. *For some experiments one must known the total amount of photons crossing a group of optical paths (see section 4.4). This is clarified in the graph figures with a gray envelop. **Unless the contrary is specified, all weights are real values.

tween graphs and experiments, which allows us to perform design and discovery tasks for quantum state generation (for pure and mixed states and on the photon number basis), quantum measurements, quantum communication protocols, and gates for quantum computing. In Table. 1, we show the correspondence between graph theory and quantum experiments. The graph representation can be directly translated into different experimental implementations. In the remaining part of this section, we explain how these graphs encode quantum states, and how to translate them to experimental setups.

2.1 Quantum State Generation

2.1.1 Probabilistic Photon-Pair Sources

Probabilistic photon-pair sources, which are typically based on nonlinear processes such as spontaneous parametric down conversion (SPDC) and four-wave mixing (FWM) [67], are one of the most widespread resources to generate entangled and correlated pairs of photons. A range of photonic quantum experiments using probabilistic sources can be interpreted as a weighted colored graph [32–35]. There, each vertex represents an optical path to a detector and each edge refers to the correlated photon pair produced by a probabilistic photon-pair source. The edge weight is the amplitude associated with the photons, and the edge color describes the photon's internal mode number (i.e., the degree of freedom of a photon). The connection between the graph and the corresponding quantum state is given by the weight function [32]

$$\Phi(\boldsymbol{\omega}) = \sum_m \frac{1}{m!} \left(\sum_{e \in E(G)} \omega(e) x^\dagger(e) y^\dagger(e) + \text{h.c.} \right)^m , \tag{1}$$

where $E(G)$ is the set of edges of the graph. The quantum state is obtained by applying the weight function to the vacuum, i.e. $|\psi\rangle = \Phi(\boldsymbol{\omega})\,|\text{vac}\rangle$. The term h.c. stands for hermitian conjugate, which includes annihilation operators. As an example of states using four path (i.e., a, b, c, and d) with two-dimensional internal modes (i.e., 0 and 1) in Fig. 1, the $\Phi(\boldsymbol{\omega})$ is given as

$$\Phi(\boldsymbol{\omega}) \approx \sum_N \frac{1}{N!} (\omega_{a,b}^{0,0} a_0^\dagger b_0^\dagger + \omega_{b,d}^{1,1} b_1^\dagger d_1^\dagger + \omega_{c,d}^{0,0} c_0^\dagger d_0^\dagger + \omega_{a,c}^{1,1} c_1^\dagger a_1^\dagger + \text{h.c.})^N, \tag{2}$$

where $\boldsymbol{\omega} = (\omega_{a,b}^{0,0}, \omega_{b,d}^{1,1}, \omega_{c,d}^{0,0}, \omega_{a,c}^{1,1})$ is a list of edge weights $\omega_{x,y}^{i,j} \in \mathbb{C}$ and $|\omega_{x,y}^{i,j}|^2 < 1$, the superscript and subscript represent the mode number and the optical path, respectively. $x_k^\dagger$ is the creation operator of a photon in path x with mode k. The pair-emission process is up to the N-order, and the probability of occurrence for lower-order events is higher than that of higher-order ones. In principle, the hermitian conjugate terms influence the final state. However, for the low pump regime, the effect of the annihilation terms is negligible in many cases. For example this is the case when the final state is conditioned on having a photon in every detector. In all of the examples that we present here, it is safe to neglect the annihilation operators.

An alternative method to compute these systems in a non-approximate way is to follow the Takagi decomposition (see [68], specifically Eq.27) , which leads to reliable solutions also in the strong-pump regime. Naturally, this method is more expensive to compute. In our manuscript, we do not need to use this more involved method, as the low-pump approximation holds with high accuracy. Experimentally, a common way to obtain a quantum state is to condition the experimental results on a simultaneous detection event in each detector, which is also called the n-fold coincidence detection. In our graph representation, this only happens when a subset of the edges contains each of the n vertices exactly once (see the subset of blue edges or red edges in Fig. 1), which is the so-called perfect matching of a graph. For the example in Fig. 1, we neglect the empty mode and higher-order terms $N > 2$ to post-select the quantum state. There are two perfect matchings (two blue edges and two red edges) in Fig. 1, which contribute to two quantum terms $|0000\rangle$ and $|1111\rangle$. The weight of a perfect matching is the product of all its edge weights. For each term in a quantum state, the weight is given by the sum of all weights of the perfect matchings that contribute to it. Therefore, the weights for quantum terms $|0000\rangle$ and $|1111\rangle$ are $\omega_{a,b}^{0,0}\omega_{c,d}^{0,0}$ and $\omega_{a,c}^{1,1}\omega_{b,d}^{1,1}$, respectively. In the end, a coherent superposition of the two perfect matchings in the graph leads to the post-selected quantum state, which is

$$|\psi\rangle \approx \omega_{a,b}^{0,0}\omega_{c,d}^{0,0}\,|0000\rangle + \omega_{a,c}^{1,1}\omega_{b,d}^{1,1}\,|1111\rangle\,. \tag{3}$$

If we set all weights the same and normalize the state, we can then reach a four-particle Greenberger-Horne-Zeilinger (GHZ) state.

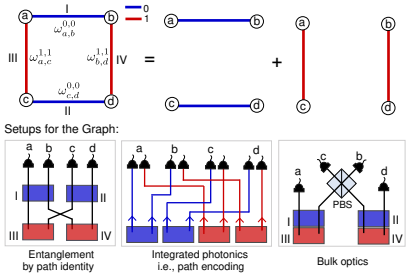

Figure 1: An abstract graph representation of quantum experiments producing GHZ states. There, edges and vertices represent correlated photon-pair and optical paths, respectively. The edge colors and weights $\boldsymbol{\omega}$ are mode numbers and complex coefficients. The blue and red colors refer to the mode numbers 0 and 1, respectively. There are two perfect matchings (i.e., a subgraph that covers all vertices only once), and their coherent superposition leads to a quantum state $|\psi\rangle = \omega_{a,b}^{0,0}\omega_{c,d}^{0,0}|0000\rangle + \omega_{a,c}^{1,1}\omega_{b,d}^{1,1}|1111\rangle$ (without normalization). We can get a four-qubit GHZ state by setting all weights equal. The graph can be translated into several quantum setups with different technologies, such as entanglement by path identity or path encoding used in integrated photonics or standard bulk optics (e.g., using polarization encoding). The squares I-IV are probabilistic sources that create photon pairs. For clearer presentation, we draw the source in the color corresponding to the mode they contribute.

Translation to Experiments – A colored weighted graph can directly be translated into several quantum optical experiments using different technologies [32], as shown in Fig. 1. The most straightforward way is applying the concept of entanglement by path identity [30, 29, 69], for which the graph representation has initially been designed [33]. In this scheme shown on the left side of Fig. 1, paths of indistinguishable photons produced from multiple crystals are overlapped, leading to a coherent superposition of possible origins for a photon. Equipped with the graph-experimental correspondence in Table 1, we now translate four edges and vertices into four photon-pair sources and optical paths. Here, we encode photon's internal mode number in polarization such that blue and red edge colors in the graph depict horizontal and vertical polarization, respectively. The four sources are set up in such a way that two sources (blue edges) produce photons with states $|00\rangle$ while the other two (red edges) produce photons with states $|11\rangle$. We then pump all sources coherently and consider that two of the four sources produce a photon pair in this example. Conditionally on perfect matching or post-selection, we have only two cases (two-photon pairs come either from the sources I and II or from the sources III and IV) that contribute to the final quantum state in Eq. (3). All other combinations of sources do not lead to only one photon in each of the detectors. For example, a photon pair in crystals I and III leads to two photons in a, one photon in b, and c, but no photon in d; therefore, this case is disregarded. If the mode numbers are indistinguishable, one can observe a new form of multi-photon interference, which has first been experimentally observed in [22, 23] and which forms the basis of many of the proposed experiments below.

Another promising technology is using integrated photonic, which usually uses path encoding [9–12], where each photon's one mode goes to one detector, as shown in the bottom middle-part of Fig. 1. In this example, each photon has two path modes depicted in blue and red colors, respectively. Therefore, one can consider that each vertex in Fig. 1 actually contains two sub-detectors that directly connect to the paths for the photon's two-mode numbers (i.e., blue and red paths). The vertex is activated when only one of the two sub-detectors clicks. In this way, perfect matching means the situations where four sub-detectors click in either blue paths or red paths, leading to the desired quantum state. Moreover, one can also use the standard bulk optics for generating photonic entanglement [70, 71]. When the edges are in the same color, which means the corresponding photons have the same mode number, one can use either probabilistic beam splitters or directly path-identified photon-pair sources to form the edge. If the edges have different colors (for example, two-mode numbers in Fig. 1), one can employ mode-dependent beam splitters such as polarizing beam splitters (PBSs) and transverse spatial mode sorters [72, 1] to create an edge. With polarization encoding in the example, we can insert a PBS between two cross-crystal sources [72], for the state generation. Yet, such a translation is not unique, and an expert may further simplify the proposed setup.

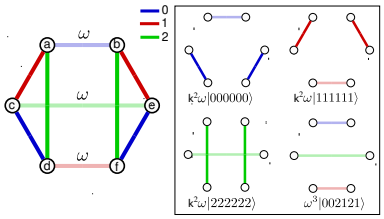

Figure 2: Asymptotic solution for quantum experiments producing a three-dimensional six-particle GHZ state. All edges have weights k but those labelled as ω. The four perfect matchings of the graph lead to the quantum state $|\psi\rangle = k^2\omega(|000000\rangle + |111111\rangle + |222222\rangle) + \omega^3 |002121\rangle$. To minimize the amplitude of the undesired term the weights must fulfill $k^2\omega > \omega^3$. Moreover, $k^2\omega > k^4$ to guarantee that (N>3)-order terms from Eq.(2) are also negligible.

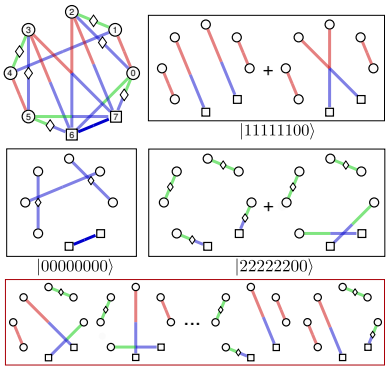

Figure 3: An abstract graph for producing a three-dimensional six-particle GHZ state with two ancillary particles. The diamonds along the edges represent that the edge weights are negative. Vertices 6 and 7 depicted by squares are for ancillas, which are in the same mode number (e.g., blue color for mode number 0). Five perfect matchings in black boxes contribute to the three terms in the desired GHZ state, while the rest of the perfect matchings are destructively canceled out.

Asymptotic Solutions – Until now, we know that each perfect matching can contribute to a term of the quantum state, and their coherent superposition gives the desired state. With the above graph-experimental link, one now expects to produce arbitrary multi-particle entanglement in high dimensions, e.g., a six-particle three-dimension GHZ state. A GHZ state appears when all perfect matchings are disjoint, i.e., every edge is used only in one perfect matching [33, 34]. However, it has been shown that it is impossible to construct a graph of more than four vertices with only three disjoint perfect matchings [33, 34]. Fig. 2 exemplifies this point. Three disjoint perfect matchings contribute to the desired quantum terms. However, there is another perfect matching that leads to an additional term that is not part of the GHZ state (the so-called Maverick term [33]). While we cannot fully erase the term, and therefore achieve a GHZ state with perfect fidelity, we can reduce the weight of the undesired term. Yet, one must be cautious with (N>3)-order terms from Eq.(2), since they also need to be smaller than the GHZ state terms we are targeting. These two constraints boil down to the inequalities $k^2 > \omega^2$ and $\omega > k^2$, respectively, which are both experimentally feasible. We call this and similar graphs *asymptotic solutions*(Fig. 2) .

Ancillary Particles – Although there is a limitation to the state generation with standard linear optics and post-selection in the graph representation [34, 73], one can further employ ancillary particles to completely get rid of Maverick terms [39, 74]. For example, assisted with two ancillary photons, we can obtain the six-particle three-dimension GHZ state (details see Fig. 3). Additionally, to create quantum states with an odd number of particles, one can just use some odd numbers of photons produced from photon-pair sources as ancillary particles [35]. We present further examples in section 4.

2.1.2 Deterministic Single-Photon Sources

In the above section 2.1.1, we have treated an edge in a graph as a probabilistic photon-pair source (in general, as the correlated photon pair) and a vertex for an optical path connecting to a single-photon (non)sensitive detector. Experimentally, one can construct a single-photon source that relies on a probabilistic photon-pair source, where one photon is detected heralds the presence of the other [18]. For example, the single-photon source in path SPS_d (SPS_c) is conditionally on the detection of only one photon in the path d (c) using a probabilistic photon-pair

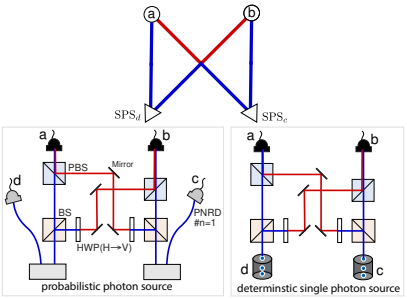

Figure 4: An abstract graph for quantum experiments producing a Bell state with single-photon sources. The vertices SPS$_d$ and SPS$_c$ described as triangles stand for the incoming path for single-photon sources while vertices a and b stand for the optical paths. No edges are allowed between input vertices SPS$_d$ and SPS$_c$. The perfect matchings in this graph lead to a two-dimensional Bell state. The corresponding experiments are listed below. Experimentally, a single-photon source can be either a heralded single-photon source implemented with a photon-pair source and a photon-number-resolving detector (PNRD) or a deterministic single-photon source which can be an ideal quantum-dot-based source. In this experiment, the two photons arrive at the same time (and have the same wavelength, polarization, and spatial mode) such that they are indistinguishable.

source and a photon-number-resolving detector, as shown in Fig. 4. In the graph representation, one can consider that there is an edge between the vertex SPS$_d$ (SPS$_c$) and a virtual vertex which always needs to have exactly one incoming edge. For simplicity, we can just use a input vertex (e.g., SPS$_d$ or SPS$_c$, without drawing its adjacent virtual vertex) for such a single-photon source based on a probabilistic photon-pair source, see Fig. 4. There are no connecting edges between two input vertices. The edge connecting to an input vertex is reinterpreted as photons propagate towards a detector [32, 75].

Interestingly, this can also be explained in Klyshko's advanced-wave picture, described as "an intuitive treatment of two-photon correlation with the help of the concept of an effective field acting upon one of the two detectors and formed by parametric conversion of the advanced wave emitted by the second detector" [76, 77]. In other words, we can treat an edge as a quantum information transfer of one single system; thus, one can describe many abstract quantum information flows instead of just probabilistic photon-pair sources. In general, our input vertex representation is directly applicable to deterministic single-photon sources such as the ideal on-demand sources based on semiconductor quantum dots [13–16] or multiplexed single-photon sources [78]. Therefore, PyTheus can design experiments that use single-photon sources.

2.1.3 Mixed States

So far, we have considered coherent creation processes, resulting in pure states. However, experimentally it is possible to introduce incoherence. Whenever distinguishing information about the quantum state escapes from the experiment to the environment, a partial trace of the density matrix is performed, producing a mixed state. This fact can be used systematically in the graph representation. To do so, we dedicate one of the vertices as the environment (environment vertex). We produce the full quantum state

$$|\psi\rangle = |\psi_0\rangle\,|0\rangle_{\text{env}} + |\psi_1\rangle\,|1\rangle_{\text{env}} + |\psi_2\rangle\,|2\rangle_{\text{env}} + \dots . \tag{4}$$

Then, tracing out the environment contribution, we obtain

$$\rho = |\psi_0\rangle\langle\psi_0| + |\psi_1\rangle\langle\psi_1| + |\psi_2\rangle\langle\psi_2| + \dots . \tag{5}$$

We illustrate this procedure by a simple example in Fig. 5. From a graph that produces

$$|\psi\rangle = |000\rangle_{abc}\,|0\rangle_{\text{env}} + |111\rangle_{abc}\,|1\rangle_{\text{env}}\,, \tag{6}$$

we trace out the last photon obtaining

$$\rho_{000111} = |000\rangle\langle 000| + |111\rangle\langle 111|\,. \tag{7}$$

This procedure is experimentally achieved by using detectors that do not distinguish between the modes in vertex env. For example, if spatial modes are used, one can use a wide-area photon detector or multi-mode fibers in front of the detector. If the time degree of freedom is used to encode the mode numbers, one can integrate over the entire time such that one cannot distinguish between time-bins. Doing so, we introduce mixedness and recover the state in Eq. (7). Similarly to the translation in 2.1.1, we can also translate the graph for creating mixed states into different schemes, as shown in Fig. 5. Therefore, PyTheus can be used to design experiments for complex and interesting mixed states.

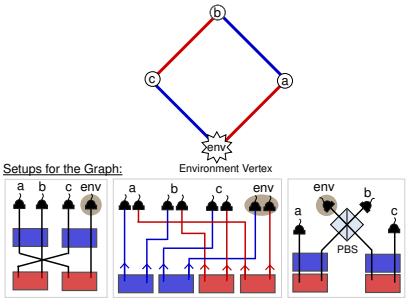

Figure 5: An abstract graph for producing mixed states. The detection paths were labeled a, b, c, and env, and internal modes described in blue and red are mode numbers 0 and 1. A mixed state can be generated by using one of the vertices as the environment (vertex env in this example). Experimentally this could be implemented by measurements that do not discriminate between the photon modes, for instance, detectors with a large active area. The corresponding setups for the graph are listed below.

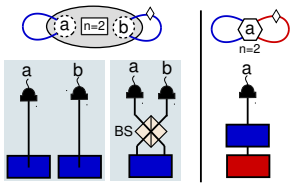

Figure 6: Graphs for producing $|\mathrm{N00N}\rangle_2^2$ states and the related experiments. On the left side, the graph with two blue edges (i.e., two self-loops) is for a path-entangled N00N state $(|2,0\rangle_{a,b} - |0,2\rangle_{a,b})/\sqrt{2}$. We translate this graph into several setups (below the graph). The setups using path identity or path encoding are the same in this case. With bulk optics, one can achieve the state with a Hong-Ou-Mandel interferometry [87, 20], where two identical photons enter a 50:50 beam splitter. One can also perform such a state in polarization, i.e., $(|2,0\rangle_{H,V} - |0,2\rangle_{V,H})/\sqrt{2}$ on the right side. The blue and red colors are, respectively, for horizontal and vertical polarization. The coherent superposition of blue and red self-loops gives the N00N state. Its related setup is described below the graph. There either two horizontally polarized photons (blue edge) or two vertically polarized photons (red edge) are in path a with a single-photon sensitive detector.

2.1.4 States Entangled in the Photon-Number Basis

Fock states containing a fixed number of particles in a given spatial mode form a complete basis for many-body Hilbert spaces. The superposition of Fock states brings, among others, the well-known N00N states [79, 80] that promise many advantages such as the best-possible quantum-enhanced precision, super-sensitivity and super-resolution [81, 8]. The N-particle N00N state is (up to normalization)

$$|\mathrm{N00N}\rangle_2^N := |N,0\rangle_{a,b} + |0,N\rangle_{a,b}\,, \tag{8}$$

where the subscript number 2 means there are two paths (e.g., a and b), $|0\rangle$ indicates an unoccupied mode. The concept of the N00N state in Eq. (8) can be extended to a multi-mode case, where N particles are distributed in one of several optical paths [82, 83].

We know the total number of photons N going through a set of optical paths, but in contrast to the previous sections, we ignore how many photons occupy each of the paths. Therefore, perfect matchings are not the only contributions to the final state that we must consider. Here, we need to compute all combinations of edges that lead to a total number of N photons for a given set of all optical paths. This includes combinations with repeated edges, which represent multiple photon pairs from the same source, and self-loops, in which a source produces a collinear photon pair [84, 85]. Moreover, for some contributions there can be vertices with degree zero, as long as the total number of photons – the total degree – is N. The conditioning on the total number of photons must be considered when employing the N00N states in metrology experiments, as described in previous work [8, 86].

As an example, we show a graph for the $|\mathrm{N00N}\rangle_2^2$ state in Fig. 6. In this case, the total photon number is $N = 2$. All edges are in the same color, thus corresponding to the standard path-entangled N00N states. A self-loop edge indicates that there are two photons in its connected vertex. Thus the coherent superposition of two photons being in one of the two vertices (one of the self-loops produced a photon-pair, but we ignore it) leads to a coherent superposition of $|2,0\rangle_{a,b}$ and $|0,2\rangle_{a,b}$, i.e., a two-mode two-photon N00N state. One can now translate the graph into quantum experiments, similarly, as we did in section 2.1.1. In this example, the setups using entanglement by path identity and path en-

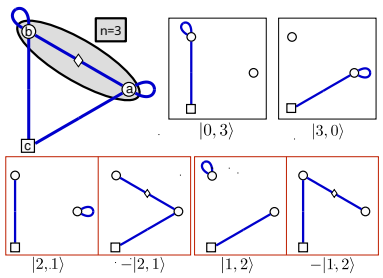

Figure 7: Graph for producing $|\mathrm{N00N}\rangle_2^3$ state with an additional ancillary particle. The total photon number (including ancillary one) for each component in the state is four. There are six combinations of two edges that cover the ancillary vertex only once. Two of them (black box) contribute to the required terms $|3,0\rangle$ and $|0,3\rangle$, and the others ($|2,1\rangle$ and $|1,2\rangle$) inside the red box cancel out.

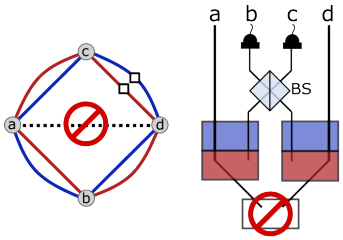

Figure 8: An abstract graph for entanglement swapping. On the right, an experimental setup for entanglement swapping is shown. The two particles a and d are entangled when two ancillary detectors click. A common source of particles a and d (as shown crossed out below the setup) would circumvent the point of entanglement swapping. The two particles are to be entangled without having interacted with each other. This restriction manifests in the graph corresponding to the experiment (shown on the left). An edge between the vertices a and d (dashed line) is not permitted.

coding are the same. With bulk optics, one can use probabilistic beam splitters that provide the mixing between the two input photons, to bunch two photons in one of the two optical paths a and b, which is the well-known Hong-Ou-Mandel (HOM) effect [20, 87]. Moreover, we can also generate such a N00N state in polarization or transverse spatial modes instead of the path; see Fig. 6 for details.

As for the previous states, ancillary paths can assist in the creation of states on the photon-number basis. Here we condition the final state on the existence of a total number of photons in the non-ancilla detectors but, again, the ancilla paths are reached by single photons. Fig. 7 shows an example in which the ancilla (vertex 3) receives only one photon, and the other two detectors get a total of three photons.

2.2 Quantum Communication

In future quantum networks that connect individual users with quantum resources and quantum computers, the distribution of quantum entanglement is essential. One key concept used in quantum communication in quantum networks is entanglement swapping [88, 89], where two qubits that never interacted can be entangled. This provides an important route for interesting tests of quantum foundations and plays an indispensable role in quantum technology such as quantum repeaters [90]. PyTheus allows us to explore new directions that could lead to solutions that require fewer resources than current techniques or are implemented in surprising ways. Many quantum network communication tasks have been experimentally implemented [89, 91–93], thus the new solutions by PyTheus can readily be implemented in laboratories.

We are interested in finding experimental setups for creating entanglement between particles that have not interacted or originated from a common source. With PyTheus this can be done for scenarios involving higher dimensions and multiple particles. Finding the corresponding graph works analogously to the state generation task shown in section 2.1, but comes with extra constraints on the graph. We set an entangled state (e.g. two particles in a Bell state) as a target for the optimization. The experiment corresponding to the resulting graph should create this state. To ensure that the two particles have no direct interaction, the graph must fulfill the following additional constraint. It should have no edge connecting the two corresponding vertices. Such an edge translated to a photon pair source would mean that the two photons could come out of the same source. This is shown in Fig. 8. Similarly, the connection of two vertices to the same single-photon source vertex implies that they can not be space-like separated. Such constellations

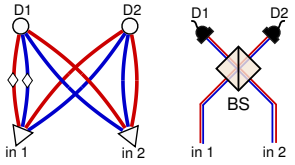

Figure 9: An abstract graph for Bell state measurement. A measurement event happens if the photons **in1** and **in2** are in the Bell state $|\Psi^-\rangle$. Simultaneous clicks in the detectors $D1$ and $D2$ signify a successful Bell measurement. The corresponding setup is given for the graph, which is a typical Bell state measurement setup.

would not be valid for entanglement swapping, either. In the same way, as for incoming photons (single photon sources or input photons), the constraints are enforced by removing the edges from the starting graph.

Approaching these tasks with PyTheus makes it possible to explore new ways of distributing entanglement. We show the examples found by PyTheus in section 4.

2.3 Quantum Measurements

A graph may also be interpreted as a quantum measurement on an input quantum state. Such measurements are of utmost importance in many quantum communication tasks, for example, a Bell state measurement for quantum teleportation. The goal of measurements here is to distinguish different orthogonal incoming states, e.g., in the case when all detectors click simultaneously. Photons entering the experiment through input paths are represented analogously to single-photon sources introduced in section 2.1.2. An input photon corresponds to one vertex in the graph. An edge connecting an input vertex to a detector vertex corresponds to the photon traveling to that detector, following Klyshko's advanced-wave picture [76] as explained in section 2.1.2. The same constraints apply, excluding edges connecting two vertices belonging to input photons.

As an example, we show a graph in Fig. 9 for the well-known Bell state measurement (BSM) [94, 95], which plays an important role in many quantum information tasks. When the two detectors click, the incoming photons are projected to one Bell state $|\Psi^-\rangle$, which can be seen as the generation of a state given by a superposition of the two perfect matchings in the graph. To search for an experimental setup for measuring a particular state, we let PyTheus search for a graph that would produce the state under consideration of the topological constraints on the graph. The graph in Fig. 9 interpreted as state generation would produce the state $|\Psi^-\rangle$ under the condition that there is no connection between vertices in1 and in2.

With a graph that 'produces' the state $|\varphi\rangle_{in}$, we can effectively perform a projective measurement ($P_0 = |\varphi\rangle\langle\varphi|$ and $P_1 = \mathbb{I} - |\varphi\rangle\langle\varphi|$) on the input photons. A coincidence of all detectors corresponds to the output 0 and any other pattern is interpreted as output 1.

The representation of measurements in terms of graphs constitutes an extension of the previous interpretation given in [32]. This allows us to use PyTheus for the discovery of measurement setups for any state and various constraints and conditions.

2.4 Quantum Computation

Quantum gates are a crucial building block in quantum computation [96, 97]. A quantum gate performs a unitary transformation on an input state. These transformations can also be interpreted in terms of graphs. In these graphs, similar to measurements (described in subsection 2.3), the input photons are described by designated vertices. Likewise, we impose restrictions on which types of vertices can be connected by edges. Photons exiting the setup (output) are also represented by vertices, as in state generation. Additional ancillary photons can stem from probabilistic photon-pair sources and single-photon sources can also be involved. With PyTheus we can search for arbitrary quantum gates under a wide range of experimental conditions.

A target unitary quantum gate acting on an N-dimensional Hilbert space is specified by how each element of an orthonormal basis transforms. One canonical example in quantum gates is the controlled-NOT (CNOT) gate, which acts on two

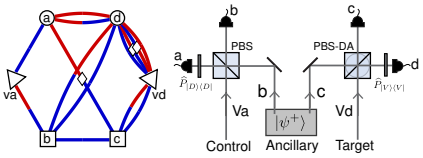

Figure 10: An abstract graph for a quantum CNOT gate shown on the left side. The right panels show the corresponding setup for a CNOT gate, which was realized by [98].

qubits and is described by the mapping:

$$|00\rangle \to |00\rangle\,,$$
$$|01\rangle \to |01\rangle\,,$$
$$|10\rangle \to |11\rangle\,,$$
$$|11\rangle \to |10\rangle\,.$$

To find this gate, we let PyTheus search for a graph that would produce the state

$$|00\rangle\,|00\rangle + |01\rangle\,|01\rangle + |10\rangle\,|11\rangle + |11\rangle\,|10\rangle\,; \quad (9)$$

under consideration of the topological constraints on the graph (no connections between input photons). In Fig. 10, we show an experimental setup realized [98] together with its graph representation.

Photonic quantum gates fall into two main categories [99]. In a post-selected gate, the outgoing photons are detected directly after the gate. This ensures that there is exactly one photon in each path after the gate [100–107]. Because possibilities where two outgoing photons enter the same path are excluded, fewer experimental resources are required. However, this procedure destroys the outgoing state, and the particles can not be used further. The second category is heralded gates [98, 108–113], where only ancillary photons are detected, and the outgoing photons of the gate remain undetected. These gates are ultimately more useful since the output state can be used further. A graph for a heralded quantum gate is harder to discover and needs more experimental resources since the looser selection rules can lead to more unwanted terms. Both types of quantum gates (post-selected and heralded) can be represented with graphs and thereby be designed using PyTheus. Terms produced in post-selected experiments are represented by perfect matching, and terms produced in heralded experiments are represented by collections of edges that cover the ancillary vertices.

The ability to perform design for quantum measurements and quantum gates relies on an idea that state generation and state propagation are closely related [32]. In the experimental quantum optics community, this idea is known as Klyshko's advanced-wave picture [76, 114], while in the quantum information science community it is often referred as Choi–Jamiołkowski isomorphism [115].

3 The PyTheus Library

Starting from a dense or fully connected graph, PyTheus uses gradient descent combined with topological optimization to find minimal graphs corresponding to some target quantum experiment. The PyTheus library greatly expands the range of applications of its predecessor, and it is significantly faster [3]. The package is written in Python and is available on GitHub for further applications and development of the source code. The graph encoding is compatible with other tools such as *The Walrus*[56], a library to (among other applications) compute perfect matchings from the graphs' adjacency matrix. [4].

PyTheus applications range from the creation of quantum states to the design of quantum communication protocols. While diverse, all these tasks are performed following the same steps, illustrated in Fig. 11. In this section, we explain the software workflow, which kind of loss functions we employ, and how to start using PyTheus.

Workflow Overview – The *Instruction Set* file details *what* we want (e.g., a quantum state or a communication protocol) and some instructions about *how* to get it. The latter includes the entire allowed topology of the final solution, such as the type of photon sources/detectors and ancillary particles, how many of each we have, or which polarization modes can be used. It also contains the

[3]For an eight-dimensional three-particle highly-entangled state (SRV(8, 5, 3)) PyTheus was almost five times faster than the current state-of-the-art method [32]. Examples of higher particle numbers were not readily available for the previous method, but we expect increasingly higher advantages for PyTheus.

[4]The loops' weights in the adjacency matrix must be multiplied by 2.

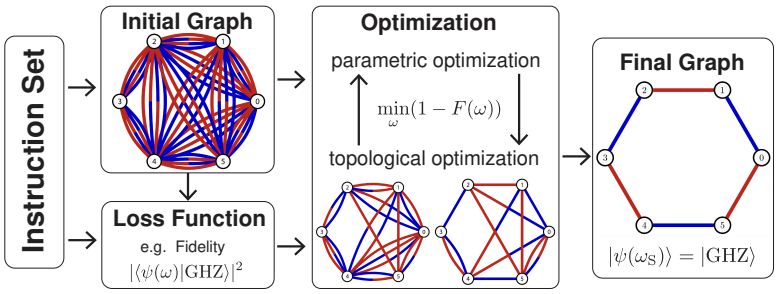

Figure 11: The PyTheus workflow. From the number of vertices and available dimensions, PyTheus builds the initial graph, which is fully connected except for vertex 3, which is only connected to its nearest neighbors. We impose this based on previous knowledge, but other constraints may arise depending on the available tools. Computing all the graph's perfect matchings, we find the more general state that the initial graph can produce: $|\psi(\omega)\rangle$. As the loss function, we choose the *Fidelity* of the state $|\psi\rangle$ with respect the target: $|\mathrm{GHZ}\rangle$. Aiming for an interpretable graph with perfect fidelity, we iterate the weight optimization with the edge removal until we find the simplest graph that produces $|\mathrm{GHZ}\rangle = |\psi(\omega_S)\rangle$. The available resources, the loss function and further optimization details are specified in the *Instruction Set*.

Loss Function to minimize (fidelity, count rate, or other metrics) as well as further optimization settings. In the example of Fig. 11, we want to obtain a post-selected six-particle, two-dimensional GHZ state, $|\mathrm{GHZ}\rangle_6^2 = |000000\rangle + |111111\rangle$. We employ 6 standard photodetectors and the photon pair sources described in section 2.1.1. In this example, we also specify further topological constraints of the final solution (thus of the initial graph) – here, vertex 3 must not have connections to vertex 0, 1 and 5.

The experimentally available topology specified in the instruction set lead to the *Initial Graph*. This weighted graph represents all possible states/experiments that can be produced with the available resources. The number of vertices, the type of edges, or which vertices can be directly connected are some of the *Topological Constraints* that one can impose on the graph or that may follow from the available tools or from the task we want to implement – the sources described in section 2.1.2 and the protocols from section 2.2 are representing examples. On the initial graph of Fig. 11 the six vertices are connected with bicolored edges and based on previous knowledge, we only connect vertex 3 with its nearest neighbors.

From the initial graph, $\mathcal{G}(\omega)$, we can compute the more general state produced by the weight function $\Phi(\omega)$ acting on the vacuum (see Eq. (2)). However, we do not consider the infinite terms produced by $\Phi(\omega)$, we only compute the creation events which fulfill certain *Conditional rules*. For example, in Fig. 11 the post-selection rule results in terms for which all detectors click. These creation events are represented by the graph's perfect matchings, and produce a coherent superposition of kets leading to the state $|\psi(\omega)\rangle$. We can specify more complex conditioning rules, which will be relevant, for example, for N00N states. There, we condition on states with a total final photon number in the output nodes. The conditioning rules are imposed by experimental circumstances 2.

Once we extract a general state $|\psi(\omega)\rangle$ from the initial graph, we can optimize it according to some *Loss Function*. As in Fig. 11 we seek a particular state, $|\mathrm{GHZ}\rangle$, we maximize the *Fidelity* of our state accordingly: $F = |\langle \mathrm{GHZ}|\psi(\omega)\rangle|^2$. To find a specific states we can also use the *Count Rate*, a metric that approximates how often our experiment produces such a state. Alternatively, we can maximize physical properties like entanglement rather than looking for a specific state. To perform quantum information tasks like measurements or communication protocols, we must translate each task into a state creation process – see sections 2.3, 2.2, and 2.4 for further details.

If the available experimental resources suffice, by optimizing the weights, we will find a graph that satisfies our needs. However, the opti-

mal solution is not unique, and even if many of the weights vanish, we will likely obtain a very dense final graph, which will be hard to interpret. Therefore, to extract useful insights from our setups, we must simplify the graphs as much as possible, alternating the optimization of the weights' values with the removal of edges. This *Topological Optimization* will lead us to a simple graph, for which the removal of any additional edge would unacceptably raise the loss function's value.

For some graphs, like the one shown in Fig. 11, no smaller graph can produce the target state [33]. However, in most cases, it is challenging to ascertain whether there exists a simpler solution, especially when we choose to optimize for real weights instead of complex ones. With respect to these subtleties, following the workflow, we first generate graphs with abundant ancillary particles and reassess the results with the goal of reducing the number of resources. Using this procedure, we propose one hundred experiments to be realized in quantum optics.

4 Hundred Experiments

In the following, we introduce one hundred experiments conceived by PyTheus. A broad catalog of designs that, hopefully, will contribute to multiple branches of quantum optics, including quantum computing, communications, and quantum sensing. For each proposed experimental setup which is new and has not been described in any theoretical or experimental paper, we mark the corresponding graph with a number in a box counting from 1 to 100. The weights of each graph can be found in the GitHub repository, together with the instruction sets used to search them.

We start by showing seven highlights from our discoveries in Table. 2.

(a) A multi-photon entangled state that goes beyond the barrier of 3-dimensions [34]. It requires only two ancillas and has a small number of edges which makes it a very promising proposal for practical application, and observation of new properties at the foundation of quantum mechanics [116].

(b) The generation of a two-mode N00N state with 5 photons. The associated graph, very symmetric, makes use of 3 ancillas.

(c) A post-selected 3-photon control gate (or Toffoli) that does not require any ancilla photons.

(d) A 4-photon qubit quantum state with equal coefficients $c = \frac{1}{\sqrt{\tau}}$, that requires the ratio between certain weights to be the golden ratio. Alternatively, a lower number of complex-weighted edges can also lead to such state.

(e) A previously unknown quantum measurement scheme that allows the experimental implementation of a quantum communication protocol, the Mean King problem, proposed in 1987 [117].

(f) A very surprising form of quantum entanglement swapping, which does not rely on the generation of two Bell pairs and a Bell state measurement.

(g) Experimental setup of a 2-photon mixed entangled state that falsified the Peres conjecture [118]. The state is bound entangled (its entanglement cannot be distilled), however, it can be used to violate Bell's inequality [119, 120]. This could lead to an experimental falsification of the Peres conjecture.

4.1 Generation of Entangled States

In this part, we propose ways to generate entangled states, which play an important role not only in our understanding of entanglement and the non-local nature of quantum mechanics but also in many quantum information applications.

4.1.1 GHZ States

Bell's theorem shows that Einstein-Podolsky-Rosen's propositions about local realism [121] are inconsistent when we apply them to quantum systems of two particles, revealed by the violation of the Bell inequality with quantum mechanical statistical correlations [122]. In the late 1980s, Greenberger, Horne, and Zeilinger took a step further from two to three particles. Interestingly, with a tripartite quantum system, local realism can be violated by quantum mechanics with perfect correlations rather than statistical correlation, and one can completely dispense with inequalities [123, 124]. It enables the performance

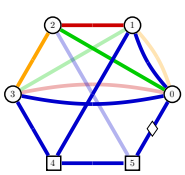

(a) 4-dimensional 4-photon GHZ state (asymptotic and exact solutions).

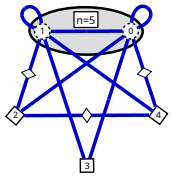

(b) 2-mode 5-photon N00N state $|50\rangle + |05\rangle$ (symmetric graph with an inscribed pentagram).

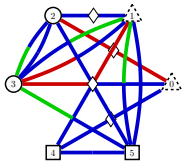

(c) Post-selected CNOT quantum gate acting on a qutrit target with two ancilla photons

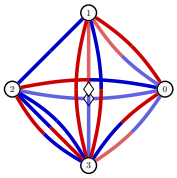

(d) A 4-qubit entangled state which requires weights with the golden ratio (or complex-valued) to be generated.

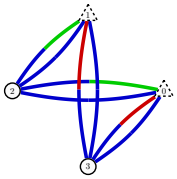

(e) Quantum measurement for a quantum communication task with quantum advantage (Mean King's Problem).

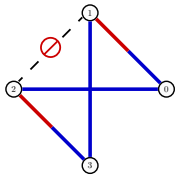

(f) Entangling photons that never interacted (related to entanglement swapping) without initial Bell states.

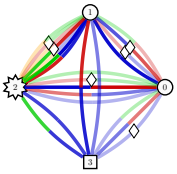

(g) Mixed state with bound entanglement that violates Bell inequality (counterexample to the Peres conjecture from 1999, solved 2014).

Table 2: A collection of seven diverse highlights, each of which is interesting in its own right.

of experiments where the *quantum physical predictions are mutually contradictory with expectations based on local realism* [125]. Such a GHZ state forms an important class of entanglement and its generalization is given as

$$|\mathrm{GHZ}\rangle_n^d = \frac{1}{\sqrt{d}} \sum_{i=0}^{d-1} |i\rangle^{\otimes n}, \tag{10}$$

where n denotes the number of particles and d is the dimension for each particle.

Increasing the number of particles and dimensions in the GHZ states not only enlarges the Hilbert space but also leads to many new exciting classically paradoxical phenomena [126, 116, 127]. Besides their fundamental interest, high-dimensional multiparticle GHZ states have also served as an important resource for many quantum information applications [128].

With the size and dimension increasing, it is very challenging to know how to experimentally create GHZ states. Experimental progress has been made in this direction to push the size and dimension, especially in the linear optics regime [70, 71, 129, 28]. Until now, only the three-particle three-dimensional GHZ state has been demonstrated with linear optics [28] and superconducting qutrits [130]. Going beyond the $|\mathrm{GHZ}\rangle_3^3$ state with arbitrary particle numbers and higher dimensions will give rise to exciting new possible quantum applications and new insights on the foundations of quantum mechanics. This remains to be explored, in any experimental platform.

PyTheus enables the discovery of many new multi-particle high-dimensional GHZ states for which no experimental implementations are known yet. That includes the 3-particle GHZ state for 4, 5 and 6 dimensions 1 2 3, the 2 solutions (asymptotic and exact) for the 4-particle 4-dimension GHZ state 4 5, and the 5-particle GHZ state for 3 and 4 dimensions 6 7, as shown in Fig. 12.

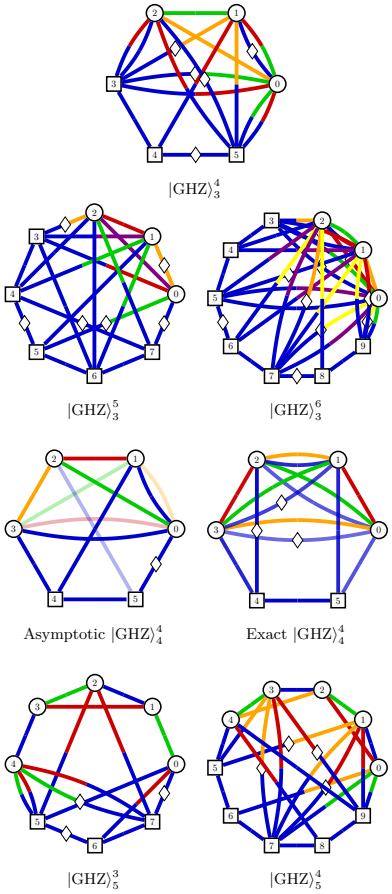

Figure 12: High-dimensional multiparticle GHZ states with ancillas. The weights here in these graphs are real numbers and the diamonds inserted in the edges represent the negative sign. The vertices in square refer to the detection of an ancillary photon. For the state $|\mathrm{GHZ}\rangle_4^4$ we have two possible solutions.

4.1.2 Bell Gems

Bell states offered the first proof of the nonlocality of quantum mechanics. Later on, they became the cornerstone of many quantum communication schemes and are nowadays widely used in quantum computing. These maximally entangled bipartite states, described in the Hilbert space $\mathcal{H}_2 \otimes \mathcal{H}_2$, can be generalized for more particles and dimensions in multiple ways while keeping their main properties [131].

In 2004, Gregg Jaeger suggested a generalization for sets of 2^N qubits, the *Bell Gems* [132]. To construct these states we need to pick a pair of orthogonal states $|\alpha\rangle$ and $|\beta\rangle$ from the Bell basis: $|\Phi^{\pm}\rangle = |00\rangle \pm |11\rangle$ and $|\Psi^{\pm}\rangle = |01\rangle \pm |10\rangle$. Then, we iterate the following mappings in all possible ways:

$$\{|\alpha\rangle, |\beta\rangle\} \to (|\alpha\rangle\,|\alpha\rangle \pm |\beta\rangle\,|\beta\rangle) \tag{11}$$
$$\{|\alpha\rangle, |\beta\rangle\} \to (|\alpha\rangle\,|\beta\rangle \pm |\beta\rangle\,|\alpha\rangle) \tag{12}$$

Therefore, for 2^N qubits, we get a basis of 2^{2^N} states. For the case of a pair of 3 dimensional Bell states 84 states exist. Fig. 13 shows how to generate one of these high-dimensional Bell gems which, up to normalization, reads 8

$$|\mathrm{GEM}\rangle = |\psi_a\rangle\,|\psi_a\rangle + |\psi_b\rangle\,|\psi_b\rangle + |\psi_c\rangle\,|\psi_c\rangle\,, \tag{13}$$

where $|\psi_a\rangle = |00\rangle + |11\rangle + |22\rangle$, $|\psi_b\rangle = |01\rangle + |12\rangle + |20\rangle$, and $|\psi_c\rangle = |02\rangle + |10\rangle + |21\rangle$.

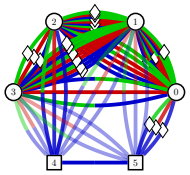

Figure 13: Graph corresponding to the creation of a 3 qutrit Bell gem.

4.1.3 Nine Ways to Entangle Four Qubits

In 2001, F. Verstraete et. al. [133] introduced a classification of any form of entanglement between 4 qubits into nine categories. Their classification establishes an equivalence relation between states generated by reversible stochastic local quantum operations assisted by classical communication (SLOCC) operations. States inside the same category can perform the same quantum information tasks, albeit with different probabilities.

Out of the nine categories, six of them include well-known quantum states: a separable state of

4 qubits, the W states of 3 and 4 qubits, the product of 2 Bell states, and the GHZ states of 3 and 4 qubits. For the 3 qubit states, the fourth particle is separable (like an ancilla). Fig. 14 shows the graphs to produce these states.

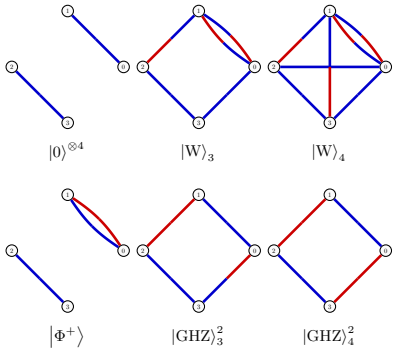

Figure 14: Six well-known examples from different entanglement categories described by Verstraete et. al. [133]

The remaining three categories, out of the initial nine ones, refer to less-known ways of entanglement. Verstraete's work refers to them as L_{a_4}, $L_{0_{5\oplus\overline{3}}}$, and $L_{0_{7\oplus\overline{1}}}$. In Fig. 15 we see a graph for each category, producing the states [9] [10] [11]

$$|\mathrm{L}_{a_4}\rangle = |0001\rangle + |0110\rangle + |1000\rangle\,, \tag{14}$$

$$\left|\mathrm{L}_{0_{5\oplus\overline{3}}}\right\rangle = |0000\rangle + |0101\rangle + |1000\rangle + |1110\rangle\,, \tag{15}$$

$$\left|\mathrm{L}_{7\oplus\overline{1}}\right\rangle = |0000\rangle + |1011\rangle + |1101\rangle + |1110\rangle\,. \tag{16}$$

4.1.4 Quantum Error Correction

The path to the quantum computer requires qubits with low error rates independent of their realization platform. However, dealing with noise on any platform is inevitable. Thus, we need error-correcting codes to protect the information and achieve fault-tolerant quantum computation. This is where *Logical Qubits* play a crucial role.

Logical qubits are sets of N physical qubits that define two orthogonal states $|0_L\rangle$ and $|1_L\rangle$. These states are defined in such a way that errors

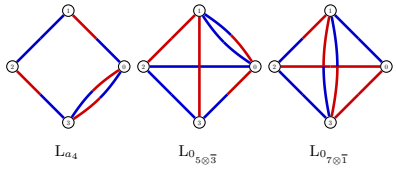

Figure 15: Graphs for L_{a_4}, $L_{0_{5\oplus\overline{3}}}$, and $L_{0_{7\oplus\overline{1}}}$.

in the physical qubits can be detected by applying a set of global measurements. These measurements will produce a different combination of outcomes for each potential error, allowing its correction. The graphs from this section produce 3 well-known logical qubits to detect and correct arbitrary errors on single qubits.

The first one, the Shor code [134], employs 9 physical qubits to define [12]

$$\left|0_L^{(9)}\right\rangle = (|000\rangle + |111\rangle)^{\otimes 3}, \tag{17}$$

$$\left|1_L^{(9)}\right\rangle = (|000\rangle - |111\rangle)^{\otimes 3}. \tag{18}$$

The second example, the Steane code [135], employs 7 physical qubits [13]

$$\begin{aligned}\left|0_L^{(7)}\right\rangle = {} & |0000000\rangle + |1010101\rangle + |0110011\rangle \\ & + |1100110\rangle + |0001111\rangle + |1011010\rangle \\ & + |0111100\rangle + |1101001\rangle\,,\end{aligned} \tag{19}$$

$$\left|1_L^{(7)}\right\rangle = X^{\otimes 7}\left|0_L^{(7)}\right\rangle = X_L\left|0_L^{(7)}\right\rangle. \tag{20}$$

We go from the logical qubit to the other by applying a logical gate X_L, that is, by applying a Pauli X gate on each physical qubit.

The third and last one, with only five physical qubits [136], is the Laflamme code [14]

$$\begin{aligned}\left|0_L^{(5)}\right\rangle = {} & |00000\rangle + |11000\rangle + |01100\rangle + |00110\rangle \\ & + |00011\rangle + |10001\rangle - |10100\rangle - |01010\rangle \\ & - |00101\rangle - |10010\rangle - |01001\rangle - |11110\rangle \\ & - |01111\rangle - |10111\rangle - |11011\rangle - |11101\rangle\,,\end{aligned} \tag{21}$$

$$\left|1_L^{(5)}\right\rangle = X^{\otimes 5}\left|0_L^{(5)}\right\rangle = X_L\left|0_L^{(5)}\right\rangle. \tag{22}$$

These two logical qubits constitute the smallest error-correcting code resilient to arbitrary single qubit errors [137].

Fig. 16 shows the graphs for producing each of the logical 0 states for 5, 7, and 9 physical qubits.

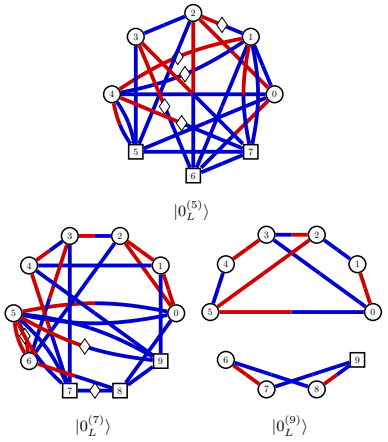

Figure 16: Graphs for generating the logical 0 state using 5, 7, and 9 physical qubits (+ ancillas, which are in a fixed state).

For the Shor code, the second logical qubit state can be obtained by multiplying the weights of every bicolored edge by -1 (or alternatively, taking the 3rd, 6th, and 9th qubits and applying a minus at each red incoming edge). For the other two codes, one can obtain the graphs associated with the logical 1 state by switching the colors blue and red. Such transformation is equivalent to applying the gate X on each qubit, the logical X_L.

4.1.5 Products of W States

Previous work with the graph representation showed how to create W states for an arbitrary even number of qubits without using any ancilla [35]. On the other hand, to generate a W state with an odd number of qubits, we always needed at least one ancillary detector. Accordingly, if we want to duplicate such odd-qubit states, we can simply duplicate the graph together with the ancillas. However, this straightforward method is not the most efficient, at least for the states $|W_3\rangle^{\otimes 2}$ and $|W_5\rangle^{\otimes 2}$. As shown in Fig. 17, these two states can be obtained without using ancillas [15] [16].

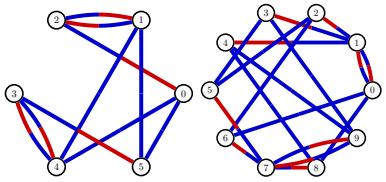

Figure 17: Graphs for generating the states $|W_3\rangle^{\otimes 2}$ and $|W_5\rangle^{\otimes 2}$ without ancillas.

4.1.6 Dicke States

The equal superposition of every N-qubit state containing a single $|1\rangle$ gives us the W states. These states can be generalized, superposing all permutations of N qubits with exactly k $|1\rangle$s. They are the *Dicke states*

$$\left|D_N^k\right\rangle = \sqrt{\frac{k!(N-k)!}{N!}} \sum_i P_i(|0\rangle^{\otimes N-k}\,|1\rangle^{\otimes k}), \tag{23}$$

where $\sum_i P_i(\cdot)$ stands for all possible permutations of k $|1\rangle$ among N qubits. These states, which have applications in multiparty quantum communication and quantum metrology [138–141], can be produced for an even number of qubits with a general graph introduced in previous works [35]. Here we produce a pair of Dicke states with an odd number of qubits and two excitations [17] [18] (see Fig. 18).

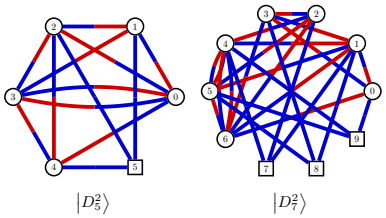

Figure 18: Dicke states with two $|1\rangle$ for five and seven qubits.

Moreover, there exists a generalization of Dicke states for higher dimensions [142]. Given a set of integers $\{k_i\}$, such that $\sum_i k_i = N$, we describe

its corresponding d-dimensional Dicke state as

$$|D(N,\{k_i\})\rangle = \sqrt{\frac{\prod_i k_i!}{N!}} \sum_i P_i(|0\rangle^{\otimes k_0} |1\rangle^{\otimes k_1} \dots |d-1\rangle^{\otimes k_{d-1}}) \tag{24}$$

where $\sum_i P_i(\cdot)$ stands for all possible permutations of the N qudits. In Fig. 19 we plot the graphs that produce the 3-dimensional Dicke state with three particles 19

$$|D(3,(1,1,1)\rangle = |012\rangle + |021\rangle + |102\rangle + |120\rangle + |201\rangle + |210\rangle\,, \tag{25}$$

and with 4 particles (with uneven coefficients $\{k_i\}$) 20

$$\begin{aligned}|D(4,(2,1,1))\rangle = &|0012\rangle + |1200\rangle + |1020\rangle \\ &+ |0102\rangle + |1002\rangle + |0120\rangle \\ &+ |0021\rangle + |2100\rangle + |2010\rangle \\ &+ |0201\rangle + |2001\rangle + |0210\rangle\,.\end{aligned} \tag{26}$$

After plotting the results found by PyTheus to generate the last two states, we found a pattern on the graphs that led us to states like $|D(5,(2,2,1)\rangle$ and $|D(4,(1,1,1,1))\rangle$: We start taking a fully connected graph of N particles, in which the vertices are connected by 2 bicolored edges, blue-red and red-blue, indicating two modes (the same as in Ref. [35]). Then one can add ancillas that are connected to the N first particles by bicolored edges, one for each of the N particles. These new edges introduce more modes, leading to the following series of states for an even number of particles, $2k$:

$$\begin{aligned}&0 \text{ ancillas, } 2 \text{ modes} \to |D(2k,(k,k))\rangle \\ &\quad 2 \text{ anc, } 3 \text{ modes} \to |D(2k,(k,k\text{ - }1,1))\rangle \\ &\quad 2 \text{ anc, } 4 \text{ modes} \to |D(2k,(k\text{ - }1,k\text{ - }1,1,1))\rangle \\ &\qquad\qquad \dots \\ &2(k\text{ - }1) \text{ anc, } 2k \text{ modes} \to |D(2k,(1,\cdots,1))\rangle\end{aligned}$$

For an odd number of particles, $2k+1$, starting with 1 ancilla, we obtain

$$\begin{aligned}&1 \text{ anc, } 3 \text{ modes} \to |D(2k{+}1,(k,k,1))\rangle \\ &3 \text{ anc, } 4 \text{ modes} \to |D(2k{+}1,(k,k\text{ - }1,1,1))\rangle \\ &3 \text{ anc, } 5 \text{ modes} \to |D(2k{+}1,(k\text{ - }1,k\text{ - }1,1,1))\rangle \\ &\qquad\qquad \dots \\ &2k\text{ - }1 \text{ anc, } 2k{+}1 \text{ modes} \to |D(2k{+}1,(1,\cdots,1))\rangle\,.\end{aligned}$$

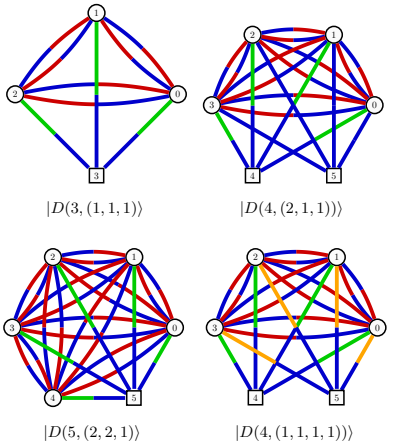

Figure 19: The three-dimensional Dicke states for three and four particles (top) were found by PyTheus. The 2 graphs in the bottom row were manually produced following the observed pattern.

4.1.7 Yeo-Chua State

In 1993, Bennett et. al. showed how to use Bell states to teleport arbitrary and unknown single-qubit states [143]. Going one step further, Yeo and Chua developed a protocol to teleport unknown states of two qubits [144], and instead of using Bell states, they employed the Yeo-Chua state

$$\begin{aligned}21\ |YC\rangle = &|0000\rangle - |0011\rangle - |0101\rangle \\ &+ |0110\rangle + |1001\rangle + |1001\rangle \\ &+ |1100\rangle + |1111\rangle\,.\end{aligned} \tag{27}$$

This highly entangled state can be produced with the graph of Fig. 20.

4.1.8 Complex Weights as a Resource

Exploring the applicability range of PyTheus, we searched for four-qubit states of the form

$$|\psi\rangle = c_1\,|0000\rangle + c_2\,|0001\rangle + ... + c_{16}\,|1111\rangle\,, \tag{28}$$

where $c_i \in \{0,1\}$. A total of $2^{16} - 1 = 65535$ states. Graphs with ± 1 weights suffice to produce most of the states, many of them do not even

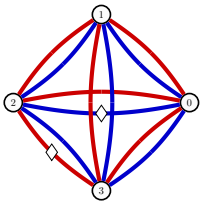

Figure 20: Graph for generating the Yeo-Chua state.

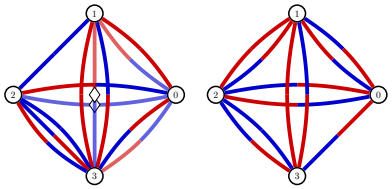

Real solution Complex solution

Figure 21: Graphs for the four-qubit state defined in Eq. (29). The left solution employs the golden ratio and the right one complex weights.

require interference. Yet, some states, such as

$$|\psi\rangle = |0011\rangle + |0100\rangle + |0111\rangle + |1000\rangle + |1100\rangle + |1101\rangle + |1110\rangle\,, \tag{29}$$

require not only destructive interference between creation terms, but very specific ratios between the weights. In particular, the weights to produce the state (29) make use of the *Golden Ratio*, since they must fulfill the expression

$$x^2 + x = 1. \tag{30}$$

The graph that employs the golden ratio is shown in Fig 21, and similar graphs can produce a whole family of 64 states which are equivalent under permutations and bit-flips. However, there is an alternative complex-weighted graph, with less edges, to produce these states. As shown in Fig 21, the absolute value is the same for all weights and the interference patterns due to the complex phases are shown in Fig 22. Even thought they are computationally more expensive to obtain, complex-weighted solutions can provide new interesting designs.

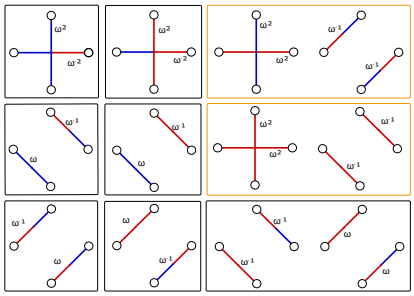

Figure 22: Perfect matchings of graph shown in Fig. 21 for the state defined in Eq. (29). $\omega = e^{i\pi/6}$. Each green box contributes one term of the state. The perfect matchings in the orange boxes interfere destructively. It is especially notable that the weights of the two $|0111\rangle$ perfect matchings (bottom right) are complex conjugates and add to one as $\omega^2 + \omega^{-2} = 1$.

4.1.9 Single Photon Sources for State Creation

Significant progress has been made toward using deterministic single-photon sources in quantum optics experiments during the last years [13, 78, 18]. In this section, we present graphs corresponding to quantum experiments for the creation of several highly entangled states using single-photon sources. Deterministic sources do not suffer from the same trade-off between high fidelity and high count rate as probabilistic sources. When using deterministic sources, the number of photons required can be smaller than with probabilistic sources [145, 146].

Post-Selected We have found graphs for creating different GHZ states with single-photon sources as a resource. One can create a six qubit GHZ from six input photons 22, a four qutrit GHZ state from six input photons 23, as well as the same four qutrit GHZ state from a combination of two single photon sources and two simultaneous SPDC events 24 (see Fig. 23).

Heralded – There have been proposals for the creation of multi-particle high-dimensional entangled states from single photon sources using discrete Fourier transform [74]. In Fig. 24 we show a graph 25, which achieves a heralded Bell state using two ancillary photons without the need for photon-number-resolving detectors with almost

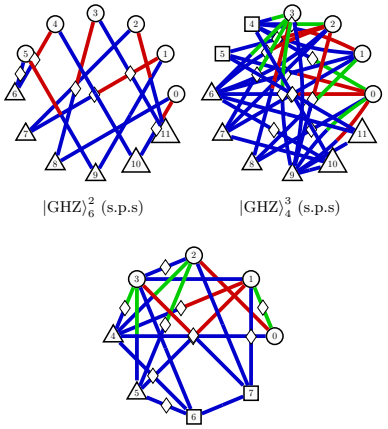

Figure 23: Graphs corresponding to the creation of three-, four- and five-particle GHZ states using single-photon sources.

perfect fidelity (F = 99%) for $w = 0.1$. There are cross-term that occur due to the lack of photon-number resolution. We want to acknowledge that the probability of a heralding event is very low for this example (P = 0.08%) and it is thus unlikely that this setup is experimentally feasible. As w approaches 0, fidelity approaches 100% but count-rate approaches 0. The trade-off between high fidelity and high count-rate is interesting to consider.

4.2 Maximizing Entanglement

When a quantum state cannot be expressed as the product of its parts, we call it entangled. However, if one asks *how* entangled a state is, the answer is not unique, there are multiple measures of entanglement. Here we present some of these metrics, together with states that are known to maximize them. Finally, we choose a particular metric and optimize a graph, not to reach a particular state – as done so far by maximizing the fidelity – but to instead maximize the entanglement metric itself. In this way, we will recover some well-known entangled states and also find new ones.

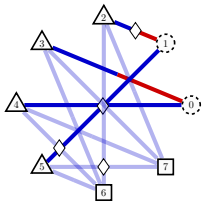

Figure 24: Graph corresponding to the creation of a heralded two-dimensional Bell state in the outgoing photons (0-1) from four single photon sources (2-5) and two heralding detectors (6-7). The heralding detectors do not require photon-number-resolution. The light edges have weights $w < 1$ corresponding to loss in the photon path.

4.2.1 Schmidt Rank Vector

Multiparticle entangled states in high dimensions allow for a much deeper structure underlying the potential ways in which the particles can be entangled. These structures can be characterized by the Schmidt Rank Vector (SRV) and give rise to new phenomena that only exist if both the number of particles and the number of dimensions go beyond two [147–149]. Here we consider tripartite states. The rank vector is a list of the ranks of the reduced density matrices. The state SRV(A,B,C) refers to a state, where

$$A = \mathrm{rank}(\rho_A), B = \mathrm{rank}(\rho_B), C = \mathrm{rank}(\rho_C),$$

and ρ_X is the density matrix of the system with the particle X traced out. In other words, the SRV is a vector of the dimensionalities of entanglement of every bipartition, which shows the dimensionality of entanglement between one particle and the rest of the quantum state. This master-slave-slave configuration is very useful for quantum applications such as layered quantum communication [150]. Taking a SRV(3,3,2) state as an example, we then know that the first two particles are both three-dimensionally entangled with the third particle, whereas the third one is only two-dimensionally entangled with the rest. The dimensionality for each particle cannot be increased with linear operations and classical communication (LOCC).

Searching the SRV(A,B,C) states has been investigated with the computer algorithm Melvin [25] and graph theory [34, 151]. Interestingly, it

has been shown from graph theory that without using any ancilla particles, there are several SRV(A,B,C) states that cannot be created. [34, 151]. Here we list these states (up to normalization):

26 SRV(5,5,4) :
$|000\rangle + |111\rangle + |222\rangle + |333\rangle + |443\rangle$

27 SRV(6,3,2) :
$|000\rangle + |101\rangle + |210\rangle + |311\rangle + |420\rangle + |521\rangle$

28 SRV(6,5,5) :
$|000\rangle + |111\rangle + |222\rangle + |334\rangle + |443\rangle + |544\rangle$

29 SRV(7,3,3) :
$|000\rangle + |101\rangle + |210\rangle + |311\rangle + |422\rangle + |520\rangle + |621\rangle$

It has been unknown whether we can experimentally create these states with additional particles, and this challenging question has been open for more than three years. Also, until now, SRV(A,B,C) states in high dimensional systems have only been recently demonstrated for SRV(3,3,2) [27], SRV(3,3,3) [28], and SRV(4,4,2) [152]. By using PyTheus, one can learn how to generate much more complex SRV states of high dimensions and more particles, such as the impossible states described in [34, 151]. We show the results in Fig. 25.

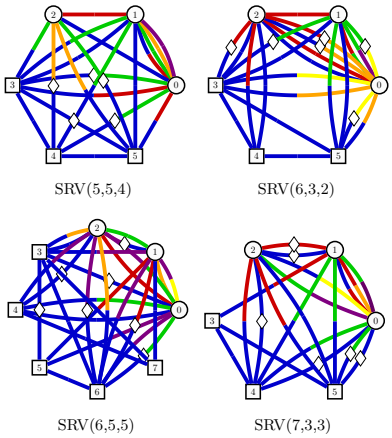

Figure 25: Graphs for producing SRV(A,B,C) states using ancillas.

4.2.2 Hyperdeterminant

Expanding the definition of determinant to tensors of arbitrary dimensions, we obtain *Hyperdeterminants* [153], which can also be used as an entanglement metric. In particular, the hyperdeterminant of a tensor $2\times2\times2\times2$ characterizes the entanglement of a 4 qubit state, which is maximal for the state (up to normalization) 30

$$|\mathrm{HD}\rangle = \left|\Psi^+00\right\rangle + \left|00\Psi^+\right\rangle + |1111\rangle\,, \qquad (31)$$

where $\sqrt{2}\,|\Psi^+\rangle = |01\rangle + |10\rangle$, and whose associated graph is shown in Fig. 26.

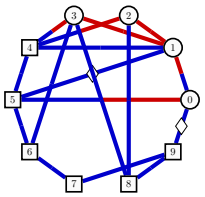

Figure 26: Graph to generate the state $|\mathrm{HD}\rangle$, which maximizes the hyperdeterminant.

4.2.3 Negative Partial Trace

Given a state ρ_{AB}, its *partial transpose* with respect to the subsystem A is

$$(\rho^{T_A})_{ab,mn} = \rho_{mb,an}. \qquad (32)$$

As shown by Peres, it is a necessary condition for the separability of A and B that none of the eigenvalues of ρ^{T_A} are negative [154]. Moreover, it is also a sufficient condition for bipartite states of dimensions 2×2 and 2×3 [155].

Aiming for highly entangled states, Brown et. al. looked for states of 2, 3, 4, and 5 qubits, whose partial traces for each bipartition had the lowest possible eigenvalues [156]. They called this metric

Negative Partial Trace, and it leads to the following states of 4 and 5 qubits [31] [32]

$$|\text{BSSB4}\rangle = |0000\rangle + |+011\rangle + |1101\rangle + |-110\rangle \quad (33)$$

$$|\text{BSSB5}\rangle = \left|000\Phi^+\right\rangle + |100\Phi^-\rangle + \left|010\Psi^+\right\rangle + |111\Psi^-\rangle\,. \quad (34)$$

Where $\sqrt{2}\,|\pm\rangle = |0\rangle \pm |1\rangle$, $\sqrt{2}\,|\Phi^\pm\rangle = |00\rangle \pm |11\rangle$, and $\sqrt{2}\,|\Psi^\pm\rangle = |01\rangle \pm |10\rangle$. These states can be produced with the graphs shown in Fig. 27.

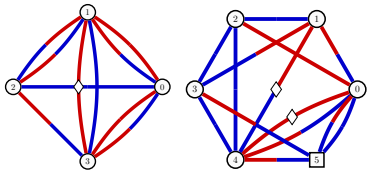

Figure 27: Graphs to generate the BSSB states of 4 and 5 qubits, respectively. The latter requires an ancilla.

4.2.4 Rényi Entropy

Among all the entanglement metrics in this document, as well as the ones that are left out, the *Rényi Entropy* is one of the most important [157]. Given a state with ρ_{AB}, the Rényi entropy of order α between the subsystems A and B is

$$\mathcal{S}_\alpha(\rho_A) = \frac{1}{1-\alpha}\log \text{Tr}(\rho_A^\alpha) = \mathcal{S}_\alpha(\rho_B), \quad (35)$$

where $\rho_A = \text{Tr}_B(\rho_{AB})$ and $\rho_B = \text{Tr}_A(\rho_{AB})$ are reduced density matrices. Similarly, the *Tsallis entropy* also describes the entanglement between A and B

$$\mathcal{T}_\alpha(\rho_A) = \frac{1}{1-\alpha}\left(\text{Tr}(\rho_A^\alpha) - 1\right) = \mathcal{T}_\alpha(\rho_B). \quad (36)$$

Notice that in the limit $\alpha \to 1$, both expressions approach the Von Neumann entropy.

A relevant difference between both metrics is that, for $\alpha > 1$, only the Tsallis entropy is convex while the Rényi one is Schur convex [158]. Taking this difference into account, Gour and Wallach showed that the 4-qubit state $|L\rangle$ maximizes the average of Tsallis entropies with $\alpha = 2$ for 2-qubit partitions [159], a metric of entanglement also referred to as the *Meyer-Wallach measure* [160, 161]. This state, created by the graph shown in Fig. 28, reads [33]

$$\begin{aligned}|\text{L}\rangle =&(1+\omega)(|0000\rangle + |1111\rangle)\\ &+(1-\omega)(|0011\rangle + |1100\rangle)\\ &+\omega^2(|0101\rangle + |0110\rangle + |1001\rangle + |1010\rangle),\end{aligned} \quad (37)$$

where $\omega = \exp(2i\pi/3)$.

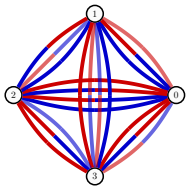

Figure 28: Graph to generate the 4-qubit L-state. All the weights in the graph are complex.

4.2.5 Rényi–Ingarden–Urbanik Entropy

Minimizing the Rényi entropy over all local unitary transformations U_{LOC}, Enriquez et. al. described the minimal *Rényi–Ingarden–Urbanik* entropy [162]

$$\mathcal{S}_\alpha^{\text{RIU}}(\phi) = \min_{U_{\text{LOC}}} \mathcal{S}_\alpha(p(U_{\text{LOC}}\,|\phi\rangle)), \quad (38)$$

where $\mathcal{S}_\alpha$ is the Rényi entropy of order $\alpha \geq 0$, and p is a normalized probability vector resulting from expanding the state to a product basis.

Together with the definition, the authors numerically find two states of three qubits that minimize the entropy for $\alpha = 1$ and $\alpha = 2$ [34] [35]

$$|\Phi\rangle_{\alpha=1} = 0.27\,|000\rangle + 0.377\,|100\rangle + 0.326\,|010\rangle + 0.363\,|001\rangle + 0.74e^{-0.79\pi i}\,|111\rangle\,, \quad (39)$$

$$|\Phi\rangle_{\alpha=2} = 0.438\,|000\rangle + 0.29\,|100\rangle + 0.371\,|010\rangle + 0.316\,|001\rangle + 0.698e^{-0.826\pi i}\,|111\rangle\,. \quad (40)$$

These states correspond to the graphs of Fig. 29.

4.2.6 Maximizing Entanglement for Each Partition

The previous states were maximally entangled according to different metrics. Indeed, many of them were found numerically when maximizing

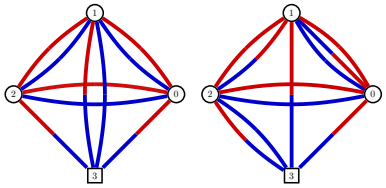

Figure 29: Graphs to generate the states that optimize the RIU entropy for $\alpha = 1$ and $\alpha = 2$.

such metrics. Similarly, we can use PyTheus to maximize arbitrary physical properties of the states produced by a graph, which can be immediately translated into experiments. This is a great advantage over previous work, in which an analytically described quantum state may not be experimentally feasible.

We optimize the graph according to the Tsallis entropy for $\alpha = 2$ (see Eq. (36)) using as loss function

$$\min_{\omega} \mathcal{L}(\rho(\omega)) = \sum_{A} \mathrm{Tr}\, \rho_A^2, \tag{41}$$

where $\rho = |\psi(\omega)\rangle\langle\psi(\omega)|$ is the state defined by a graph with weights $\{\omega\}$, ρ_A is the reduced density matrix with respect to a subsystem A. A subsystem and its complement A^c are a bipartition of the full system. The loss function is minimized for the sum of all bipartitions.

Given a bipartition, the entanglement between them is maximal if

$$\rho_A = \mathrm{Tr}_{A^c}(\rho) = \frac{1}{D}\mathbb{I}, \tag{42}$$

with D being the dimension of the Hilbert space in which ρ_A is defined, and $\mathbb{I}$ the identity matrix. Accordingly, multipartite states with maximal entanglement for every bipartition are called *Absolutely Maximally Entangled* (AME); such kinds of states have applications in quantum protocols like threshold secret sharing or open-destination teleportation [163]. On the other hand, given a state of N qudits, $\rho \in \mathcal{H}_d^{\otimes N}$, we call it *k-uniform* when the entanglement is maximal for all bipartitions of k qudits [164]. GHZ states of N-qudits (see Eq. (10)) are examples of 1-uniform states.

With PyTheus we can pick types of bipartitions the entanglement is to be maximized. Choosing all bipartitions targets the production

Dim	Number of particles								
	2	3	4	5	6	7	8	9	10
2	✓	✓	✗	✓	✓	✗	✗(3)	✓(3)	✗(3)
3	✓	✓	✓	✓	✓	✓	✗(3)	✓	✓
4	✓	✓	✓	✓	✓	✓	¿?	✓	✓
5	✓	✓	✓	✓	✓	✓	✓	✓	✓

Table 3: **Known AME states up to 10 particles and 5 dimensions.** ✗: no AME exist for the 2-dimensional systems of 4, 7, 8, and 10 particles, nor for the 3-dimensional system of 8 particles. **¿?**: it is unknown whether there is an AME for the 4-dimensional system of 8 particles. ✓: there exist an AME state for the rest of systems. For the 2-dimensional systems of 8, 9, and 10 particles, as well as for the 3-dimensional system of 8 particles, there exist a state with maximally entangled partitions of 3 particles [164, 165]. The existence of some of these state does not imply that they have been (or can be) experimentally realized.

of an AME state, bipartitions of size $|A| = k$ target k-uniform states. A mathematical result of entanglement theory is that AMEs only exist for certain combinations of N and d (see table 3). In such situations we choose to optimize for k-uniform states.

AME States – Since no AME exist for a system of four qubits (see table 3), we start optimizing the entanglement for all possible partitions for five qubits, obtaining two different AME states 36 37

$$\begin{aligned} |\mathrm{AME}(5,2)\rangle_a = &|00000\rangle + |01101\rangle + |01110\rangle \\ &+ |10110\rangle + |11000\rangle + |11011\rangle \\ &- |00011\rangle - |10101\rangle\,, \end{aligned} \tag{43}$$

$$\begin{aligned} |\mathrm{AME}(5,2)\rangle_b = &|01011\rangle + |01100\rangle + |10110\rangle \\ &+ |11010\rangle - |00000\rangle - |00111\rangle \\ &- |10001\rangle - |11101\rangle\,. \end{aligned} \tag{44}$$

For six qubits we found an asymptotic state 38

$$\begin{aligned} |\mathrm{AME}(6,2)\rangle \approx &|000010\rangle + |000100\rangle + |001001\rangle \\ &+ |010101\rangle + |011000\rangle + |011110\rangle \\ &+ |101010\rangle + |110000\rangle + |111011\rangle \\ &+ |111101\rangle - |001111\rangle - |010011\rangle \\ &- |100001\rangle - |100111\rangle - |101100\rangle \\ &- |110110\rangle + \varepsilon(|000000\rangle + |000110\rangle \\ &+ |010001\rangle + |010111\rangle + |110010\rangle \\ &+ |110100\rangle + |111001\rangle + |111111\rangle). \end{aligned} \tag{45}$$

This is not exactly the AME state of eight qubits, it has eight terms which vanish asymptotically as

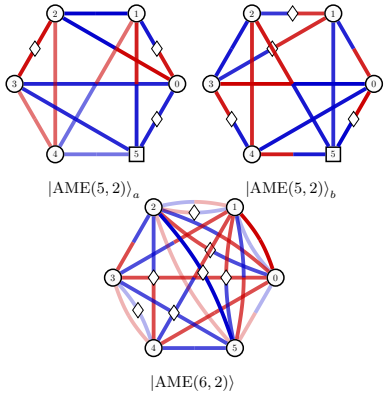

Figure 30: Absolutely Maximally Entangled states with 5 and 6 qubits. The 6-qubit graph produces an asymptotic state.

ε goes to zero. However, by doing so, we reduce the creation rate of the whole state. The graphs to produce this and the 5-qubits AME states are shown in Fig. 30.

k-Uniform States – While the AME solution for six qubits was asymptotic, we can generate the exact 2-uniform state of such a system [39]

$$\begin{aligned}|\mathrm{U2}\rangle_6^2 = &|100011\rangle + |101110\rangle - |000000\rangle \\ &- |001101\rangle - |010111\rangle - |011010\rangle \\ &- |110100\rangle - |111001\rangle\,. \end{aligned} \tag{46}$$

Twelve out of twenty three-qubit bipartitions of the above state are maximally entangled.

Similarly, we generated a 7-qubit state that maximizes the entanglement between each of the 21 possible $k = 2$ partitions except one [40]

$$\begin{aligned}|\sim \mathrm{U2}\rangle_7^2 = &|0011110\rangle + |0101000\rangle + |0110111\rangle \\ &+ |1001101\rangle + |1010010\rangle + |1100100\rangle \\ &- |0000001\rangle - |1111011\rangle\,. \end{aligned} \tag{47}$$

The graph to produce this 'almost' uniform state and the previous one are shown in Fig. 31.

Other States – As we have seen, even when an AME or k-uniform state for a given system of qudits exists, it is not always realizable with

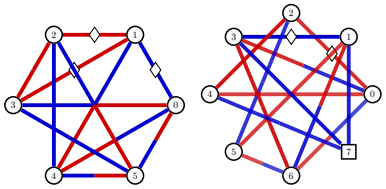

Figure 31: k=2 uniform state for 6 qubits and k=2 (almost) uniform state for 7 qubits (+ one ancilla).

linear optics. However, even if not perfect, we have found several highly entangled states which are worth mentioning. We refer to them as

$$|\mathrm{Ent(n,d,k)}\rangle\,, \tag{48}$$

where n stands for the number of particles, d for their dimensions, and k for the size of the partitions.

For a system of four qubits, we find two interesting states when maximizing the entanglement (see Eq. (41)) for every 2-qubit partition (see Fig. 32). We first optimize using real weights [41]

$$|\mathrm{Ent(4,2,2)}\rangle_{\mathbb{R}} = |1010\rangle + |1101\rangle - |0011\rangle - |0100\rangle\,, \tag{49}$$

obtaining a state which maximizes all possible partitions except one. For the second solution, we extend the weights to the complex domain, finding a local optimal [42]

$$\begin{aligned}|\mathrm{Ent(4,2,2)}\rangle_{\mathbb{C}} = &|0011\rangle + e^{-i0.54\pi}\,|0101\rangle \\ &+ e^{-i0.93\pi}\,|0110\rangle + e^{i0.45\pi}\,|1001\rangle \\ &+ e^{i0.71\pi}\,|1010\rangle + e^{i0.86\pi}\,|1100\rangle\,. \end{aligned} \tag{50}$$

This state minimizes the sum of partial traces for $k = 2$ partitions, following Eq. (41). However, while the sum its (locally) minimal, and all qubit partitions are equally entangled, they are not maximally entangled for $k = 2$. and all are equally for all $k = 1$ partitions and for none of the $k = 2$. However, all $k = 2$ partitions lead to the same value for the partial trace defined in Eq. (41). The entanglement seems to be 'equally distributed'.

The complex state in Eq. (50) gives the same entanglement structure as the Higuchi-Sudbery

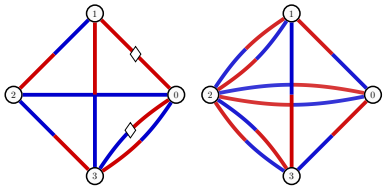

$|\mathrm{Ent}(4,2,2)\rangle_{\mathbb{R}}$ $|\mathrm{Ent}(4,2,2)\rangle_{\mathbb{C}}$

Figure 32: The graphs produced maximally entangled states for single qubit partitions on a 4 qubit system, they also present high entanglement between 2 qubit partitions (even if not maximal). The weights on the left graph are real, and the weights on the right graph are complex (the phase of every edge can be found in the repository).

state presented in [166]

$$|\mathrm{HS}\rangle = |0011\rangle + |1100\rangle + \omega(|1010\rangle + |0101\rangle) + \omega^2(|1001\rangle + |0110\rangle), \tag{51}$$

where $\omega = e^{i2\pi/3}$.

Finally, for a system of 8 qubits, PyTheus found a state for which 48 out of 56 total three-qubit bipartitions are maximally entangled. 43

$$\begin{aligned}|\mathrm{Ent}(8,2,3)\rangle = &|00010000\rangle + |00010111\rangle \\ &+ |01101011\rangle + |01101100\rangle \\ &+ |01110001\rangle + |10100010\rangle \\ &+ |10100101\rangle + |10111111\rangle \\ &+ |11000100\rangle + |11011001\rangle \\ &- |00001010\rangle - |00001101\rangle \\ &- |01110110\rangle - |10111000\rangle \\ &- |11000011\rangle - |11011110\rangle .\end{aligned} \tag{52}$$

The graph to produce this state is shown in Fig. 33.

It would be interesting to extend the maximization of other entanglement measures, such as experimental feasible, strong forms of all-vs-nothing violations [116], Hardy's version of local realism experiments which goes beyond the violations in Ref. [167, 168] (for example, by involving more particles), or other measures of quantum correlations. Such extensions would contribute to the study of artificial intelligence for the foundations of quantum mechanics [169].

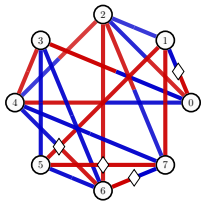

$|\mathrm{Ent}(8,2,3)\rangle$

Figure 33: The state generated by this graph is maximally entangled for 48 of the 56 possible 3-qubit partitions.

4.3 Generation of Mixed States

4.3.1 Werner State

The Werner state with the density matrix

$$\rho_\alpha = \alpha \left|\Phi^+\right\rangle \left\langle\Phi^+\right| + (1-\alpha)\frac{\mathbb{I}}{4}, \tag{53}$$

has different properties for different values of α. For $\alpha < 0.683$, it is known to be Bell-local. For $\alpha > 0.697$, it is known to be Bell nonlocal [170]. This leaves the gap between 0.683 and 0.697 open without a mathematical proof of its properties. By creating this state, it could be possible to test the Bell-locality of a state in the middle of the gap, $\alpha = 0.69$. The graph for the creation of this mixed state is shown in Fig. 34 44 .

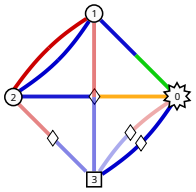

Figure 34: Graph for the Werner state with $\alpha = 0.69$. Information at vertex 0 is to be discarded. Vertex 3 is an ancillary detector

4.3.2 Counter-Example to the Peres Conjecture

Relations between different notions of quantum correlations are studied in quantum information theory. These insights are important to understand the underlying resources of quantum corre-

lations and their applicability in quantum protocols. In 1999, Asher Peres conjectured that the notion of Bell nonlocality and distillability is equivalent [118]. Bell nonlocality, as witnessed by a violation of Bell's inequality, says that no local hidden-variable model can explain the correlations observed in an experiment. A state is called distillable if a maximally entangled Bell pair can be extracted from multiple copies. The conjecture was open for 15 years until a counterexample was discovered in 2014, first for a strong version of the conjecture [119] and shortly after in its full form [120]. These violations are based on the uncovering of a two-particle bound state (a state that cannot be distilled) which can be used for quantum steering and violation of Bell's inequality. The Moroder-Gittsovich-Huber-Gühne-Vertesi-Brunner (MGHG-VB) state can be written as a mixed state that is an incoherent superposition of four entangled two-qutrit states, 45

$$\rho = \sum_{i=1}^{4} \lambda_i \left|\psi_i\right\rangle \left\langle\psi_i\right| \tag{54}$$

with $\lambda = \left(\frac{3257}{6884}, \frac{450}{1721}, \frac{450}{1721}, \frac{27}{6884}\right)$ and

$$\begin{aligned}
\left|\psi_1\right\rangle &= \frac{1}{\sqrt{2}}\left(\left|00\right\rangle + \left|11\right\rangle\right) \\
\left|\psi_2\right\rangle &= \frac{\sqrt{131}}{12\sqrt{2}}\left(\left|01\right\rangle + \left|10\right\rangle\right) + \frac{1}{60}\left|02\right\rangle - \frac{3}{10}\left|21\right\rangle \\
\left|\psi_3\right\rangle &= \frac{\sqrt{131}}{12\sqrt{2}}\left(\left|00\right\rangle - \left|11\right\rangle\right) + \frac{1}{60}\left|12\right\rangle - \frac{3}{10}\left|20\right\rangle \\
\left|\psi_4\right\rangle &= \frac{1}{\sqrt{3}}\left(-\left|01\right\rangle + \left|10\right\rangle + \left|22\right\rangle\right).
\end{aligned}$$

The graph that corresponds to this state is shown in Fig. 35. It might be interesting to generate this state and show experimentally that the state can violate Bell's inequality and thereby demonstrate an experimental falsification of Peres's conjecture.

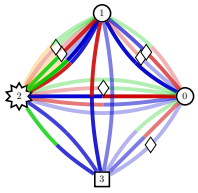

Figure 35: Graph for the Moroder-Gittsovich-Huber-Gühne-Vertesi-Brunner (MGHG-VB) state, which is a counter-example to the Peres conjecture. Here, vertex 3 is an ancilla photon and vertex 2 is the environment vertex. Due to the structure of the MGHG-VB state, the edge weights are not simple fractions.

4.4 Generation of Entanglement in the Photon-Number Basis

4.4.1 N00N States

The ability to perform precise measurements is always affected by several limitations, some of them avoidable by careful design of experiments and others of a fundamental nature. Classically, one can estimate a phase parameter more precisely by increasing the number of particles N in the measurement process; the precision is typically limited to $1/\sqrt{N}$, also known as the standard quantum limit (SQL). With the aid of quantum resources, one can beat the SQL, and the measurement precision can be enhanced to scale as $1/N$, approaching the Heisenberg limit that is governed by the physical law of quantum mechanics. One prominent representative of quantum states with the ability to break the SQL is the well-known N00N states [171, 8], as described in Eq. (8).

These N00N states can not only be used to test fundamental physics via violating Bell-type inequalities [172] but also play an important role in quantum-enhanced applications, quantum-enhanced microscopes and imaging systems [173–176], super-resolving phase measurements [177–180], and quantum lithography [181], to name a few. Interestingly, as the two-mode N00N states are formed in a superposition of two distinct states $|N,0\rangle$ and $|0,N\rangle$, one could consider that the two terms correspond to the "dead cat" and "alive cat" in the "Schrödinger-cat" form [86]. With high-N00N states, we might step closer to a better understanding of macroscopic entanglement envisioned by Schrödinger [182]. In the optical regime, achieving an efficient photonic source of N00N states with large N is very challenging. Several schemes and experiments have been toward the direction of generating photonic high-N00N states in different ways, such as by using strong optical nonlinearities [183], by linear optics and feed-forward [184], and by mixing coherent light with SPDC photon-pair sources on a standard beam splitter [185, 186, 86, 187].

Additionally, interest has also been growing in the simultaneous estimation of multiple parameters using multi-mode quantum states [82, 83]. Using a multimode N00N state, one can reach the Heisenberg limit with an $O(d)$ advantage over what is obtained with d copies of a two-mode N00N state [188, 189]. The generalization of the two-mode N00N states in Eq. (8) is given as [82, 83]

$$|\text{N00N}\rangle_d^N := \frac{1}{\sqrt{d}}(|N,0,...,0,0\rangle \pm |0,N,...,0,0\rangle \pm ... \pm |0,0,...,N,0\rangle \pm |0,0,...,0,N\rangle)_{1,...,d}. \tag{55}$$

Here we show how to produce perfect N00N states without using any coherent states or feed-forward. We list some examples that might give a different conceptual understanding and new insight. For more path-entangled states, one can directly employ PyTheus. For the ancillary detectors, we always assume they are reached by single photons, like in previous sections.

Two Particles – As we have introduced in section 2.1.4, the simplest N00N state is the $|\text{N00N}\rangle_2^2$ state that can be deterministically created via HOM interference when two indistinguishable photons are incident on a standard beam splitter simultaneously [87]. From the graph in Fig. 6, we can easily generalize the state to an arbitrary number of modes by adding more vertices, each one with a loop. The coherent superposition of a loop being in one of the vertices indicates the resulting multi-mode two-particle N00N states.

Three Particles – For producing 2-mode 3-photon N00N states $|\text{N00N}\rangle_2^3$, we additionally employ an ancilla particle in the experiment. We show the graph found by PyTheus in Fig. 36, which uses only one color, thus corresponding to the standard path-entangled N00N states. The edge can also be in different colors such that we are able to construct graphs for polarization-entangled N00N states [190–192]. We further explore the states in multi-mode cases, as described in Fig. 36 (b), (c) and (d) for 3-, 4-, 5-mode three-photon N00N states. Interestingly, the graphs found by PyTheus exhibit a nice structure, which may be amenable to generalization, to systematically produce other multi-mode NOON states without any optimization process.

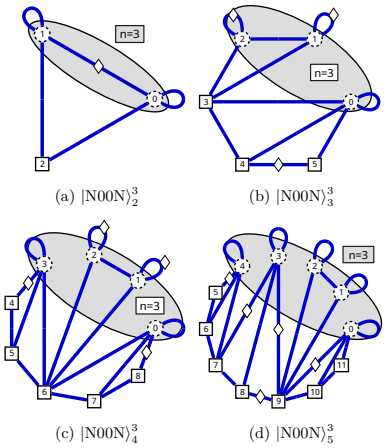

(a) $|\text{N00N}\rangle_2^3$ (b) $|\text{N00N}\rangle_3^3$

(c) $|\text{N00N}\rangle_4^3$ (d) $|\text{N00N}\rangle_5^3$

Figure 36: Graphs for multi-mode three-particle N00N states $|\text{N00N}\rangle_d^3$ with increasing number of ancillas.

Four Particles – For the previous N00N states, we optimized the graphs using real weights, finding the states $|40\rangle - |04\rangle$ and $|400\rangle - |040\rangle - |004\rangle$ [46] [47]. However, to generate the same N00N states with zero phase difference between the terms we need to, either add a $\pi/2$ phase on the solitary loops from Fig. 37 or, using only real weights, add 2 more ancillas. Additionally, after generating the 4-particle N00N states for 2 and 3 modes, it became obvious how to generate the graphs for an arbitrary number of modes.

It is worth noting that given a ket $|40\rangle$, each combination of non-repeating edges contributes twice as much as one with duplicate edges (assuming equal weights). This is a consequence of the multinomial theorem applied to the creation operators described in Eq. (2).

Other Two-Mode States – For the previous N00N states, the associated graphs have shown some patterns. The more obvious was the increasing need for ancillas, whether we were adding more photons or modes. Moreover, based

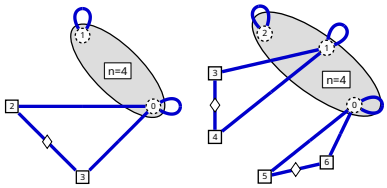

(a) $|40\rangle - |04\rangle$ (b) $|400\rangle - |040\rangle - |004\rangle$

Figure 37: Graphs with only real weights to generate 4-particle N00N states for 2 and 3 modes. Multiplying the i the loops of the disconnected vertices all the amplitudes of the state's terms become positive. To increase the number of modes, we add a triangular subgraph connected to a loop. The edge connecting the two new ancillas must be negative.

on a few graphs, we realized how to generate N00N states with 2 and 4 photons for an arbitrary number of modes. In Fig. 38 we show how to produce the two-mode N00N state for 5, 6, 7, and 8 photons 48 49 50 51. As with the 3-photon N00N states, it seems to be an underlying pattern in the graphs solutions when increasing the number of photons.

4.4.2 Platonic Solid States

We have been considering states where all N photons are in the same path, with the other paths empty. However, PyTheus can produce path-entangled states which do not fulfill such restrictions. Among them, a very special case leads to the highly symmetric Platonic Solid State [193–195], which can resolve rotations around any axis equally well. In the Platonic picture, shown in Fig. 39, an N-photon state is mapped onto N points on the Poincaré sphere [196], offering a systematic way for visualization. This also relates to a long-lasting problem of distributing N points on the Poincaré sphere in a highly symmetric fashion, where one can have many different solutions based on the function one tries to optimize [197, 198]. Additionally, the concept of Platonic solids has also been used for fundamental investigations in quantum physics [199, 200]. Apart from their symmetric elegance, there is plenty of room for applications of these states, for instance, in magnetometry, polarimetry, and metrology. Researchers have started investigating how to generate these Platonic solid state. In this part, we show the examples found by PyTheus.

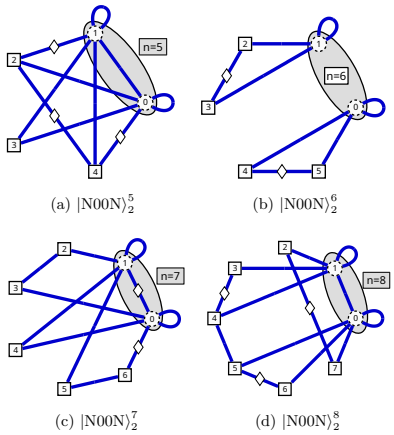

(a) $|\mathrm{N00N}\rangle_2^5$ (b) $|\mathrm{N00N}\rangle_2^6$

(c) $|\mathrm{N00N}\rangle_2^7$ (d) $|\mathrm{N00N}\rangle_2^8$

Figure 38: Graphs for two-mode N00N states of 5, 6, 7, and 8 photons.

Tetrahedron – Our first Platonic solid state is the tetrahedron [201], which is the unique optimal four-photon state for characterizing polarization rotations. The state written in the Fock basis reads as

$$\left|\Psi^{(1)}\right\rangle = \frac{1}{\sqrt{3}}(|4,0\rangle + \sqrt{2}\,|1,3\rangle). \tag{56}$$

It can be produced by the graph in Fig. 39 (top panels), and has already been implemented [202].

The similarity between the graphs that produce the tetrahedron and the three-photon N00N state discovered by PyTheus (see Fig. 36 a) shows a nice pattern: to generate states in the Fock basis, we can add an arbitrary number of photons to any path. In this way, starting with a general state $|\mathrm{M,N}\rangle \pm |\mathrm{N,M}\rangle$, we can obtain

$$|\mathrm{M,N}\rangle \pm |\mathrm{N,M}\rangle \Rightarrow |\mathrm{M+x,N+y}\rangle \pm |\mathrm{N+x,M+y}\rangle\,. \tag{57}$$

We only need to connect the first and second paths to x and y ancillary photons, respectively. This construction can be used for an arbitrary number of modes.

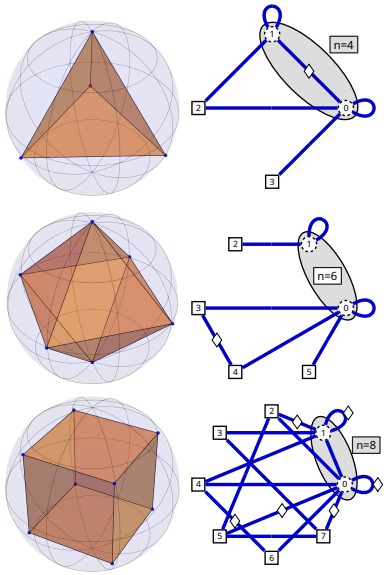

Figure 39: Graphs for producing tetrahedron, octahedron, and cube quantum states.

Octahedron – The octahedron state reads

$$\left|\Psi^{(2)}\right\rangle = \frac{1}{\sqrt{2}}(|5,1\rangle - |1,5\rangle), \tag{58}$$

and was found by PyTheus using only 4 ancillary detectors (see Fig. 39). Alternatively, we can apply the pattern described in Eq. (57) to the graph that produces $|40\rangle - |04\rangle$, which is shown in Fig. 37 a).

Cube – The last platonic solid we are able to produce is the cube state, which reads 52

$$\left|\Psi^{(3)}\right\rangle = \frac{\sqrt{3}}{12}(\sqrt{10}\,|8,0\rangle + 2\sqrt{7}\,|4,4\rangle + \sqrt{10}\,|0,8\rangle). \tag{59}$$

In Fig. 39, we show the graph that can be used to generate the cube state. As we can see from the expression and Fig. 39 (bottom), the graph cannot be obtained by modifying one of the previous graphs for a two-mode N00N state.

4.5 Towards Quantum Simulation

In this section, we present quantum state generation for states from condensed matter physics which could be interesting for quantum simulation[203]. The quantum entangled states of few- or many-body systems can generally be expressed by the tensor network formulations [204, 205]. One of the most successful members of this family with a vast application in condensed matter physics is the 1D matrix product state (MPS). Here one represents the quantum state of a system with periodic boundary conditions and N particles as

$$|\psi\rangle = \sum_{s} \mathrm{tr}\left[A_1^{(s_1)} A_2^{(s_2)} \dots A_N^{(s_N)}\right] |s_1 \dots s_N\rangle\,, \tag{60}$$

where $s_i = \{0, \dots d-1\}$ denotes the local state of the ith particle with local physical dimension d. Here $A_i^{(s_i)}$ is a complex matrix with dimension χ, also known as the bond (virtual) dimension. The matrix $A_i^{(s_i)}$ can be viewed as a projector from a χ-dimensional virtual (correlation) vector space into the physical d-dimensional space [206]. While in non-interacting systems, described by product states, the bond dimension χ is one, this quantity grows exponentially with N in most strongly correlated systems. This results in employing numerical techniques to (approximately) obtain the ground states of most many-body systems. Nevertheless, one can find multiple few- or many-body ground states with $\chi > 1$ but independent of the particle number. Here, we present a collection of these ground states with a concise description of their host Hamiltonian and their physical implication upon realization. While our focus is on zero-temperature ground states, we emphasize that the applicability of PyTheus is not limited to these states. This is because both mixed states 2.1.3, which describe open quantum states, and states constitute combinations of (various) Fock states 2.1.4, can be used to study the (grand) canonical ensemble, are treatable by PyTheus.

4.5.1 Spin-1/2 Systems

Due to the simplicity of spin-1/2 systems and the surge of interest in qubit quantum computation, these many-body systems received ever-growing attention. The local physical space of

these systems spanned by $\{|\uparrow\rangle, |\downarrow\rangle\}$, or equivalently $\{|0\rangle, |1\rangle\}$, results in the local physical dimension $d = 2$. Despite such a small physical dimension, the obtained ground states can be rich and exotic. In the following, we list some of these states.

Spin-1/2 Wire – A computational quantum spin-1/2 wire governed by nearest-neighbor interactions, associated with non-zero two-point correlation functions and arbitrary local entanglement, is described by [207, 206]

$$|\psi\rangle = \sum_{s_i=0}^{1} \mathrm{tr}[A(s_{n-1}) \dots A(s_1)] \, |s_1 \dots s_n\rangle \,, \quad (61)$$

where

$$A(\uparrow) = \frac{1}{\sqrt{2}} G, \quad G = \exp(\mathrm{i}\pi\sigma^x/\tau), \quad (62)$$

$$A(\downarrow) = \frac{1}{\sqrt{2}} GT(\phi), \quad T = \begin{pmatrix} e^{-\mathrm{i}\phi/2} & 0 \\ 0 & e^{\mathrm{i}\phi/2} \end{pmatrix}, \quad (63)$$

where ϕ and τ denote the entanglement factor and period, respectively.

Fig. 40 displays the associated graph for the ground state of the spin-1/2 wire for four particles with $\phi = \pi/2$. The state, up to normalization, reads 53

$$\begin{aligned} |\psi\rangle = \sqrt{2}\,|0000\rangle + |0001\rangle + |0010\rangle + |0100\rangle \\ - |0111\rangle + |1000\rangle - |1011\rangle \\ - |1101\rangle - |1110\rangle - \sqrt{2}\,|1111\rangle \,. \end{aligned} \quad (64)$$

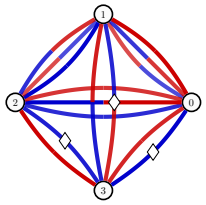

Figure 40: The associated graph for the ground state of the spin-1/2 wire with four particles.

Spin-1/2 States with No Adjacent Spin-ups – Aside from the previous spin-1/2 state, one can compute entangled states where no two neighboring spin-ups appear in the ground state. One can expect to detect these states in spin systems with nearest-neighbor interactions. In the Rydberg-atom experiments, this situation occurs due to the Rydberg blockade [208]. The matrix product representation of these states reads

$$|\psi\rangle = \sum_{s_i=0}^{1} \mathrm{tr}[A(s_{n-1}) \dots A(s_1)] \, |s_1 \dots s_n\rangle \,, \quad (65)$$

where

$$A(\uparrow) = \frac{1}{\sqrt{2}}(\mathbb{I} + \sigma^x), \quad (66)$$

$$A(\downarrow) = 2\sigma^+, \quad (67)$$

with $\sigma^+ = \sigma^x + \mathrm{i}\sigma^y$.

Fig. 41 displays the associated graphs for this system with various numbers of particles whose ground states read

- 54 Three particles with one ancillary particle:

$$|\psi_3\rangle = |000\rangle + |001\rangle + |010\rangle + |100\rangle \,. \quad (68)$$

- 55 Four particles:

$$\begin{aligned} |\psi_4\rangle = |0000\rangle + |0001\rangle + |0010\rangle \\ + |0100\rangle + |0101\rangle + |1000\rangle + |1010\rangle \,. \end{aligned} \quad (69)$$

- 56 Five particles with one ancillary particle:

$$\begin{aligned} |\psi_5\rangle = |00000\rangle + |00001\rangle + |00010\rangle \\ + |00100\rangle + |00101\rangle + |01000\rangle \\ + |01001\rangle + |01010\rangle + |10000\rangle \\ + |10010\rangle + |10100\rangle \,. \end{aligned} \quad (70)$$

- 57 Six particles:

$$\begin{aligned} |\psi_6\rangle = |000000\rangle + |000001\rangle + |000010\rangle \\ + |000100\rangle + |000101\rangle + |001000\rangle \\ + |001001\rangle + |001010\rangle + |010000\rangle \\ + |010001\rangle + |010010\rangle + |010100\rangle \\ + |010101\rangle + |100000\rangle + |100010\rangle \\ + |100100\rangle + |101000\rangle + |101010\rangle \,. \end{aligned} \quad (71)$$

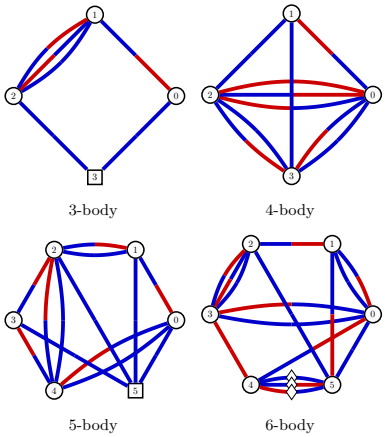

Figure 41: Associated graphs for spin-1/2 states with no adjacent spin-ups for three, four, five, and six particles. One ancillary particle is included in states with an odd number of particles (left column).

Majumdar-Gosh Model – The one-dimensional quantum Heisenberg spin model is known as the Majumdar-Gosh model when the value of the next-nearest-neighbor interaction is half the value of the nearest-neighbor antiferromagnetic exchange interaction. The Hamiltonian of this model casts [209]

$$H = \sum_i 2\overrightarrow{\sigma}_i \cdot \overrightarrow{\sigma}_{i+1} + \overrightarrow{\sigma}_i \cdot \overrightarrow{\sigma}_{i+2}, \tag{72}$$

where $\overrightarrow{\sigma}_i = (\sigma_i^x, \sigma_i^y, \sigma_i^z)$.

The ground states of this model Hamiltonian are dimerized states given by products of singlet configurations of spins on neighboring sites. The linear combination of these states reads [209]

$$|\psi\rangle = \sum_{s_i=0}^{1} \mathrm{tr}[A(s_{n-1}) \dots A(s_1)] \, |s_1 \dots s_n\rangle \,, \tag{73}$$

where

$$A^{\uparrow} = \begin{pmatrix} 0 & 1 & 0 \\ 0 & 0 & 0 \\ \frac{1}{\sqrt{2}} & 0 & 0 \end{pmatrix}, \quad A^{\downarrow} = \begin{pmatrix} 0 & 0 & 1 \\ -\frac{1}{\sqrt{2}} & 0 & 0 \\ 0 & 0 & 0 \end{pmatrix}. \tag{74}$$

This ground state of the Majumdar-Gosh model is one of the simplest spin-1/2 valence-bond solids in one-dimensional systems.

Fig. 42 displays the associated graphs for the four- and six-particle systems whose ground states read

- 58 Four particles:

$$\begin{aligned} \left|\psi^{(4)}\right\rangle = &|0011\rangle - 2\,|0101\rangle + |0110\rangle \\ &+ |1100\rangle - 2\,|1010\rangle + |1001\rangle \,. \end{aligned} \tag{75}$$

- 59 Six particles with two ancillary particles:

$$\begin{aligned} \left|\psi^{(6)}\right\rangle = &|001011\rangle - |001101\rangle \\ &- |010011\rangle + |010110\rangle \\ &+ |011001\rangle - |011010\rangle \\ &+ |100101\rangle - |100110\rangle \\ &- |101001\rangle + |101100\rangle \\ &+ |110010\rangle - |110100\rangle \,. \end{aligned} \tag{76}$$

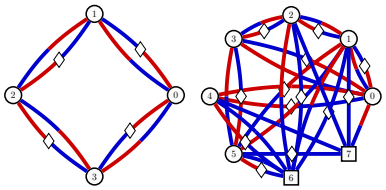

Figure 42: Ground states of the Majumdar-Gosh model with four (left panel) and six (right) particles. Two ancillary particles are included in the right panel.

Dyck Words – The Fredkin spin-1/2 model with a three-body interaction term reads [210–213]

$$\mathcal{H} = \sum_i U_{i-1} P_{i,i+1} + P_{i-1,i} D_{i+1}, \tag{77}$$

where $U_i = |\uparrow_i\rangle\langle\uparrow_i|$, $D_i = |\downarrow_i\rangle\langle\downarrow_i|$ and the spin-singlet projector reads $P_{i,i+1} = |S_{i,i+1}\rangle\langle S_{i,i+1}|$ with $|S_{i,j}\rangle = (|\uparrow_i\rangle\langle\downarrow_j| - |\downarrow_i\rangle\langle\uparrow_j|)$. The ground state of this model is an equally weighted superposition of spin configurations forming Dyck words. Here one may use the notation $|\uparrow\rangle = |(\rangle$ and $|\downarrow\rangle = |)\rangle$ to translate the spin states into the Dyck words. In this notation, the ground state forms balanced strings whose segments contain equal numbers of open and closed parentheses. The ground states of the Fredkin model with six and eight particles cast

- 60 Six particles:

$$\left|\psi^{(6)}\right\rangle = \frac{1}{\sqrt{5}}[\,|()()()\rangle + |()(())\rangle + |(())()\rangle + |(()())\rangle + |((()))\rangle\,]. \quad (78)$$

- 61 Eight particles:

$$\begin{aligned}\left|\psi^{(6)}\right\rangle = \frac{1}{\sqrt{14}}[\,&|(()())()\rangle + |(()()())\rangle \\ &+ |(()(()))\rangle + |((()))()\rangle \\ &+ |((())())\rangle + |((()()))\rangle \\ &+ |(((())))\rangle + |()()()()\rangle \\ &+ |()()(())\rangle + |()(())()\rangle \\ &+ |()(()())\rangle + |()((()))\rangle \\ &+ |(())()()\rangle + |(())(())\rangle\,]. \end{aligned} \quad (79)$$

The associated graphs for these states are shown in Fig. 43.

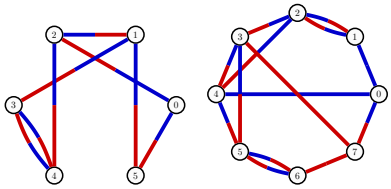

Dyck Word with six letters Dyck Word with eight letters

Figure 43: The graphs corresponding to the creation of Dyck word states.

4.5.2 Spin-1 Systems

The quest to go beyond the two-level qubit systems in quantum computation put forward other proposals based on three-level qutrit quantum states [214, 215]. In spin systems, this inquiry is translated into exploring the $S = 1$ space spanned by $\{|-1\rangle, |0\rangle, |1\rangle\}$ with physical dimension $d = 3$. While spin-1 states can be realized experimentally in a controlled fashion [216], often, one may encounter these states as emergent phenomena in various spin-1/2 condensed matter systems, e.g., in describing the low-energy physics of chiral threefold fermions [217]. As a result, aside from technological implications, exploring the higher-spin systems may shed light on a better understanding of some emergent phenomena in other fields of physics.

Spin-1 Wire – The antiferromagnetic ground state of a spin-1 chain with nearest-neighbor interactions can be represented in the matrix product form as [218]

$$|\psi\rangle = \mathrm{tr}(A_1 A_2 \dots A_N), \quad (80)$$

where

$$A_i = \begin{pmatrix} |0\rangle & -\sqrt{a}\,|+1\rangle \\ \sqrt{a}\,|-1\rangle & -\sigma\,|0\rangle \end{pmatrix}, \quad (81)$$

with nonvanishing a and σ.

Fig. 44 displays the associated graph with one ancilla, for the ground states of the spin-1 chain with three particles, which, up to normalization, reads 62

$$\begin{aligned}|\psi\rangle = 0.3(&|012\rangle + |120\rangle + |201\rangle) - 0.875\,|111\rangle \\ &- 0.15(|021\rangle + |102\rangle + |210\rangle). \end{aligned} \quad (82)$$

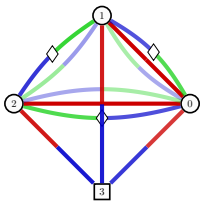

Figure 44: The associated graph for the ground states of the spin-1 chain with three particles.

Affleck-Kennedy-Lieb-Tasaki Model – A particular spin-1 bilinear biquadratic Hamiltonian introduced by Affleck, Kennedy, Lieb, and Tasaki (AKLT) is given by [219, 220]

$$H = \sum_i \vec{S}_i \cdot \vec{S}_{i+1} + \frac{1}{3}(\vec{S}_i \cdot \vec{S}_{i+1})^2. \quad (83)$$

The ground state of this solvable model, known as the AKLT state, is short-range entangled and classified in symmetry-protected-topological states [221]. The MPS representation of this state reads [209, 204]

$$|\psi\rangle = \sum_{s_i=0}^{1} \mathrm{tr}[A(s_{n-1}) \dots A(s_1)]\,|s_1 \dots s_n\rangle\,, \quad (84)$$

where $s_i \in \{0, 1\}$ and

$$\{A_{-1}, A_0, A_{+1}\} = \{\sqrt{\frac{2}{3}}\sigma^+, \frac{1}{\sqrt{3}}\sigma^z, -\sqrt{\frac{2}{3}}\sigma^-\}. \tag{85}$$

Here $\sigma^\pm = \sigma^x \pm \mathrm{i}\sigma^y$. The AKLT state is the spin-1 valance bond solids [222].

Fig. 45 displays the associated graphs for the three- and four-particle AKLT system whose ground states read, up to normalization 63 64

$$\begin{aligned}\left|\psi^{(3)}\right\rangle &= |0,-1,+1\rangle - |-1,0,+1\rangle \\ &+ |-1,+1,0\rangle - |0,+1,-1\rangle \\ &+ |+1,0,-1\rangle - |+1,-1,0\rangle\,, \end{aligned} \tag{86}$$

$$\begin{aligned}\left|\psi^{(4)}\right\rangle &= 2(|-1,1,-1,1\rangle + |1,-1,1,-1\rangle) \\ &+ |1,0,-1,0\rangle - |1,-1,0,0\rangle \\ &+ |0,1,0,-1\rangle - |0,1,-1,0\rangle \\ &- |0,0,1,-1\rangle + |0,0,0,0\rangle \\ &- |0,0,-1,1\rangle - |0,-1,1,0\rangle \\ &+ |0,-1,0,1\rangle - |-1,1,0,0\rangle \\ &- |1,0,0,-1\rangle + |-1,0,1,0\rangle \\ &- |-1,0,0,1\rangle\,. \end{aligned} \tag{87}$$

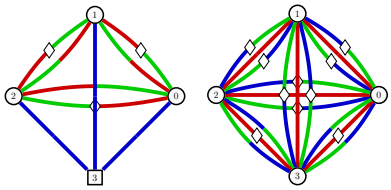

Figure 45: The associated graphs for the ground state of the spin-1 AKLT state with three and four particles. One ancillary particle is included in the first state.

Motzkin State – The spin-1 generalization of the Dyck words is known as the Motzkin State [211, 223, 224]. The spin configurations, in this case, can be translated into strings using $|-1\rangle = |)\rangle$, $|0\rangle = |-\rangle$, and $|1\rangle = |(\rangle$. Here, similar to the Dyck words, the number of open and closed parentheses is equal. Examples of such states cast

- 65 Three particles:

$$|\psi\rangle = \frac{1}{2}[|---\rangle + |()-\rangle + |(-)\rangle + |-()\rangle]. \tag{88}$$

- 66 Four particles:

$$\begin{aligned}|\psi\rangle = \frac{1}{\sqrt{9}}[&|----\rangle + |()--\rangle + |-()-\rangle \\ &+ |--()\rangle + |(--)\rangle + |()()\rangle \\ &+ |-(-)\rangle + |(-)-\rangle + |(())\rangle]. \end{aligned} \tag{89}$$

The associated graphs for these states are presented in Fig. 46.

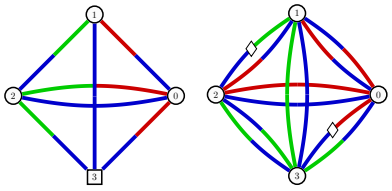

Figure 46: The graphs corresponding to the creation of Motzkin states.

4.5.3 Spin-3/2 Systems

Sharing the same motivation as spin-1 systems, the four-level spin-3/2 systems have putative implications in qudits with $d = 4$ quantum computation [225]. The local Hilbert space of these spin-3/2 systems are spanned by $\{|1\rangle, |-1\rangle, |3\rangle, |-3\rangle\}$ resulting in local physical dimension $d = 4$.

Spin-3/2 Wire – Two exact ground states for a spin-3/2 chain with ferromagnetic character are shown to have the following matrix product representation [226, 227]

$$|\psi^\pm\rangle = \mathrm{tr}\left(A_1^\pm A_2^\pm \dots A_N^\pm\right), \tag{90}$$

where

$$A^+ = \begin{pmatrix} |1\rangle & -\sqrt{3}\,|3\rangle \\ |-1\rangle & -|1\rangle \end{pmatrix},\ A^- = \begin{pmatrix} -|-1\rangle & |1\rangle \\ -\sqrt{3}\,|-3\rangle & |-1\rangle \end{pmatrix}. \tag{91}$$

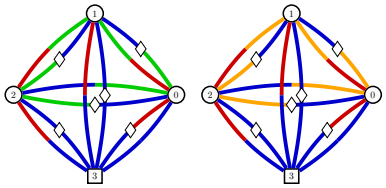

Figure 47: The associated graphs for the ground states of the spin-3/2 chain for three particles.

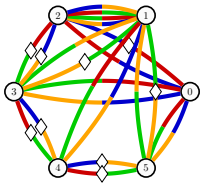

Spin-3/2 letter state with six letters

Figure 48: The graphs corresponding to the creation of the spin-3/2 letter state.

The ground states of the spin-3/2 chain, up to normalization, reads [67]

$$|\psi^{\pm}\rangle = |-1,1,\pm 3\rangle - |1,-1,\pm 3\rangle + |1,\pm 3,-1\rangle - |-1,\pm 3,1\rangle + |\pm 3,-1,1\rangle - |\pm 3,1,-1\rangle . \tag{92}$$

As one ground state, say $|\psi^+\rangle$, can be achieved from the other ground state, $|\psi^-\rangle$, by merely replacing $|3\rangle$ with $|-3\rangle$, we only present the associated graph for $|\psi^+\rangle$ with three particles and one ancilla in Fig. 47.

Spin-3/2 Letter State – As a straightforward generalization of the Dyck words and Motzkin letter states, discussed previously, one can introduce the letter states for the spin-3/2 states. Here one should translate the spin state into the letters as $|-3\rangle = |[\rangle$, $|-1\rangle = |\langle\rangle$, $|1\rangle = |\rangle\rangle$ and $|3\rangle = |]\rangle$. Using this language, the six particle state is [68]

$$\begin{aligned}|\psi\rangle =& \frac{1}{\sqrt{40}}[|()()()\rangle + |()[]()\rangle + |[]()()\rangle + |()()[]\rangle \\ &+ |[][]()\rangle + |[]()[]\rangle + |()[][]\rangle + |[][][]\rangle \\ &+ |(())()\rangle + |(())[]\rangle + |([])()\rangle + |[()]()\rangle \\ &+ |[()][]\rangle + |[[]]()\rangle + |([])[]\rangle + |[[]][]\rangle \\ &+ |()(())\rangle + |[](())\rangle + |()([])\rangle + |()[()]\rangle \\ &+ |[][()]\rangle + |[]([])\rangle + |()[[]]\rangle + |[][[]]\rangle \\ &+ |(()())\rangle + |[()()]\rangle + |([]())\rangle + |(())[]\rangle \\ &+ |([][])\rangle + |[[]()]\rangle + |[()[]]\rangle + |[[][]]\rangle \\ &+ |((()))\rangle + |(([]))\rangle + |([()])\rangle + |[(())]\rangle \\ &+ |([[]])\rangle + |[([])]\rangle + |[[()]]\rangle + |[[[]]]\rangle].\end{aligned} \tag{93}$$

The associated graph for this state is shown in Fig. 48.

4.5.4 Spin-2 Systems

Five-level computational units can further be of interest in quantum computation beyond qubits. The local physical space of these spin-2 units is spanned by $\{|-2\rangle, |-1\rangle, |0\rangle, |1\rangle, |2\rangle\}$ with local physical dimension $d = 5$. Similar to other higher-spin systems in condensed matter systems, spin-2 states can also be viewed as emergent states in some (lower-spin with $S < 2$) many-body systems [228].

Spin-2 Wire – The anisotropic spin-2 chain with nearest-neighbour interactions hosts various phases depending on three parameters (a, x, σ) with $a \in \mathbb{R}, \sigma = \pm 1$ [229]. These phases consist of three distinct antiferromagnetic Haldane phases and a weak antiferromagnetic phase.

The ground states of the weak-antiferromagnetic phase have the following matrix product representation:

$$\left|\psi_0^{(1)}\right\rangle = \mathrm{tr}\left[\prod_{i=1}^{L/2} m_{2i-1} g_{2i}\right], \tag{94}$$

$$\left|\psi_0^{(2)}\right\rangle = \mathrm{tr}\left[\prod_{i=1}^{L/2} g_{2i-1} m_{2i}\right], \tag{95}$$

where

$$m = \begin{pmatrix} |1\rangle & x\sqrt{a}\,|2\rangle \\ \sqrt{a}\,|0\rangle & |1\rangle \end{pmatrix}, \; g = \begin{pmatrix} |-1\rangle & \sqrt{a}\,|0\rangle \\ x\sqrt{a}\,|-2\rangle & |-1\rangle \end{pmatrix}. \tag{96}$$

Here we set $a = 0.5$.

When the translational symmetry is not broken, i.e., $x = 1$, two more states can also be iden-

tified for this phase, given by

$$\left|\psi_0^{(3)}\right\rangle = \mathrm{tr}\left[\prod_{i=1}^{L} m_i^{x=1}\right], \quad \left|\psi_0^{(4)}\right\rangle = \mathrm{tr}\left[\prod_{i=1}^{L} g_i^{x=1}\right]. \tag{97}$$

Fig. 49 displays the associated graphs for the three-particle ground states of the weak-antiferromagnetic phase when the translational symmetry is broken (top panel) and respected (bottom). The states with broken translation symmetry, up to normalization, read 69

$$\begin{aligned}\left|\psi_0^{(1)}\right\rangle =& 0.5(|2,-1,0\rangle + |0,-1,2\rangle) \\ &+0.25(|2,-2,1\rangle + |1,-2,2\rangle) \\ &+|1,0,0\rangle + |0,0,1\rangle + 4\,|1,-1,1\rangle\,, \end{aligned} \tag{98}$$

$$\begin{aligned}\left|\psi_0^{(2)}\right\rangle =& |-1,0,0\rangle + |0,0,-1\rangle + 4\,|-1,1,-1\rangle \\ &+0.25(|-2,2,-1\rangle + |-1,2,-2\rangle) \\ &+0.5(|-2,1,0\rangle + |0,1,-2\rangle). \end{aligned} \tag{99}$$

When the symmetry is respected, the states, up to normalization, are 70

$$\begin{aligned}\left|\psi_0^{(3)}\right\rangle =& |0,1,2\rangle + |0,2,1\rangle + |1,0,2\rangle + |2,1,0\rangle \\ &+|1,2,0\rangle + |2,0,1\rangle + 4\,|1,1,1\rangle\,, \end{aligned} \tag{100}$$

$$\begin{aligned}\left|\psi_0^{(4)}\right\rangle =& |0,-1,-2\rangle + |0,-2,-1\rangle + |-1,0,-2\rangle \\ &+|-2,-1,0\rangle + |-1,-2,0\rangle \\ &+|-2,0,-1\rangle + 4\,|-1,-1,-1\rangle\,. \end{aligned} \tag{101}$$

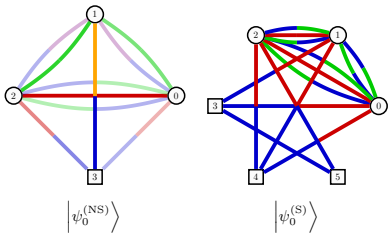

Figure 49: The associated graphs for the three-particle ground states of the weak-antiferromagnetic phase when the translational symmetry is broken (left) and respected (right).

The Haldane-antiferromagnetic-A is another possible phase in this spin-2 system described by the ground state

$$|\psi\rangle = \sum_{s_i=-2}^{2} \mathrm{tr}\left[A_1^{s_1} A_2^{s_2} \dots A_N^{s_N}\right] |s_1, s_2, \dots s_N\rangle\,, \tag{102}$$

where

$$\sum_{s_m=-2}^{2} A_m^{s_m} = \begin{pmatrix} |0\rangle & \sqrt{x}\,|1\rangle & a\,|2\rangle \\ \sqrt{x}\,|-1\rangle & \gamma\,|0\rangle & \sqrt{x}\,|1\rangle \\ a\,|-2\rangle & \sqrt{x}\,|-1\rangle & |0\rangle \end{pmatrix}. \tag{103}$$

Fig. 50 displays the graph associated with the ground state, with three particles and five ancillas, for the Haldane-antiferromagnetic-A phase. Up to normalization, the state reads 71

$$\begin{aligned}|\psi_A\rangle =& |-1,0,1\rangle + |-1,1,0\rangle + |0,-1,1\rangle \\ &+|0,1,-1\rangle + |1,-1,0\rangle + |1,0,-1\rangle \\ &+0.5(|-2,0,2\rangle + |0,-2,2\rangle + |-2,2,0\rangle) \\ &+0.5(|2,0,-2\rangle + |0,2,-2\rangle + |2,-2,0\rangle) \\ &+0.25(|1,-2,1\rangle + |-1,-1,2\rangle + |-1,2,-1\rangle) \\ &+0.25(|1,1,-2\rangle + |-2,1,1\rangle + |2,-1,-1\rangle) \\ &+6\,|0,0,0\rangle\,. \end{aligned} \tag{104}$$

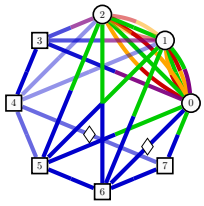

Figure 50: The associated graph for the three-particle ground state of the Haldane-antiferromagnetic-A phase.

The ground states of the second antiferromagnetic Haldane phase, referred to as Haldane-antiferromagnetic-B, reads

$$|\psi_B\rangle = \sum_{s_i=-1}^{1} \mathrm{tr}\left[A_1^{s_1} A_2^{s_2} \dots A_N^{s_N}\right] |s_1, s_2, \dots s_N\rangle\,, \tag{105}$$

where

$$\sum_{s_m=-1}^{1} A_m^{s_m} = \begin{pmatrix} |0\rangle & \sqrt{a}\,|1\rangle \\ \sqrt{a}\,|-1\rangle & \sigma\,|0\rangle \end{pmatrix}. \tag{106}$$

Similarly, the ground state of the third Haldane-antiferromagnetic phase, known as Haldane-antiferromagnetic-C, is

$$|\psi_C\rangle = \sum_{s_i\in\{0,\pm 2\}} \mathrm{tr}\left[A_1^{s_1}A_2^{s_2}\dots A_N^{s_N}\right]|s_1,s_2,\dots s_N\rangle\,, \tag{107}$$

where

$$\sum_{s_i\in\{0,\pm 2\}} A_m^{s_m} = \begin{pmatrix} |0\rangle & \sqrt{a}\,|2\rangle \\ \sqrt{a}\,|-2\rangle & \sigma\,|0\rangle \end{pmatrix}. \tag{108}$$

Notice that the last Haldane phases, B and C, have essentially the same Hamiltonian as the weak-antiferromagnetic phase when the translational symmetry is preserved (see Eq. (101)). One can obtain one from the other by performing $|\pm 1\rangle \leftrightarrow |\pm 2\rangle$.

4.5.5 Quantum Many-Body Scars

The phenomena in which weakly entangled nonthermal quantum eigenstates are embedded in the eigensystem of non-integrable (thermal) systems is dubbed 'quantum many-body scars' [230]. The well-known examples of these scar states are shown to be present in the AKLT spin chain models [231, 232]. The experimental realizations of such states are also reported in Rydberg-atom quantum simulators [208, 233]. In the following, we suggest that one may also detect these states using quantum optics experiments.

Onsager's Scars in Disordered Spin Chains – A non-integrable quantum spin chain that exhibits quantum many-body scars can be described by the coherent state with parameter β as [234]

$$|\psi_\beta\rangle = \mathrm{tr}[A_{p_1}B_{p_1}\dots A_{p_n}B_{p_n}]\,|p_1,\dots,p_n\rangle\,, \tag{109}$$

where A, B are $n\times n$ matrices with matrix elements

$$(A_p)_{ij} = \beta^p\delta_{ip}\delta_{j0} + \frac{(-1)^{j+1}\beta^p}{\sin(\pi(n-j)/n)}\delta_{n-p,j-i}, \tag{110}$$

$$(B_p)_{ij} = \beta^p\delta_{ip}\delta_{j0} + \frac{(-1)^{n-j}\beta^p}{\sin(\pi(n-j)/n)}\delta_{n-p,j-1}. \tag{111}$$

Here $0\le i,j\le n-1$ with $n\ge 2$. This representation ensures that no certain spin configurations occur over three consecutive sites in $|\psi_\beta\rangle$.

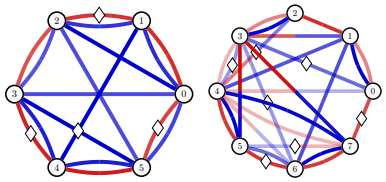

Figure 51: The associated graphs for the Onsager's scar in a system with six (left panel) and eight (right) qubits. Here we set $\beta = 1/\sqrt{2}$.

Fig. 51 displays the graph associated with the Onsager's scar in a system with six and eight spins, with $\beta = 1/\sqrt{2}$. Up to normalization, the states read [72] [73]

$$\begin{aligned}\left|\psi_\beta^{(6)}\right\rangle = &+2(|000011\rangle - |000110\rangle + |001100\rangle \\ &+ |110000\rangle - |011000\rangle - |100001\rangle) \\ &+ |011110\rangle + |001111\rangle + |100111\rangle \\ &- |101101\rangle - |011011\rangle + |110011\rangle \\ &- |110110\rangle + |111001\rangle + |111100\rangle \\ &+ 4\,|000000\rangle\,,\end{aligned} \tag{112}$$

$$\begin{aligned}\left|\psi_\beta^{(8)}\right\rangle = &8\,|00000000\rangle + 4(|00000011\rangle - |00000110\rangle \\ &+ |00001100\rangle - |00011000\rangle + |00110000\rangle \\ &- |01100000\rangle + |11000000\rangle - |10000001\rangle) \\ &+ 2(|00001111\rangle - |00011011\rangle + |00011110\rangle \\ &+ |00110011\rangle - |00110110\rangle + |00111100\rangle \\ &- |01100011\rangle + |01100110\rangle - |01101100\rangle \\ &+ |01111000\rangle + |10000111\rangle - |10001101\rangle \\ &+ |10011001\rangle - |10110001\rangle + |11000011\rangle \\ &- |11000110\rangle + |11001100\rangle - |11011000\rangle \\ &+ |11100001\rangle + |11110000\rangle) + |00111111\rangle \\ &+ |10110111\rangle - |10111101\rangle - |01101111\rangle \\ &- |10011111\rangle + |11001111\rangle - |11011011\rangle \\ &+ |11011110\rangle + |01111011\rangle - |01111110\rangle \\ &- |11100111\rangle + |11101101\rangle + |11110011\rangle \\ &- |11110110\rangle - |11111001\rangle + |11111100\rangle \\ &+ |11111111\rangle\,.\end{aligned} \tag{113}$$

Scars in the PXP Model – Another platform where quantum scars emerge is in the PXP model. This model on a chain with L sites and

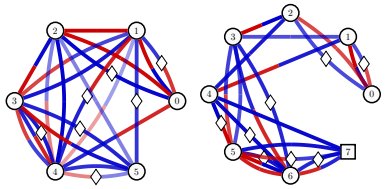

Figure 52: The graphs associated with the ground state of the PXP model with six (left panel) and eight (right) particles.

with the periodic boundary condition is [235]

$$\mathcal{H} = \sum_i P_{i-1} X_i P_{i+1} + P_L X_1 P_2 + P_{L-1} X_L P_1, \tag{114}$$

where $P = |0\rangle\langle 0|$ and $X = |0\rangle\langle 1| + |1\rangle\langle 0|$. One of the ground states of this model in the matrix product representation yields

$$|\mathrm{PXP}\rangle = \sum_{\{\sigma\}} \mathrm{tr}[B^{\sigma_1} C^{\sigma_2} \dots B^{\sigma_{L-1}} C^{\sigma_{L-1}}] \, |\sigma_1 \sigma_2 \dots \sigma_L\rangle, \tag{115}$$

where

$$B^0 = \begin{pmatrix} 1 & 0 & 0 \\ 0 & 1 & 0 \end{pmatrix}, \quad B^1 = \sqrt{2} \begin{pmatrix} 0 & 0 & 0 \\ 1 & 0 & 1 \end{pmatrix}, \tag{116}$$

$$C^0 = \begin{pmatrix} 0 & -1 \\ 1 & 0 \\ 0 & 0 \end{pmatrix}, \quad C^1 = \sqrt{2} \begin{pmatrix} 1 & 0 \\ 0 & 0 \\ -1 & 0 \end{pmatrix}. \tag{117}$$

Fig. 52 displays the graph associated with the ground state of the PXP model with six and eight particles. Up to normalization, these states read [74] [75]

$$\begin{aligned} |\mathrm{PXP6}\rangle = {} & |000000\rangle - |000010\rangle \\ & - |101000\rangle - |100000\rangle \\ & + |101010\rangle - 2\,|010100\rangle \\ & + \sqrt{2}(|100100\rangle + |010000\rangle), \end{aligned} \tag{118}$$

$$\begin{aligned} |\mathrm{PXP8}\rangle = {} & |00000000\rangle + |00001000\rangle \\ & + |10000000\rangle + |10101010\rangle \\ & - |00001010\rangle - |10000010\rangle \\ & - |10100000\rangle - |10101000\rangle \\ & - 2(|01010000\rangle + |10010100\rangle) \\ & + \sqrt{2}(|01000010\rangle - |00000100\rangle \\ & + |10010000\rangle - |01000000\rangle \\ & + |10100100\rangle + 2\,|01010100\rangle). \end{aligned} \tag{119}$$

4.6 Quantum Communication

Quantum communication refers to communication protocols that involve the transfer of quantum states. Machine learning has been previously employed for the artificial discovery of quantum communication schemes [47].

The first experimental realization of entanglement swapping was presented as a way of entangling two photons that never interacted [89]. In this section we show graphs corresponding to experiments that create entanglement between two parties (each party with single or multiple photons) without interaction between the parties. Entanglement swapping has a strong connection to other quantum communication tasks, e.g. teleportation. This opens the door to use PyTheus for discovering related quantum information protocols.

Entangling Two Photons that Never Interacted without Bell Pairs – Respecting the constraints that are placed on two particles that do not interact (presented in section 2.2) we show a graph that entangles two photons from independent sources in Fig. 53 . The corresponding setup constructed by path identity does not require the initial creation of entangled Bell pairs [76].

Multiparticle Entanglement Swapping – Performing simultaneous entanglement swapping on multiple pairs of particles is one of the key players in achieving resource-efficient quantum communication. Entanglement swapping between two qubits requires two additional particles for a Bell state measurement. Performing this swapping experiment in parallel for n qubit pairs would require $2n$ additional photons. We prompted PyTheus to find experiments that beat this naive baseline. With this, we found a three-qubit entanglement swapping experiment

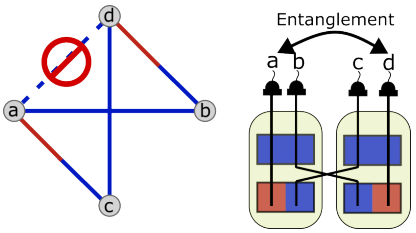

Figure 53: Entanglement between two qubits without a common source. Because the vertices a and d have no connection in the graph, each of the corresponding photons is created in one of two disjoint subsystems (green boxes).

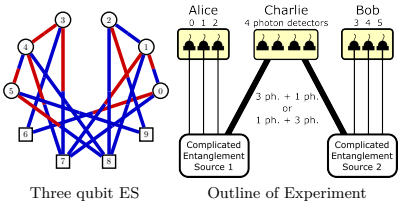

Figure 54: **Entanglement swapping of 3 Bell pairs measuring only 4 photons.** Left: abstract graph for multi-particle entanglement swapping. Right: outline of a multi-particle Entanglement swapping experiment. Alice and Bob each receive three particles from the two independent sources 1 and 2 (each a collection of SPDC crystals). When Charlie measures a coincidence in all four detectors Alice and Bob share three Bell pairs (0&3, 1&4, 2&5) without them having interacted. This is possible due to a superposition of events where Charlie either receives three photons from Alice and one photon from Bob or one photon from Alice and three photons from Bob.

(Fig. 54), which produces the state 77

$$\left|\Phi^+\right\rangle_{03} \otimes \left|\Phi^+\right\rangle_{14} \otimes \left|\Phi^+\right\rangle_{25}, \tag{120}$$

where the photons $0, 1, 2$ are separated from $3, 4, 5$. This experiment requires four additional particles instead of the six particles necessary for the parallel case described above.

Similarly, entanglement swapping between a pair of qutrits requires four ancillary particles. We found that "performing entanglement swapping for two pairs of qutrits could also beat the naive baseline by only requiring six ancillas instead of eight, in total, to produce 78

$$\left|\Phi^+\right\rangle_{02}^{3d} \otimes \left|\Phi^+\right\rangle_{13}^{3d}, \tag{121}$$

where the photons $0, 1$ are separated from $2, 3$, and $|\Phi^+\rangle^{3d}$ is the first three-dimensional Bell state.

Entanglement Swapping with Single-Photon Sources It is also possible to use single-photon sources for entanglement swapping [91, 236, 237]. In Fig. 55, we show a graph 79 for a higher-dimensional case, performing three-dimensional entanglement swapping with single photon sources. In total, six single photon sources are necessary.

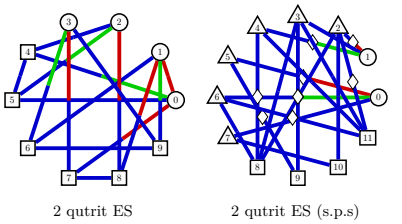

Figure 55: Graphs for entanglement swapping experiments.

4.7 Quantum Measurements

An important tool in quantum information is multi-particle measurements such as the Bell state measurement [94] or the GHZ analyzer [238]. Here we present a wider range of measurements that PyTheus has discovered. Many others, such as POVM (positive operator-valued measure) or their symmetric, informationally complete special case (SIC-POVMs) could be additional targets for future research, given their exceptional importance for quantum information tasks [239, 240] as well as their connection to exciting number theoretical questions [241].

4.7.1 Analyzers

Here, we use the word *analyzer* to refer to experimental setups that confirm a collection of photons to be in a particular state. Their formulation in terms of graphs is described in 2.3. The two-dimensional GHZ analyzer realized in Ref. [238]

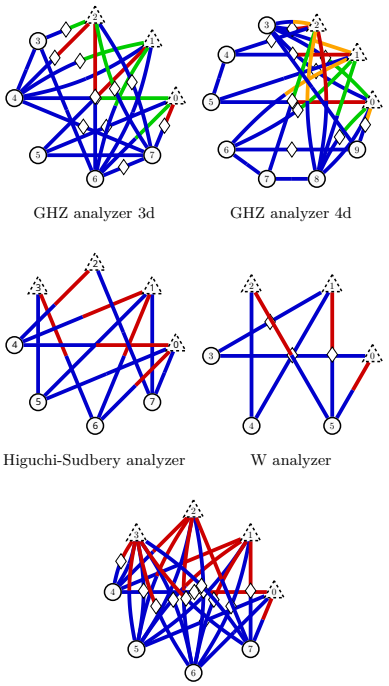

Figure 56: Graphs for analyzers. When all detectors click, the incoming photons were in the corresponding state.

can be extended towards higher dimensions, giving the 3d GHZ analyzer [80] and the 4d GHZ analyzer [81]. Further, we show analyzers for the W state [82], the Higuchi-Sudbery state (shown in Eq. (51)) [83] and the Yeo-Chua state (shown in Eq. (27)) [84] in Fig. 56.

4.7.2 Mean King's Problem

In 1987, L. Vaidman, Y. Akaronov, and D. Z. Albert [117] devised an interesting quantum communication task that can be solved only with quantum resources. Later referred to as the Mean King's Problem (MKP), it involves two parties. Alice, who sends a quantum state which she created to another party – the Mean King. The Mean King then performs a projective measurement on the state in a basis of his choice out of a collection of mutually unbiased bases (MUBs). Alice is then allowed to perform one more measurement, after which the King declares his measurement basis and Alice must correctly guess his result. Should Alice guess incorrectly even once, she will suffer a cruel fate, for the Mean King is exceptionally intolerant of poor guesses. This task has applications in quantum key distribution, wherein even the slightest discrepancy between the shared secret key of Alice and Bob implicates (in principle) the presence of an eavesdropper.

Over the years, various generalizations to the initial solution, proposed in the original paper [117], have been introduced. Here, we employ a generalization proposed by Hayashi, Horibe, and Hashimoto [242] for quantum states of dimension D which is a prime power. This solution proposes that Alice first prepares a maximally entangled, two-photon state $|\psi_o\rangle$ and sends one of her photons to the Mean King. After the King makes a projective measurement in one of the $(D+1)$ MUBs, Alice retrieves her photon and performs a measurement in the basis of states credited to Vaidman, Akaronov, and Albert (VAA states). There are D^2 VAA states in all. For $D = 2$, the first VAA state can be written as

$$|\phi_1\rangle = \frac{1}{2}(\sqrt{2}\,|00\rangle + e^{-i\frac{\pi}{4}}\,|01\rangle + e^{i\frac{\pi}{4}}\,|10\rangle) \quad (122)$$

For $D = 3$, the third VAA state can be written as

$$|\phi_3\rangle = \frac{1}{\sqrt{3}}(|00\rangle + \alpha(|02\rangle + |10\rangle + |01\rangle + |20\rangle) + \beta(|12\rangle) + \gamma(|21\rangle)) \quad (123)$$

where $\omega = e^{-i2\pi/3}$, $\alpha = (\omega^2 + 2\omega)/3$, $\beta = (\omega^2 + 2)/3$, and $\gamma = (\omega + 2)/3$,

Experimentally realizing Alice's measurement in this basis is non-trivial. Setups that recreate the two-dimensional VAA measurement using two qubits encoded in a single photon [243, 244] and that realize extensions to the Mean King's problem [245] have been proposed; but the original solution to the Mean King's Problem involves two photons, to which no experimental realization has been proposed for any prime-power D. Here we provide examples discovered by PyTheus for select prime-dimensional cases.

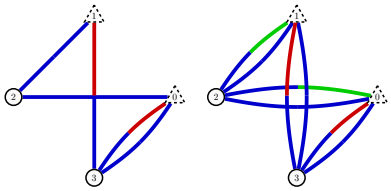

MKP (2d) MKP (3d)

Figure 57: Graphs realizing the VAA state measurement for the MKP in the 2-dimensional case and 3-dimensional case.

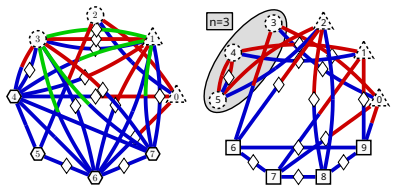

Heralded CNOT(2,3) Heralded Toffoli

Figure 58: Graphs for heralded quantum gates.

Two-dimensional Case – The left side of Fig. 57 shows the graph of Alice's measurement in the VAA basis [85]. This graph was found with PyTheus by optimizing for the VAA state projection into $|\phi_1\rangle$. Surprisingly however, during the translation of the graph to an optical setup, we found that several other VAA states can be projected with the same setup, by adding detectors at unused beam splitter ports. Several of the remaining VAA states can then be distinguished by the set of possible simultaneous two-detector click events that they each trigger. Since any result of the Mean King's measurement can be expressed in terms of a superposition of VAA states, Alice is able to guess the result by performing the measurement of her input state in the VAA basis and guessing the state that can be expressed in terms of Alice's measurement result. This procedure works regardless of the Mean King's choice of MUB in his measurement.

Three-Dimensional Case – The right-hand side of Fig. 57 shows the graph for the projection of the state into the one of the three-dimensional VAA states $|\phi_3\rangle$ [86]. As with the two-dimensional case, we add again detectors at the empty port of beam splitters and find that we can distinguish between more three of the nine states without any additional modifications. After post-selection, Alice has a guaranteed chance to correctly guess the Mean King's measurement result so long as the King does not choose the second MUB for his measurement. Were the King to pick that MUB, two of the three results of the measurement are expressed in terms of VAA states that Alice cannot distinguish, giving her a 50% chance of escaping the Mean King's cruelty.

4.8 Quantum Gates

Universal quantum gates, which rely on the interaction between two or more photons, can be realized with non-linearities induced by measurements [97]. Quantum gates based on this approach, such as a CNOT between two qubits, have been realized experimentally for almost twenty years [98]. However, since then, the attempt to experimentally discover a wide range of quantum gates has continued due to the advancement of experimental resources which can deal with higher dimensional systems.

Heralded – We call a quantum gate heralded when only ancillary particles are detected, meaning that the outgoing particles are not measured. The photons exiting such a gate can continue into further components of a longer circuit. At the end of the circuit it is necessary to confirm that two photons have exited the gate, but not which path they followed. We find that a higher dimensional version of the CNOT gate with a control qubit and a target qutrit (CNOT$(2,3)$ [87]) can also be realized with two ancilla photons. Further, we find a heralded Toffoli gate with four ancillas [88]; see Fig. 58.

Reduced Input Space – For some tasks in which quantum gates are applied, there is some prior knowledge about the input state. This knowledge can be exploited to reduce the experimental resources required to perform the transformation [105, 246]. A wide range of constraints on the input state can be encoded by our framework. Here we show examples of heralded quan-

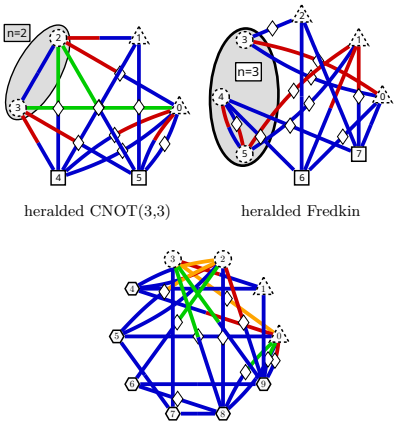

heralded CNOT(3,3) heralded Fredkin

heralded CNOT(4,4)

Figure 59: Graphs for heralded quantum gates with reduced input space.

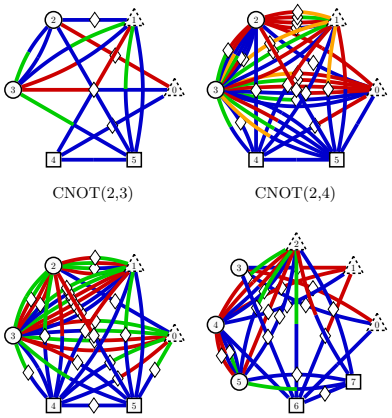

CNOT(2,3) CNOT(2,4)

CNOT(3,3) 3d Toffoli with two ancilla photons

Figure 60: Graphs for quantum gates with post-selection.

tum gates where a target qubit is prepared in the zero state before entering the gate.

PyTheus found gates CNOT$(3,3)$ [89], CNOT$(4,4)$ [90] and the Fredkin gate [91] acting on a target input photon in the computational zero state; see Fig. 59. A post-selected Fredkin gate on the full input space has been experimentally realized [106].

Post-Selected – When post-selecting a gate, all outgoing photons are detected and thus destroyed. Such a gate does not require as many resources as a heralded gate, but it imposes restrictions, such as not mixing the two output paths, on the remainder of the circuit, to ensure that the presence of a photon in each output of the gate can be ascertained. PyTheus found different post-selected high-dimensional CNOT gates, such as CNOT$(2,3)$ [92], CNOT$(2,4)$ [93], CNOT$(3,3)$ [94] and the Toffoli gate on a qutrit [95]; see Fig. 60.

4.8.1 Single Photon Sources for Quantum Gates

Experiments exploiting single-photon sources as an additional resource for the construction of quantum gates have been previously demonstrated [112]. Fig. 61 displays graphs for a heralded CNOT$(2,2)$ with two additional input photons [96], a heralded CNOT$(2,3)$ with three additional input photons [97], and a post-selected CNOT$(2,3)$ with two additional input photons [98].

4.9 Combinatorial Measures

In this section, we demonstrate how PyTheus can discover exceptional structures without computing the quantum state. This ability might be useful for finding experimental configurations with particular symmetries or properties that are interesting, independent of the resulting quantum state. Such metrics can also be combined with other objectives mentioned in the previous sections.

4.9.1 Assembly Index

As an example for structural property discovery, we consider the *assembly index*, which has been invented in chemistry for the search of extraterrestrial life [247, 248]. Specifically, the assembly index counts the complexity of building up a combinatorial structure, for instance, molecules or — in our case — graphs. It counts the number of in-

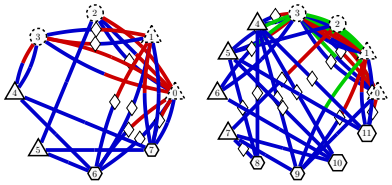

heralded CNOT(2,2) s.p.s heralded CNOT(2,3) s.p.s

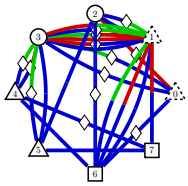

post-selected CNOT(2,3) s.p.s

Figure 61: Graphs for quantum gates with single-photon sources as an additional resource.

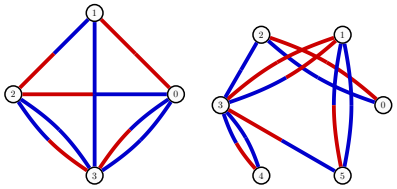

4 qubits, 8 edges, assembly index 8 6 qubits, 10 edges, assembly index 10

Figure 62: Graphs for assembly index.

dependent processes that are necessary to create a structure. The hypothesis is that a structure with a large assembly index cannot be formed by natural processes and would require complex (living) systems for its generation. Strong indications in favor of this hypothesis have been found in the study of millions of molecules on earth [248].

Our goal here is to discover graphs with very high assembly indices. The assembly index is a discrete structural metric that cannot be optimized directly using gradients. However, we can use the weights of edges to transform the discrete metric into a continuously differentiable metric. A general procedure is to compute the average combinatorial value of the weighted graph from sampled discrete graphs. Here, the weights $|\omega_i|^2$ are used as the probability for sampling discrete graphs. While this procedure is differential, it is computationally expensive as many sampled graphs need to be evaluated to obtain an average assembly index of the whole graph.

Alternatively, here we restrict ourselves to graphs with exactly eight edges (with 4 99 and 6 100 vertices). Here, the eight highest-weighted edges are used to generate the graph, and in addition, weights are used to change the order of edges. The graphs in Fig. 62 present graphs with very high assembly indices with 4 vertices and 8 edges as well as 6 vertices and 10 edges.

5 Outlook

This article uses a list of examples to showcase the broad range of possibilities of digital discovery in quantum optics. The goal to design one hundred novel and intriguing experiments has led us to collect a diverse set of tasks for which experimental setups could be designed. To make the discoveries possible, we expanded the theoretical framework underlying the algorithm and produced faster, more versatile open-source software. We hope that this work can be an inspiration for experimental physicists in two ways: (1) to explore some of the experiments as they are proposed in this article (2) to see that PyTheus can be used to design experiments for a wide range of targets and for individually tailored specifications of experimental restrictions and resources. To explore particular examples that have not been covered in this article, the open-source library PyTheus can be used. Many more avenues leave room for significant further exploration, particularly within the optimization for targets other than fidelity, as well as more specific experimental constraints. For this, the PyTheus framework can readily be expanded in the future.

A number of extensions that would be interesting include the discovery of experiments that maximize success probability in terms of heralding efficiency or Bell state measurement efficiency, especially as experimentally available technologies became increasingly powerful [249]. The po-

tential of PyTheus on suggesting experimental setups can pave the way to find experiments to simulate quantum states, which are nowadays merely realizable in extreme (thermodynamics) conditions, such as high pressure and low temperature [250]. An exciting extension would be the analysation whether we can extend state generation to encoding the dymanics of a quantum state into the weights of the graphs. Along with this line of research, it is theoretically tantalizing to explore the putative correlation between the complexity of time-evolved states [251] and the complexity of associated graphs as outputs of PyTheus.

As a final thought, we want to view our results through an additional lens. We have created a dataset of 100 hand-selected quantum experiments that are some aspects exceptional (which PyTheus has discovered). This dataset might be large enough for highly efficient artificial intelligence algorithms to bootstrap an intuition of what properties make an experiment interesting, and allow them to produce proposals for new, hopefully equally interesting quantum experiments. It would sure be exciting to investigate the physical properties of the proposals that the machine believes are *interesting*. In the best case, it could act as an inspiration for new ideas for the human scientist [252, 253].

6 Acknowledgment

The authors thank Jian-Wei Wang and Jake Bulmer for their useful comments. The authors thank Matthias Bär for his support in software development and Jhon Alejandro Montañez for help in an early version of the software. S.S. thanks the Galileo Galilei Institute for Theoretical Physics for hospitality during the completion of this work. T.J. and E.K. acknowledge the support of the Canada Research Chairs (CRC) and Max Planck-University of Ottawa Centre for Extreme and Quantum Photonics. N.T. is a recipient of an Australian Research Council Discovery Early Career Researcher Award (DE220101082). This work was partially supported by the Australian Research Council Centre of Excellence for Quantum Computation and Communication Technology (Grant No. CE170100012).

References

[1] Jian-Wei Pan, Zeng-Bing Chen, Chao-Yang Lu, Harald Weinfurter, Anton Zeilinger, and Marek Żukowski. Multiphoton entanglement and interferometry. *Rev. Mod. Phys.*, 84, May 2012. DOI: 10.1103/RevModPhys.84.777.

[2] Sheng-Kai Liao, Wen-Qi Cai, Wei-Yue Liu, Liang Zhang, Yang Li, Ji-Gang Ren, Juan Yin, Qi Shen, Yuan Cao, Zheng-Ping Li, et al. Satellite-to-ground quantum key distribution. *Nature*, 549(7670), 2017. DOI: 10.1038/nature23655.

[3] Sheng-Kai Liao, Wen-Qi Cai, Johannes Handsteiner, Bo Liu, Juan Yin, Liang Zhang, Dominik Rauch, Matthias Fink, Ji-Gang Ren, Wei-Yue Liu, et al. Satellite-relayed intercontinental quantum network. *Phys. Rev. Lett.*, 120, Jan 2018. DOI: 10.1103/PhysRevLett.120.030501.

[4] Bas Hensen, Hannes Bernien, Anaïs E Dréau, Andreas Reiserer, Norbert Kalb, Machiel S Blok, Just Ruitenberg, Raymond FL Vermeulen, Raymond N Schouten, Carlos Abellán, et al. Loophole-free Bell inequality violation using electron spins separated by 1.3 kilometres. *Nature*, 526(7575), 2015. DOI: 10.1038/nature15759.

[5] Lynden K Shalm, Evan Meyer-Scott, Bradley G Christensen, Peter Bierhorst, Michael A Wayne, Martin J Stevens, Thomas Gerrits, Scott Glancy, Deny R Hamel, Michael S Allman, et al. Strong loophole-free test of local realism. *Phys. Rev. Lett.*, 115, Dec 2015. DOI: 10.1103/PhysRevLett.115.250402.

[6] Marissa Giustina, Marijn AM Versteegh, Sören Wengerowsky, Johannes Handsteiner, Armin Hochrainer, Kevin Phelan, Fabian Steinlechner, Johannes Kofler, Jan-Åke Larsson, Carlos Abellán, et al. Significant-loophole-free test of Bell's theorem with entangled photons. *Phys. Rev. Lett.*, 115, Dec 2015. DOI: 10.1103/PhysRevLett.115.250401.

[7] Sara Bartolucci, Patrick Birchall, Hector Bombin, Hugo Cable, Chris Dawson, Mercedes Gimeno-Segovia, Eric Johnston, Konrad Kieling, Naomi Nickerson, Mihir Pant, et al. Fusion-based quan-

tum computation. *arXiv*, 2021. DOI: 10.48550/arXiv.2101.09310.

[8] Emanuele Polino, Mauro Valeri, Nicolò Spagnolo, and Fabio Sciarrino. Photonic quantum metrology. *AVS Quantum Science*, 2(2), 2020. DOI: 10.1116/5.0007577.

[9] Christoph Schaeff, Robert Polster, Marcus Huber, Sven Ramelow, and Anton Zeilinger. Experimental access to higher-dimensional entangled quantum systems using integrated optics. *Optica*, 2(6), 2015. DOI: 10.1364/OPTICA.2.000523.

[10] Jianwei Wang, Stefano Paesani, Yunhong Ding, Raffaele Santagati, Paul Skrzypczyk, Alexia Salavrakos, Jordi Tura, Remigiusz Augusiak, Laura Mančinska, Davide Bacco, et al. Multidimensional quantum entanglement with large-scale integrated optics. *Science*, 360(6386), 2018. DOI: 10.1126/science.aar7053.

[11] Jianwei Wang, Fabio Sciarrino, Anthony Laing, and Mark G Thompson. Integrated photonic quantum technologies. *Nature Photonics*, 14(5), 2020. DOI: 10.1038/s41566-019-0532-1.

[12] Emanuele Pelucchi, Giorgos Fagas, Igor Aharonovich, Dirk Englund, Eden Figueroa, Qihuang Gong, Hübel Hannes, Jin Liu, Chao-Yang Lu, Nobuyuki Matsuda, et al. The potential and global outlook of integrated photonics for quantum technologies. *Nature Reviews Physics*, 4(3), 2022. DOI: 10.1038/s42254-021-00398-z.

[13] Hui Wang, Yu-Ming He, T-H Chung, Hai Hu, Ying Yu, Si Chen, Xing Ding, M-C Chen, Jian Qin, Xiaoxia Yang, et al. Towards optimal single-photon sources from polarized microcavities. *Nature Photonics*, 13(11), 2019. DOI: 10.1038/s41566-019-0494-3.

[14] Yasuhiko Arakawa and Mark J Holmes. Progress in quantum-dot single photon sources for quantum information technologies: A broad spectrum overview. *Applied Physics Reviews*, 7(2), 2020. DOI: 10.1063/5.0010193.

[15] Natasha Tomm, Alisa Javadi, Nadia Olympia Antoniadis, Daniel Najer, Matthias Christian Löbl, Alexander Rolf Korsch, Rüdiger Schott, Sascha René Valentin, Andreas Dirk Wieck, Arne Ludwig, et al. A bright and fast source of coherent single photons. *Nature Nanotechnology*, 16(4), 2021. DOI: 10.1038/s41565-020-00831-x.

[16] Ravitej Uppu, Leonardo Midolo, Xiaoyan Zhou, Jacques Carolan, and Peter Lodahl. Quantum-dot-based deterministic photon–emitter interfaces for scalable photonic quantum technology. *Nature nanotechnology*, 16(12), 2021. DOI: 10.1038/s41565-021-00965-6.

[17] Tomás Santiago-Cruz, Sylvain D Gennaro, Oleg Mitrofanov, Sadhvikas Addamane, John Reno, Igal Brener, and Maria V Chekhova. Resonant metasurfaces for generating complex quantum states. *Science*, 377(6609), 2022. DOI: 10.1126/science.abq8684.

[18] Matthew D Eisaman, Jingyun Fan, Alan Migdall, and Sergey V Polyakov. Invited review article: Single-photon sources and detectors. *Review of scientific instruments*, 82(7), 2011. DOI: 10.1063/1.3610677.

[19] Sergei Slussarenko and Geoff J Pryde. Photonic quantum information processing: A concise review. *Applied Physics Reviews*, 6 (4), 2019. DOI: 10.1063/1.5115814.

[20] Frédéric Bouchard, Alicia Sit, Yingwen Zhang, Robert Fickler, Filippo M Miatto, Yuan Yao, Fabio Sciarrino, and Ebrahim Karimi. Two-photon interference: the hong–ou–mandel effect. *Reports on Progress in Physics*, 84(1), 2020. DOI: 10.1088/1361-6633/abcd7a.

[21] Adrian J. Menssen, Alex E. Jones, Benjamin J. Metcalf, Malte C. Tichy, Stefanie Barz, W. Steven Kolthammer, and Ian A. Walmsley. Distinguishability and many-particle interference. *Phys. Rev. Lett.*, 118, Apr 2017. DOI: 10.1103/PhysRevLett.118.153603.

[22] Lan-Tian Feng, Ming Zhang, Di Liu, Yu-Jie Cheng, Guo-Ping Guo, Dao-Xin Dai, Guang-Can Guo, Mario Krenn, and Xi-Feng Ren. On-chip quantum interference between the origins of a multi-photon state. *Optica*, 10(1), 2023. DOI: 10.1364/OPTICA.474750.

[23] Kaiyi Qian, Kai Wang, Leizhen Chen, Zhaohua Hou, Mario Krenn, Shining Zhu,

and Xiao-song Ma. Multiphoton non-local quantum interference controlled by an undetected photon. *Nature Communications*, 14(1), 2023. DOI: 10.1038/s41467-023-37228-y.

[24] Mario Krenn, Manuel Erhard, and Anton Zeilinger. Computer-inspired quantum experiments. *Nature Reviews Physics*, 2(11), 2020. DOI: 10.1038/s42254-020-0230-4.

[25] Mario Krenn, Mehul Malik, Robert Fickler, Radek Lapkiewicz, and Anton Zeilinger. Automated search for new quantum experiments. *Phys. Rev. Lett.*, 116, Mar 2016. DOI: 10.1103/PhysRevLett.116.090405.

[26] Amin Babazadeh, Manuel Erhard, Feiran Wang, Mehul Malik, Rahman Nouroozi, Mario Krenn, and Anton Zeilinger. High-dimensional single-photon quantum gates: Concepts and experiments. *Phys. Rev. Lett.*, 119, Nov 2017. DOI: 10.1103/PhysRevLett.119.180510.

[27] Mehul Malik, Manuel Erhard, Marcus Huber, Mario Krenn, Robert Fickler, and Anton Zeilinger. Multi-photon entanglement in high dimensions. *Nature Photonics*, 10, 2016. DOI: 10.1038/nphoton.2016.12.

[28] Manuel Erhard, Mehul Malik, Mario Krenn, and Anton Zeilinger. Experimental Greenberger–Horne–Zeilinger entanglement beyond qubits. *Nature Photonics*, 12 (12), 2018. DOI: 10.1038/s41566-018-0257-6.

[29] Jaroslav Kysela, Manuel Erhard, Armin Hochrainer, Mario Krenn, and Anton Zeilinger. Path identity as a source of high-dimensional entanglement. *Proceedings of the National Academy of Sciences*, 117(42), 2020. DOI: 10.1073/pnas.2011405117.

[30] Mario Krenn, Armin Hochrainer, Mayukh Lahiri, and Anton Zeilinger. Entanglement by path identity. *Phys. Rev. Lett.*, 118, Feb 2017. DOI: 10.1103/PhysRevLett.118.080401.

[31] Xiaoqin Gao, Manuel Erhard, Anton Zeilinger, and Mario Krenn. Computer-inspired concept for high-dimensional multipartite quantum gates. *Phys. Rev. Lett.*, 125, Jul 2020. DOI: 10.1103/PhysRevLett.125.050501.

[32] Mario Krenn, Jakob S. Kottmann, Nora Tischler, and Alán Aspuru-Guzik. Conceptual understanding through efficient automated design of quantum optical experiments. *Phys. Rev. X*, 11, Aug 2021. DOI: 10.1103/PhysRevX.11.031044.

[33] Mario Krenn, Xuemei Gu, and Anton Zeilinger. Quantum experiments and graphs: Multiparty states as coherent superpositions of perfect matchings. *Phys. Rev. Lett.*, 119, Dec 2017. DOI: 10.1103/PhysRevLett.119.240403.

[34] Xuemei Gu, Manuel Erhard, Anton Zeilinger, and Mario Krenn. Quantum experiments and graphs ii: Quantum interference, computation, and state generation. *Proceedings of the National Academy of Sciences*, 116, 2019. DOI: 10.1073/pnas.1815884116.

[35] Xuemei Gu, Lijun Chen, Anton Zeilinger, and Mario Krenn. Quantum experiments and graphs. iii. high-dimensional and multiparticle entanglement. *Phys. Rev. A*, 99, Mar 2019. DOI: 10.1103/PhysRevA.99.032338.

[36] Robert Raussendorf and Hans J. Briegel. A one-way quantum computer. *Phys. Rev. Lett.*, 86, May 2001. DOI: 10.1103/PhysRevLett.86.5188.

[37] Robert Raussendorf, Daniel E. Browne, and Hans J. Briegel. Measurement-based quantum computation on cluster states. *Phys. Rev. A*, 68, Aug 2003. DOI: 10.1103/PhysRevA.68.022312.

[38] Hans J Briegel, David E Browne, Wolfgang Dür, Robert Raussendorf, and Maarten Van den Nest. Measurement-based quantum computation. *Nature Physics*, 5(1), 2009. DOI: 10.1038/nphys1157.

[39] Sören Arlt, Carlos Ruiz-Gonzalez, and Mario Krenn. Digital discovery of a scientific concept at the core of experimental quantum optics. *arXiv*, 2022. DOI: 10.48550/arXiv.2210.09981.

[40] Mario Krenn, Jonas Landgraf, Thomas Foesel, and Florian Marquardt. Artificial intelligence and machine learning for quantum technologies. *Physical Review A*, 107(1), 2023. DOI: 10.1103/PhysRevA.107.010101.

[41] PA Knott. A search algorithm for quantum state engineering and metrology. *New*

Journal of Physics, 18(7), 2016. DOI: 10.1088/1367-2630/18/7/073033.

[42] L O'Driscoll, Rosanna Nichols, and Paul A Knott. A hybrid machine learning algorithm for designing quantum experiments. *Quantum Machine Intelligence*, 1(1), 2019. DOI: 10.1007/s42484-019-00003-8.

[43] Rosanna Nichols, Lana Mineh, Jesús Rubio, Jonathan CF Matthews, and Paul A Knott. Designing quantum experiments with a genetic algorithm. *Quantum Science and Technology*, 4(4), 2019. DOI: 10.1088/2058-9565/ab4d89.

[44] Xiang Zhan, Kunkun Wang, Lei Xiao, Zhihao Bian, Yongsheng Zhang, Barry C Sanders, Chengjie Zhang, and Peng Xue. Experimental quantum cloning in a pseudo-unitary system. *Physical Review A*, 101(1), 2020. DOI: 10.1103/PhysRevA.101.010302.

[45] Alexey A Melnikov, Hendrik Poulsen Nautrup, Mario Krenn, Vedran Dunjko, Markus Tiersch, Anton Zeilinger, and Hans J Briegel. Active learning machine learns to create new quantum experiments. *Proceedings of the National Academy of Sciences*, 115(6), 2018. DOI: 10.1073/pnas.1714936115.

[46] Alexey A. Melnikov, Pavel Sekatski, and Nicolas Sangouard. Setting up experimental Bell tests with reinforcement learning. *Phys. Rev. Lett.*, 125, Oct 2020. DOI: 10.1103/PhysRevLett.125.160401.

[47] Julius Wallnöfer, Alexey A. Melnikov, Wolfgang Dür, and Hans J. Briegel. Machine learning for long-distance quantum communication. *PRX Quantum*, 1, Sep 2020. DOI: 10.1103/PRXQuantum.1.010301.

[48] X. Valcarce, P. Sekatski, E. Gouzien, A. Melnikov, and N. Sangouard. Automated design of quantum-optical experiments for device-independent quantum key distribution. *Phys. Rev. A*, 107, Jun 2023. DOI: 10.1103/PhysRevA.107.062607.

[49] Thomas Adler, Manuel Erhard, Mario Krenn, Johannes Brandstetter, Johannes Kofler, and Sepp Hochreiter. Quantum optical experiments modeled by long short-term memory. In *Photonics*, volume 8. Multidisciplinary Digital Publishing Institute, 2021. DOI: 10.3390/photonics8120535.

[50] Daniel Flam-Shepherd, Tony C Wu, Xuemei Gu, Alba Cervera-Lierta, Mario Krenn, and Alan Aspuru-Guzik. Learning interpretable representations of entanglement in quantum optics experiments using deep generative models. *Nature Machine Intelligence*, 4(6), 2022. DOI: 10.1038/s42256-022-00493-5.

[51] Alba Cervera-Lierta, Mario Krenn, and Alán Aspuru-Guzik. Design of quantum optical experiments with logic artificial intelligence. *Quantum*, 6, 2022. DOI: 10.22331/q-2022-10-13-836.

[52] Juan Miguel Arrazola, Thomas R Bromley, Josh Izaac, Casey R Myers, Kamil Brádler, and Nathan Killoran. Machine learning method for state preparation and gate synthesis on photonic quantum computers. *Quantum Science and Technology*, 4 (2), 2019. DOI: 10.1088/2058-9565/aaf59e.

[53] Nathan Killoran, Josh Izaac, Nicolás Quesada, Ville Bergholm, Matthew Amy, and Christian Weedbrook. Strawberry Fields: A Software Platform for Photonic Quantum Computing. *Quantum*, 3, Mar 2019. ISSN 2521-327X. DOI: 10.22331/q-2019-03-11-129.

[54] Nadia Belabas, Boris Bourdoncle, Pierre-Emmanuel Emeriau, Andreas Fyrillas, Grégoire de Gliniasty, Nicolas Heurtel, Raphaël Le Bihan, Sébastien Malherbe, Rawad Mezher, Shane Mansfield, Luka Music, Marceau Paillhas, Jean Senellart, Pascale Senellart, Mario Valdiva, and Benoît Valiron. Perceval: an open source framework for programming photonic quantum computers, 2022. URL `https://github.com/Quandela/Perceval`.

[55] Budapest Quantum Computing Group. Piquasso: a python library for designing and simulating photonic quantum computers, 2022. URL `https://github.com/Budapest-Quantum-Computing-Group/piquasso`.

[56] Brajesh Gupt, Josh Izaac, and Nicolás Quesada. The walrus: a library for the calculation of hafnians, hermite polynomials and gaussian boson sampling. *Journal of Open Source Software*, 4(44), 2019. DOI: 10.21105/joss.01705.

[57] Jakob S Kottmann, Mario Krenn, Thi Ha

Kyaw, Sumner Alperin-Lea, and Alán Aspuru-Guzik. Quantum computer-aided design of quantum optics hardware. *Quantum Science and Technology*, 6(3), 2021. DOI: 10.1088/2058-9565/abfc94.

[58] Jueming Bao, Zhaorong Fu, Tanumoy Pramanik, Jun Mao, Yulin Chi, Yingkang Cao, Chonghao Zhai, Yifei Mao, Tianxiang Dai, Xiaojiong Chen, et al. Very-large-scale integrated quantum graph photonics. *Nature Photonics*, 17, 2023. DOI: 10.1038/s41566-023-01187-z.

[59] Paul G. Kwiat, Klaus Mattle, Harald Weinfurter, Anton Zeilinger, Alexander V. Sergienko, and Yanhua Shih. New high-intensity source of polarization-entangled photon pairs. *Phys. Rev. Lett.*, 75, Dec 1995. DOI: 10.1103/PhysRevLett.75.4337.

[60] Liangliang Lu, Lijun Xia, Zhiyu Chen, Leizhen Chen, Tonghua Yu, Tao Tao, Wenchao Ma, Ying Pan, Xinlun Cai, Yanqing Lu, et al. Three-dimensional entanglement on a silicon chip. *npj Quantum Information*, 6(1), 2020. DOI: 10.1038/s41534-020-0260-x.

[61] Halina Rubinsztein-Dunlop, Andrew Forbes, Michael V Berry, Mark R Dennis, David L Andrews, Masud Mansuripur, Cornelia Denz, Christina Alpmann, Peter Banzer, Thomas Bauer, et al. Roadmap on structured light. *Journal of Optics*, 19(1), 2016. DOI: 10.1088/2040-8978/19/1/013001.

[62] Miles J Padgett. Orbital angular momentum 25 years on. *Optics express*, 25(10), 2017. DOI: 10.1364/OE.25.011265.

[63] Frédéric Bouchard, Robert Fickler, Robert W Boyd, and Ebrahim Karimi. High-dimensional quantum cloning and applications to quantum hacking. *Science Advances*, 3(2), 2017. DOI: 10.1126/sciadv.1601915.

[64] Jessica Bavaresco, Natalia Herrera Valencia, Claude Klöckl, Matej Pivoluska, Paul Erker, Nicolai Friis, Mehul Malik, and Marcus Huber. Measurements in two bases are sufficient for certifying high-dimensional entanglement. *Nature Physics*, 14(10), 2018. DOI: 10.1038/s41567-018-0203-z.

[65] J. D. Franson. Bell inequality for position and time. *Phys. Rev. Lett.*, 62, May 1989. DOI: 10.1103/PhysRevLett.62.2205.

[66] L. Olislager, J. Cussey, A. T. Nguyen, P. Emplit, S. Massar, J.-M. Merolla, and K. Phan Huy. Frequency-bin entangled photons. *Phys. Rev. A*, 82, Jul 2010. DOI: 10.1103/PhysRevA.82.013804.

[67] Robert W Boyd. *Nonlinear optics, Fourth Edition*. Academic press, 2020. DOI: 10.1016/C2015-0-05510-1.

[68] Regina Kruse, Craig S. Hamilton, Linda Sansoni, Sonja Barkhofen, Christine Silberhorn, and Igor Jex. Detailed study of gaussian boson sampling. *Phys. Rev. A*, 100, Sep 2019. DOI: 10.1103/PhysRevA.100.032326.

[69] Armin Hochrainer, Mayukh Lahiri, Manuel Erhard, Mario Krenn, and Anton Zeilinger. Quantum indistinguishability by path identity and with undetected photons. *Rev. Mod. Phys.*, 94, Jun 2022. DOI: 10.1103/RevModPhys.94.025007.

[70] Xi-Lin Wang, Luo-Kan Chen, W. Li, H.-L. Huang, C. Liu, C. Chen, Y.-H. Luo, Z.-E. Su, D. Wu, Z.-D. Li, H. Lu, Y. Hu, X. Jiang, C.-Z. Peng, L. Li, N.-L. Liu, Yu-Ao Chen, Chao-Yang Lu, and Jian-Wei Pan. Experimental ten-photon entanglement. *Phys. Rev. Lett.*, 117, Nov 2016. DOI: 10.1103/PhysRevLett.117.210502.

[71] Luo-Kan Chen, Zheng-Da Li, Xing-Can Yao, Miao Huang, Wei Li, He Lu, Xiao Yuan, Yan-Bao Zhang, Xiao Jiang, Cheng-Zhi Peng, et al. Observation of ten-photon entanglement using thin bib 3 o 6 crystals. *Optica*, 4(1), 2017. DOI: 10.1364/OPTICA.4.000077.

[72] Paul G. Kwiat, Edo Waks, Andrew G. White, Ian Appelbaum, and Philippe H. Eberhard. Ultrabright source of polarization-entangled photons. *Phys. Rev. A*, 60, Aug 1999. DOI: 10.1103/PhysRevA.60.R773.

[73] John Calsamiglia. Generalized measurements by linear elements. *Phys. Rev. A*, 65, Feb 2002. DOI: 10.1103/PhysRevA.65.030301.

[74] Stefano Paesani, Jacob F. F. Bulmer, Alex E. Jones, Raffaele Santagati, and Anthony Laing. Scheme for universal high-dimensional quantum computa-

tion with linear optics. *Phys. Rev. Lett.*, 126, Jun 2021. DOI: 10.1103/PhysRevLett.126.230504.

[75] Seungbeom Chin, Yong-Su Kim, and Sangmin Lee. Graph picture of linear quantum networks and entanglement. *Quantum*, 5, 2021. DOI: 10.22331/q-2021-12-23-611.

[76] AV Belinskii and DN Klyshko. Two-photon optics: diffraction, holography, and transformation of two-dimensional signals. *Soviet Journal of Experimental and Theoretical Physics*, 78(3), 1994. URL `http://jetp.ras.ru/cgi-bin/dn/e_078_03_0259.pdf`.

[77] M. F. Z. Arruda, W. C. Soares, S. P. Walborn, D. S. Tasca, A. Kanaan, R. Medeiros de Araújo, and P. H. Souto Ribeiro. Klyshko's advanced-wave picture in stimulated parametric down-conversion with a spatially structured pump beam. *Phys. Rev. A*, 98, Aug 2018. DOI: 10.1103/PhysRevA.98.023850.

[78] Evan Meyer-Scott, Christine Silberhorn, and Alan Migdall. Single-photon sources: Approaching the ideal through multiplexing. *Review of Scientific Instruments*, 91 (4), 2020. DOI: 10.1063/5.0003320.

[79] Barry C. Sanders. Quantum dynamics of the nonlinear rotator and the effects of continual spin measurement. *Phys. Rev. A*, 40, Sep 1989. DOI: 10.1103/PhysRevA.40.2417.

[80] Hwang Lee, Pieter Kok, and Jonathan P Dowling. A quantum rosetta stone for interferometry. *Journal of Modern Optics*, 49(14-15), 2002. DOI: 10.1080/0950034021000011536.

[81] Vittorio Giovannetti, Seth Lloyd, and Lorenzo Maccone. Advances in quantum metrology. *Nature photonics*, 5(4), 2011. DOI: 10.1038/nphoton.2011.35.

[82] Lu Zhang and Kam Wai Clifford Chan. Scalable generation of multi-mode noon states for quantum multiple-phase estimation. *Scientific reports*, 8(1), 2018. DOI: 10.1038/s41598-018-29828-2.

[83] Seongjin Hong, Yong-Su Kim, Young-Wook Cho, Seung-Woo Lee, Hojoong Jung, Sung Moon, Sang-Wook Han, Hyang-Tag Lim, et al. Quantum enhanced multiple-phase estimation with multi-mode n00n states. *Nature Communications*, 12(1), 2021. DOI: 10.1038/s41467-021-25451-4.

[84] A. V. Burlakov, M. V. Chekhova, O. A. Karabutova, D. N. Klyshko, and S. P. Kulik. Polarization state of a biphoton: Quantum ternary logic. *Phys. Rev. A*, 60, Dec 1999. DOI: 10.1103/PhysRevA.60.R4209.

[85] A. V. Burlakov, M. V. Chekhova, O. A. Karabutova, and S. P. Kulik. Collinear two-photon state with spectral properties of type-i and polarization properties of type-ii spontaneous parametric down-conversion: Preparation and testing. *Phys. Rev. A*, 64, Sep 2001. DOI: 10.1103/PhysRevA.64.041803.

[86] Itai Afek, Oron Ambar, and Yaron Silberberg. High-noon states by mixing quantum and classical light. *Science*, 328(5980), 2010. DOI: 10.1126/science.1188172].

[87] C. K. Hong, Z. Y. Ou, and L. Mandel. Measurement of subpicosecond time intervals between two photons by interference. *Phys. Rev. Lett.*, 59, Nov 1987. DOI: 10.1103/PhysRevLett.59.2044.

[88] M. Żukowski, A. Zeilinger, M. A. Horne, and A. K. Ekert. "event-ready-detectors" bell experiment via entanglement swapping. *Phys. Rev. Lett.*, 71, Dec 1993. DOI: 10.1103/PhysRevLett.71.4287.

[89] Jian-Wei Pan, Dik Bouwmeester, Harald Weinfurter, and Anton Zeilinger. Experimental entanglement swapping: Entangling photons that never interacted. *Phys. Rev. Lett.*, 80, May 1998. DOI: 10.1103/PhysRevLett.80.3891.

[90] Nicolas Sangouard, Christoph Simon, Hugues de Riedmatten, and Nicolas Gisin. Quantum repeaters based on atomic ensembles and linear optics. *Rev. Mod. Phys.*, 83, Mar 2011. DOI: 10.1103/RevModPhys.83.33.

[91] F. Basso Basset, M. B. Rota, C. Schimpf, D. Tedeschi, K. D. Zeuner, S. F. Covre da Silva, M. Reindl, V. Zwiller, K. D. Jöns, A. Rastelli, and R. Trotta. Entanglement swapping with photons generated on demand by a quantum dot. *Phys. Rev. Lett.*, 123, Oct 2019. DOI: 10.1103/PhysRevLett.123.160501.

[92] Daniel Llewellyn, Yunhong Ding, Imad I Faruque, Stefano Paesani, Davide Bacco,

Raffaele Santagati, Yan-Jun Qian, Yan Li, Yun-Feng Xiao, Marcus Huber, et al. Chip-to-chip quantum teleportation and multi-photon entanglement in silicon. *Nature Physics*, 16(2), 2020. DOI: 10.1038/s41567-019-0727-x.

[93] Farid Samara, Nicolas Maring, Anthony Martin, Arslan S Raja, Tobias J Kippenberg, Hugo Zbinden, and Rob Thew. Entanglement swapping between independent and asynchronous integrated photon-pair sources. *Quantum Science and Technology*, 6(4), 2021. DOI: 10.1088/2058-9565/abf599.

[94] Harald Weinfurter. Experimental Bell-state analysis. *EPL (Europhysics Letters)*, 25(8), 1994. DOI: 10.1209/0295-5075/25/8/001.

[95] Markus Michler, Klaus Mattle, Harald Weinfurter, and Anton Zeilinger. Interferometric Bell-state analysis. *Phys. Rev. A*, 53, Mar 1996. DOI: 10.1103/PhysRevA.53.R1209.

[96] Michael A Nielsen and Isaac L Chuang. *Quantum Computation and Quantum Information: 10th Anniversary Edition*. Cambridge University Press; 10th Anniversary edition (9 Dec. 2010), 2010. DOI: 10.1017/CBO9780511976667.

[97] Emanuel Knill, Raymond Laflamme, and Gerald J Milburn. A scheme for efficient quantum computation with linear optics. *nature*, 409(6816), 2001. DOI: 10.1038/35051009.

[98] Sara Gasparoni, Jian-Wei Pan, Philip Walther, Terry Rudolph, and Anton Zeilinger. Realization of a photonic controlled-not gate sufficient for quantum computation. *Phys. Rev. Lett.*, 93, Jul 2004. DOI: 10.1103/PhysRevLett.93.020504.

[99] Pieter Kok, W. J. Munro, Kae Nemoto, T. C. Ralph, Jonathan P. Dowling, and G. J. Milburn. Linear optical quantum computing with photonic qubits. *Rev. Mod. Phys.*, 79, Jan 2007. DOI: 10.1103/RevModPhys.79.135.

[100] Yuan Li, Lingxiao Wan, Hui Zhang, Huihui Zhu, Yuzhi Shi, Lip Ket Chin, Xiaoqi Zhou, Leong Chuan Kwek, and Ai Qun Liu. Quantum fredkin and toffoli gates on a versatile programmable silicon photonic chip. *npj Quantum Information*, 8(1), September 2022. DOI: 10.1038/s41534-022-00627-y.

[101] E. Knill. Quantum gates using linear optics and postselection. *Physical Review A*, 66(5), November 2002. DOI: 10.1103/physreva.66.052306.

[102] T. C. Ralph, N. K. Langford, T. B. Bell, and A. G. White. Linear optical controlled-not gate in the coincidence basis. *Phys. Rev. A*, 65, Jun 2002. DOI: 10.1103/PhysRevA.65.062324.

[103] J. L. O'Brien, G. J. Pryde, A. G. White, T. C. Ralph, and D. Branning. Demonstration of an all-optical quantum controlled-NOT gate. *Nature*, 426, 2003. DOI: 10.1038/nature02054.

[104] N. K. Langford, T. J. Weinhold, R. Prevedel, K. J. Resch, A. Gilchrist, J. L. O'Brien, G. J. Pryde, and A. G. White. Demonstration of a simple entangling optical gate and its use in Bell-state analysis. *Phys. Rev. Lett.*, 95, Nov 2005. DOI: 10.1103/PhysRevLett.95.210504.

[105] Farzad Ghafari, Nora Tischler, Jayne Thompson, Mile Gu, Lynden K. Shalm, Varun B. Verma, Sae Woo Nam, Raj B. Patel, Howard M. Wiseman, and Geoff J. Pryde. Dimensional quantum memory advantage in the simulation of stochastic processes. *Phys. Rev. X*, 9, Oct 2019. DOI: 10.1103/PhysRevX.9.041013.

[106] Raj B Patel, Joseph Ho, Franck Ferreyrol, Timothy C Ralph, and Geoff J Pryde. A quantum fredkin gate. *Science Advances*, 2 (3), 2016. DOI: 10.1126/sciadv.1501531.

[107] Shakib Daryanoosh, Sergei Slussarenko, Dominic W. Berry, Howard M. Wiseman, and Geoff J. Pryde. Experimental optical phase measurement approaching the exact Heisenberg limit. *Nature Communications*, 9, 2018. DOI: 10.1038/s41467-018-06601-7.

[108] Zhi Zhao, An-Ning Zhang, Yu-Ao Chen, Han Zhang, Jiang-Feng Du, Tao Yang, and Jian-Wei Pan. Experimental demonstration of a nondestructive controlled-not quantum gate for two independent photon qubits. *Phys. Rev. Lett.*, 94, Jan 2005. DOI: 10.1103/PhysRevLett.94.030501.

[109] Xiao-Hui Bao, Teng-Yun Chen, Qiang Zhang, Jian Yang, Han Zhang, Tao Yang, and Jian-Wei Pan. Optical nondestructive

controlled-not gate without using entangled photons. *Phys. Rev. Lett.*, 98, Apr 2007. DOI: 10.1103/PhysRevLett.98.170502.

[110] Wei-Bo Gao, Alexander M Goebel, Chao-Yang Lu, Han-Ning Dai, Claudia Wagenknecht, Qiang Zhang, Bo Zhao, Cheng-Zhi Peng, Zeng-Bing Chen, Yu-Ao Chen, et al. Teleportation-based realization of an optical quantum two-qubit entangling gate. *Proceedings of the National Academy of Sciences*, 107(49), 2010. DOI: 10.1073/pnas.1005720107.

[111] Ryo Okamoto, Jeremy L O'Brien, Holger F Hofmann, and Shigeki Takeuchi. Realization of a knill-laflamme-milburn controlled-not photonic quantum circuit combining effective optical nonlinearities. *Proceedings of the National Academy of Sciences*, 108(25), 2011. DOI: 10.1073/pnas.101883910.

[112] Jin-Peng Li, Xuemei Gu, Jian Qin, Dian Wu, Xiang You, Hui Wang, Christian Schneider, Sven Höfling, Yong-Heng Huo, Chao-Yang Lu, Nai-Le Liu, Li Li, and Jian-Wei Pan. Heralded nondestructive quantum entangling gate with single-photon sources. *Phys. Rev. Lett.*, 126, Apr 2021. DOI: 10.1103/PhysRevLett.126.140501.

[113] Jonas Zeuner, Aditya N. Sharma, Max Tillmann, René Heilmann, Markus Gräfe, Amir Moqanaki, Alexander Szameit, and Philip Walther. Integrated-optics heralded controlled-NOT gate for polarization-encoded qubits. *npj Quantum Information*, 4, 2018. DOI: 10.1038/s41534-018-0068-0.

[114] Reuben S Aspden, Daniel S Tasca, Andrew Forbes, Robert W Boyd, and Miles J Padgett. Experimental demonstration of klyshko's advanced-wave picture using a coincidence-count based, camera-enabled imaging system. *Journal of Modern Optics*, 61(7), 2014. DOI: 10.1080/09500340.2014.899645.

[115] Min Jiang, Shunlong Luo, and Shuangshuang Fu. Channel-state duality. *Phys. Rev. A*, 87, Feb 2013. DOI: 10.1103/PhysRevA.87.022310.

[116] Jay Lawrence. Rotational covariance and Greenberger-Horne-Zeilinger theorems for three or more particles of any dimension. *Phys. Rev. A*, 89, Jan 2014. DOI: 10.1103/PhysRevA.89.012105.

[117] Lev Vaidman, Yakir Aharonov, and David Z. Albert. How to ascertain the values of sigma$_x$, σ_y, and σ_z of a spin-1/2 particle. *Phys. Rev. Lett.*, 58, Apr 1987. DOI: 10.1103/PhysRevLett.58.1385.

[118] Asher Peres. All the Bell inequalities. *Foundations of Physics*, 29(4), 1999. DOI: 10.1023/A:1018816310000.

[119] Tobias Moroder, Oleg Gittsovich, Marcus Huber, and Otfried Gühne. Steering bound entangled states: A counterexample to the stronger peres conjecture. *Phys. Rev. Lett.*, 113, Aug 2014. DOI: 10.1103/PhysRevLett.113.050404.

[120] Tamás Vértesi and Nicolas Brunner. Disproving the peres conjecture by showing Bell nonlocality from bound entanglement. *Nature Communications*, 5(1), 2014. DOI: 10.1038/ncomms6297.

[121] A. Einstein, B. Podolsky, and N. Rosen. Can quantum-mechanical description of physical reality be considered complete? *Phys. Rev.*, 47, May 1935. DOI: 10.1103/PhysRev.47.777.

[122] J. S. Bell. On the einstein podolsky rosen paradox. *Physics*, 1, Nov 1964. DOI: 10.1103/PhysicsPhysiqueFizika.1.195.

[123] Daniel M Greenberger, Michael A Horne, and Anton Zeilinger. Going beyond Bell's theorem. In *Bell's theorem, quantum theory and conceptions of the universe*. Springer, 1989. DOI: 10.1007/978-94-017-0849-4_10.

[124] Daniel M Greenberger, Michael A Horne, Abner Shimony, and Anton Zeilinger. Bell's theorem without inequalities. *American Journal of Physics*, 58(12), 1990. DOI: 10.1119/1.16243.

[125] Jian-Wei Pan, Dik Bouwmeester, Matthew Daniell, Harald Weinfurter, and Anton Zeilinger. Experimental test of quantum nonlocality in three-photon Greenberger–Horne–Zeilinger entanglement. *Nature*, 403 (6769), 2000. DOI: 10.1038/35000514.

[126] Junghee Ryu, Changhyoup Lee, Zhi Yin, Ramij Rahaman, Dimitris G. Angelakis, Jinhyoung Lee, and Marek Żukowski. Multisetting Greenberger-Horne-Zeilinger theorem. *Phys. Rev. A*, 89, Feb 2014. DOI: 10.1103/PhysRevA.89.024103.

[127] Jay Lawrence. Many-qutrit mermin inequalities with three measure-

ment settings. *arXiv*, 2019. DOI: 10.48550/arXiv.1910.05869.

[128] Manuel Erhard, Mario Krenn, and Anton Zeilinger. Advances in high-dimensional quantum entanglement. *Nature Reviews Physics*, 2(7), 2020. DOI: 10.1038/s42254-020-0193-5.

[129] Xi-Lin Wang, Yi-Han Luo, He-Liang Huang, Ming-Cheng Chen, Zu-En Su, Chang Liu, Chao Chen, Wei Li, Yu-Qiang Fang, Xiao Jiang, Jun Zhang, Li Li, Nai-Le Liu, Chao-Yang Lu, and Jian-Wei Pan. 18-qubit entanglement with six photons' three degrees of freedom. *Phys. Rev. Lett.*, 120, Jun 2018. DOI: 10.1103/PhysRevLett.120.260502.

[130] Alba Cervera-Lierta, Mario Krenn, Alán Aspuru-Guzik, and Alexey Galda. Experimental high-dimensional greenberger-horne-zeilinger entanglement with superconducting transmon qutrits. *Phys. Rev. Applied*, 17, Feb 2022. DOI: 10.1103/PhysRevApplied.17.024062.

[131] Denis Sych and Gerd Leuchs. A complete basis of generalized Bell states. *New Journal of Physics*, 11(1), 2009. DOI: 10.1088/1367-2630/11/1/013006.

[132] Gregg Jaeger. Bell gems: the Bell basis generalized. *Physics Letters A*, 329(6), 2004. DOI: 10.1016/j.physleta.2004.07.037.

[133] F. Verstraete, J. Dehaene, B. De Moor, and H. Verschelde. Four qubits can be entangled in nine different ways. *Phys. Rev. A*, 65, Apr 2002. DOI: 10.1103/PhysRevA.65.052112.

[134] Peter W. Shor. Scheme for reducing decoherence in quantum computer memory. *Phys. Rev. A*, 52, Oct 1995. DOI: 10.1103/PhysRevA.52.R2493.

[135] Andrew Steane. Multiple-particle interference and quantum error correction. *Proceedings of the Royal Society of London. Series A: Mathematical, Physical and Engineering Sciences*, 452(1954), 1996. DOI: 10.1098/rspa.1996.0136.

[136] Raymond Laflamme, Cesar Miquel, Juan Pablo Paz, and Wojciech Hubert Zurek. Perfect quantum error correcting code. *Phys. Rev. Lett.*, 77, Jul 1996. DOI: 10.1103/PhysRevLett.77.198.

[137] David P. DiVincenzo and Peter W. Shor. Fault-tolerant error correction with efficient quantum codes. *Phys. Rev. Lett.*, 77, Oct 1996. DOI: 10.1103/PhysRevLett.77.3260.

[138] Mohamed Bourennane, Manfred Eibl, Sascha Gaertner, Nikolai Kiesel, Christian Kurtsiefer, and Harald Weinfurter. Entanglement persistency of multiphoton entangled states. *Phys. Rev. Lett.*, 96, Mar 2006. DOI: 10.1103/PhysRevLett.96.100502.

[139] M. Murao, D. Jonathan, M. B. Plenio, and V. Vedral. Quantum telecloning and multiparticle entanglement. *Phys. Rev. A*, 59, Jan 1999. DOI: 10.1103/PhysRevA.59.156.

[140] R. Prevedel, G. Cronenberg, M. S. Tame, M. Paternostro, P. Walther, M. S. Kim, and A. Zeilinger. Experimental realization of dicke states of up to six qubits for multiparty quantum networking. *Phys. Rev. Lett.*, 103, Jul 2009. DOI: 10.1103/PhysRevLett.103.020503.

[141] Luca Pezzè, Augusto Smerzi, Markus K. Oberthaler, Roman Schmied, and Philipp Treutlein. Quantum metrology with nonclassical states of atomic ensembles. *Rev. Mod. Phys.*, 90, Sep 2018. DOI: 10.1103/RevModPhys.90.035005.

[142] Tzu-Chieh Wei and Paul M. Goldbart. Geometric measure of entanglement and applications to bipartite and multipartite quantum states. *Phys. Rev. A*, 68, Oct 2003. DOI: 10.1103/PhysRevA.68.042307.

[143] Charles H. Bennett, Gilles Brassard, Claude Crépeau, Richard Jozsa, Asher Peres, and William K. Wootters. Teleporting an unknown quantum state via dual classical and einstein-podolsky-rosen channels. *Phys. Rev. Lett.*, 70, 3 1993. DOI: 10.1103/PhysRevLett.70.1895.

[144] Ye Yeo and Wee Kang Chua. Teleportation and dense coding with genuine multipartite entanglement. *Phys. Rev. Lett.*, 96, Feb 2006. DOI: 10.1103/PhysRevLett.96.060502.

[145] Cezary Śliwa and Konrad Banaszek. Conditional preparation of maximal polarization entanglement. *Phys. Rev. A*, 67, Mar 2003. DOI: 10.1103/PhysRevA.67.030101.

[146] F. V. Gubarev, I. V. Dyakonov, M. Yu. Saygin, G. I. Struchalin, S. S. Straupe, and S. P. Kulik. Improved heralded schemes to generate entangled states from single pho-

tons. *Phys. Rev. A*, 102, Jul 2020. DOI: 10.1103/PhysRevA.102.012604.

[147] Marcus Huber and Julio I. de Vicente. Structure of multidimensional entanglement in multipartite systems. *Phys. Rev. Lett.*, 110, Jan 2013. DOI: 10.1103/PhysRevLett.110.030501.

[148] Marcus Huber, Martí Perarnau-Llobet, and Julio I. de Vicente. Entropy vector formalism and the structure of multidimensional entanglement in multipartite systems. *Phys. Rev. A*, 88, Oct 2013. DOI: 10.1103/PhysRevA.88.042328.

[149] Josh Cadney, Marcus Huber, Noah Linden, and Andreas Winter. Inequalities for the ranks of multipartite quantum states. *Linear Algebra and its Applications*, 452, 2014. DOI: 10.1016/j.laa.2014.03.035.

[150] Matej Pivoluska, Marcus Huber, and Mehul Malik. Layered quantum key distribution. *Phys. Rev. A*, 97, Mar 2018. DOI: 10.1103/PhysRevA.97.032312.

[151] Xuemei Gu, Lijun Chen, and Mario Krenn. Quantum experiments and hypergraphs: Multiphoton sources for quantum interference, quantum computation, and quantum entanglement. *Phys. Rev. A*, 101, Mar 2020. DOI: 10.1103/PhysRevA.101.033816.

[152] Xiao-Min Hu, Wen-Bo Xing, Chao Zhang, Bi-Heng Liu, Matej Pivoluska, Marcus Huber, Yun-Feng Huang, Chuan-Feng Li, and Guang-Can Guo. Experimental creation of multi-photon high-dimensional layered quantum states. *npj Quantum Information*, 6(1), 2020. DOI: 10.1038/s41534-020-00318-6.

[153] Akimasa Miyake. Classification of multipartite entangled states by multidimensional determinants. *Phys. Rev. A*, 67, Jan 2003. DOI: 10.1103/PhysRevA.67.012108.

[154] Asher Peres. Separability criterion for density matrices. *Phys. Rev. Lett.*, 77, Aug 1996. DOI: 10.1103/PhysRevLett.77.1413.

[155] Michał Horodecki. Entanglement measures. *Quantum Information & Computation*, 1 (1), 2001. DOI: 10.5555/2011326.2011328.

[156] Iain DK Brown, Susan Stepney, Anthony Sudbery, and Samuel L Braunstein. Searching for highly entangled multi-qubit states. *Journal of Physics A: Mathematical and General*, 38(5), 2005. DOI: 10.1088/0305-4470/38/5/013.

[157] Alfréd Rényi et al. On measures of entropy and information. In *Proceedings of the fourth Berkeley symposium on mathematical statistics and probability*, 1961. URL `http://l.academicdirect.org/Horticulture/GAs/Refs/Renyi_1961.pdf`.

[158] Wim Van Dam and Patrick Hayden. Renyi-entropic bounds on quantum communication. *arXiv*, 2002. DOI: 10.48550/arXiv.quant-ph/0204093.

[159] Gilad Gour and Nolan R Wallach. All maximally entangled four-qubit states. *Journal of Mathematical Physics*, 51(11), 2010. DOI: 10.1063/1.3511477.

[160] Gavin K. Brennen. An observable measure of entanglement for pure states of multi-qubit systems. *Quantum Inf. Comput.*, 3 (6), 2003. DOI: 10.26421/QIC3.6-5.

[161] David A Meyer and Nolan R Wallach. Global entanglement in multiparticle systems. *Journal of Mathematical Physics*, 43 (9), 2002. DOI: 10.1063/1.1497700.

[162] Marco Enríquez, Zbigniew Puchała, and Karol Życzkowski. Minimal rényi–ingarden–urbanik entropy of multipartite quantum states. *Entropy*, 17(7), 2015. DOI: 10.3390/e17075063.

[163] Wolfram Helwig. Absolutely maximally entangled qudit graph states. *arXiv*, 2013. DOI: 10.48550/arXiv.1306.2879.

[164] Dardo Goyeneche and Karol Życzkowski. Genuinely multipartite entangled states and orthogonal arrays. *Phys. Rev. A*, 90, Aug 2014. DOI: 10.1103/PhysRevA.90.022316.

[165] Fei Shi, Yi Shen, Lin Chen, and Xiande Zhang. Constructions of k-uniform states from mixed orthogonal arrays. *arXiv*, 2020. DOI: 10.48550/arXiv.2006.04086.

[166] A. Higuchi and A. Sudbery. How entangled can two couples get? *Physics Letters A*, 273(4), August 2000. DOI: 10.1016/s0375-9601(00)00480-1.

[167] Lucien Hardy. Nonlocality for two particles without inequalities for almost all entangled states. *Phys. Rev. Lett.*, 71, Sep 1993. DOI: 10.1103/PhysRevLett.71.1665.

[168] Lixiang Chen, Wuhong Zhang, Ziwen Wu,

Jikang Wang, Robert Fickler, and Ebrahim Karimi. Experimental ladder proof of hardy's nonlocality for high-dimensional quantum systems. *Phys. Rev. A*, 96, Aug 2017. DOI: 10.1103/PhysRevA.96.022115.

[169] Kishor Bharti, Tobias Haug, Vlatko Vedral, and Leong-Chuan Kwek. Machine learning meets quantum foundations: A brief survey. *AVS Quantum Science*, 2(3), 2020. DOI: 10.1116/5.0007529.

[170] Joseph Bowles, Flavien Hirsch, and Daniel Cavalcanti. Single-copy activation of Bell nonlocality via broadcasting of quantum states. *Quantum*, 5, jul 2021. ISSN 2521-327X. DOI: 10.22331/q-2021-07-13-499.

[171] Vittorio Giovannetti, Seth Lloyd, and Lorenzo Maccone. Quantum-enhanced measurements: beating the standard quantum limit. *Science*, 306(5700), 2004. DOI: 10.1126/science.1104149.

[172] Christoph F. Wildfeuer, Austin P. Lund, and Jonathan P. Dowling. Strong violations of Bell-type inequalities for path-entangled number states. *Phys. Rev. A*, 76, Nov 2007. DOI: 10.1103/PhysRevA.76.052101.

[173] Yonatan Israel, Shamir Rosen, and Yaron Silberberg. Supersensitive polarization microscopy using noon states of light. *Phys. Rev. Lett.*, 112, Mar 2014. DOI: 10.1103/PhysRevLett.112.103604.

[174] Takafumi Ono, Ryo Okamoto, and Shigeki Takeuchi. An entanglement-enhanced microscope. *Nature Communications*, 4(1), 2013. DOI: 10.1038/ncomms3426.

[175] Xiaoqin Gao, Yingwen Zhang, Alessio D'Errico, Khabat Heshami, and Ebrahim Karimi. High-speed imaging of spatiotemporal correlations in hong-ou-mandel interference. *Optics Express*, 30(11), 2022. DOI: 10.1364/OE.456433.

[176] Bienvenu Ndagano, Hugo Defienne, Dominic Branford, Yash D Shah, Ashley Lyons, Niclas Westerberg, Erik M Gauger, and Daniele Faccio. Quantum microscopy based on hong–ou–mandel interference. *Nature Photonics*, 16(5), 2022. DOI: 10.1038/s41566-022-00980-6.

[177] Morgan W Mitchell, Jeff S Lundeen, and Aephraem M Steinberg. Super-resolving phase measurements with a multiphoton entangled state. *Nature*, 429(6988), 2004. DOI: 10.1038/nature02493.

[178] Philip Walther, Jian-Wei Pan, Markus Aspelmeyer, Rupert Ursin, Sara Gasparoni, and Anton Zeilinger. De broglie wavelength of a non-local four-photon state. *Nature*, 429(6988), 2004. DOI: 10.1038/nature02552.

[179] F. W. Sun, B. H. Liu, Y. F. Huang, Z. Y. Ou, and G. C. Guo. Observation of the four-photon de broglie wavelength by state-projection measurement. *Phys. Rev. A*, 74, Sep 2006. DOI: 10.1103/PhysRevA.74.033812.

[180] K. J. Resch, K. L. Pregnell, R. Prevedel, A. Gilchrist, G. J. Pryde, J. L. O'Brien, and A. G. White. Time-reversal and super-resolving phase measurements. *Phys. Rev. Lett.*, 98, May 2007. DOI: 10.1103/PhysRevLett.98.223601.

[181] Agedi N. Boto, Pieter Kok, Daniel S. Abrams, Samuel L. Braunstein, Colin P. Williams, and Jonathan P. Dowling. Quantum interferometric optical lithography: Exploiting entanglement to beat the diffraction limit. *Phys. Rev. Lett.*, 85, Sep 2000. DOI: 10.1103/PhysRevLett.85.2733.

[182] Erwin Schrödinger. Die gegenwärtige situation in der quantenmechanik. *Naturwissenschaften*, 23(50), 1935. URL `https://informationphilosopher.com/solutions/scientists/schrodinger/Die_Situation-3.pdf`.

[183] Kishore T. Kapale and Jonathan P. Dowling. Bootstrapping approach for generating maximally path-entangled photon states. *Phys. Rev. Lett.*, 99, Aug 2007. DOI: 10.1103/PhysRevLett.99.053602.

[184] Hugo Cable and Jonathan P. Dowling. Efficient generation of large number-path entanglement using only linear optics and feed-forward. *Phys. Rev. Lett.*, 99, Oct 2007. DOI: 10.1103/PhysRevLett.99.163604.

[185] Luca Pezzé and Augusto Smerzi. Mach-zehnder interferometry at the heisenberg limit with coherent and squeezed-vacuum light. *Phys. Rev. Lett.*, 100, Feb 2008. DOI: 10.1103/PhysRevLett.100.073601.

[186] Holger F. Hofmann and Takafumi Ono. High-photon-number path entanglement in

the interference of spontaneously down-converted photon pairs with coherent laser light. *Phys. Rev. A*, 76, Sep 2007. DOI: 10.1103/PhysRevA.76.031806.

[187] Y. Israel, I. Afek, S. Rosen, O. Ambar, and Y. Silberberg. Experimental tomography of noon states with large photon numbers. *Phys. Rev. A*, 85, Feb 2012. DOI: 10.1103/PhysRevA.85.022115.

[188] Peter C. Humphreys, Marco Barbieri, Animesh Datta, and Ian A. Walmsley. Quantum enhanced multiple phase estimation. *Phys. Rev. Lett.*, 111, Aug 2013. DOI: 10.1103/PhysRevLett.111.070403.

[189] P. A. Knott, T. J. Proctor, A. J. Hayes, J. F. Ralph, P. Kok, and J. A. Dunningham. Local versus global strategies in multiparameter estimation. *Phys. Rev. A*, 94, Dec 2016. DOI: 10.1103/PhysRevA.94.062312.

[190] Heonoh Kim, Hee Su Park, and Sang-Kyung Choi. Three-photon n00n states generated by photon subtraction from double photon pairs. *Optics Express*, 17(22), 2009. DOI: 10.1364/OE.17.019720.

[191] Yosep Kim, Gunnar Björk, and Yoon-Ho Kim. Experimental characterization of quantum polarization of three-photon states. *Phys. Rev. A*, 96, Sep 2017. DOI: 10.1103/PhysRevA.96.033840.

[192] Yong-Su Kim, Osung Kwon, Sang Min Lee, Jong-Chan Lee, Heonoh Kim, Sang-Kyung Choi, Hee Su Park, and Yoon-Ho Kim. Observation of young's double-slit interference with the three-photon n00n state. *Optics Express*, 19(25), 2011. DOI: 10.1364/OE.19.024957.

[193] Gunnar Björk, Markus Grassl, Pablo de la Hoz, Gerd Leuchs, and Luis L Sánchez-Soto. Stars of the quantum universe: extremal constellations on the poincaré sphere. *Physica Scripta*, 90(10), 2015. DOI: 10.1088/0031-8949/90/10/108008.

[194] G. Björk, A. B. Klimov, P. de la Hoz, M. Grassl, G. Leuchs, and L. L. Sánchez-Soto. Extremal quantum states and their majorana constellations. *Phys. Rev. A*, 92, Sep 2015. DOI: 10.1103/PhysRevA.92.031801.

[195] Frederic Bouchard, P de la Hoz, Gunnar Björk, RW Boyd, Markus Grassl, Z Hradil, E Karimi, AB Klimov, Gerd Leuchs, J Řeháček, et al. Quantum metrology at the limit with extremal majorana constellations. *Optica*, 4(11), 2017. DOI: 10.1364/OPTICA.4.001429.

[196] Ettore Majorana. Atomi orientati in campo magnetico variabile. *Il Nuovo Cimento (1924-1942)*, 9(2), 1932. DOI: 10.1007/BF02960953.

[197] John H Conway, Ronald H Hardin, and Neil JA Sloane. Packing lines, planes, etc.: Packings in grassmannian spaces. *Experimental mathematics*, 5(2), 1996. DOI: 10.1080/10586458.1996.10504585.

[198] Edward B Saff and Amo BJ Kuijlaars. Distributing many points on a sphere. *The mathematical intelligencer*, 19(1), 1997. DOI: 10.1007/BF03024331.

[199] Armin Tavakoli and Nicolas Gisin. The platonic solids and fundamental tests of quantum mechanics. *Quantum*, 4, 2020. DOI: 10.22331/q-2020-07-09-293.

[200] Károly F Pál and Tamás Vértesi. Platonic Bell inequalities for all dimensions. *Quantum*, 6, 2022. DOI: 10.22331/q-2022-07-07-756.

[201] Markus Grassl. Extremal polarization states, 2015. URL `http://polarization.markus-grassl.de/index.html`.

[202] Hugo Ferretti. *Quantum Parameter Estimation in the Laboratory*. PhD thesis, University of Toronto (Canada), 2022. URL `https://www.proquest.com/dissertations-theses/quantum-parameter-estimation-laboratory/docview/2646725686/se-2`.

[203] Alán Aspuru-Guzik and Philip Walther. Photonic quantum simulators. *Nature physics*, 8(4), 2012. DOI: 10.1038/nphys2253.

[204] Ulrich Schollwöck. The density-matrix renormalization group in the age of matrix product states. *Annals of physics*, 326(1), 2011. DOI: 10.1016/j.aop.2010.09.012.

[205] J. Ignacio Cirac, David Pérez-Garcia, Norbert Schuch, and Frank Verstraete. Matrix product states and projected entangled pair states: Concepts, symmetries, theorems. *Rev. Mod. Phys.*, 93, Dec 2021. DOI: 10.1103/RevModPhys.93.045003.

[206] Jorge Miguel-Ramiro and Wolfgang Dür.

Delocalized information in quantum networks. *New Journal of Physics*, 22(4), 2020. DOI: 10.1088/1367-2630/ab784d.

[207] D. Gross and J. Eisert. Quantum computational webs. *Phys. Rev. A*, 82, Oct 2010. DOI: 10.1103/PhysRevA.82.040303.

[208] Hannes Bernien, Sylvain Schwartz, Alexander Keesling, Harry Levine, Ahmed Omran, Hannes Pichler, Soonwon Choi, Alexander S Zibrov, Manuel Endres, Markus Greiner, et al. Probing many-body dynamics on a 51-atom quantum simulator. *Nature*, 551, 2017. DOI: 10.1038/nature24622.

[209] D. Perez-Garcia, F. Verstraete, M. M. Wolf, and J. I. Cirac. Matrix product state representations. *Quantum Info. Comput.*, 7 (5), Jul 2007. ISSN 1533-7146. DOI: 10.5555/2011832.2011833.

[210] Olof Salberger and Vladimir Korepin. Fredkin spin chain. In *Ludwig Faddeev Memorial Volume: A Life In Mathematical Physics*. World Scientific, 2018. DOI: 10.1142/9789813233867_0022.

[211] Ramis Movassagh. Entanglement and correlation functions of the quantum motzkin spin-chain. *Journal of Mathematical Physics*, 58(3), 2017. DOI: 10.1063/1.4977829.

[212] Libor Caha and Daniel Nagaj. The pair-flip model: a very entangled translationally invariant spin chain. *arXiv*, 2018. DOI: 10.48550/arXiv.1805.07168.

[213] Khagendra Adhikari and K. S. D. Beach. Deforming the fredkin spin chain away from its frustration-free point. *Phys. Rev. B*, 99, Feb 2019. DOI: 10.1103/PhysRevB.99.054436.

[214] Colin P. Williams. *Explorations in Quantum Computing, Second Edition*. Springer, 2011. DOI: 10.1007/978-1-84628-887-6.

[215] Peter BR Nisbet-Jones, Jerome Dilley, Annemarie Holleczek, Oliver Barter, and Axel Kuhn. Photonic qubits, qutrits and ququads accurately prepared and delivered on demand. *New Journal of Physics*, 15(5), 2013. DOI: 10.1088/1367-2630/15/5/053007.

[216] C. Senko, P. Richerme, J. Smith, A. Lee, I. Cohen, A. Retzker, and C. Monroe. Realization of a quantum integer-spin chain with controllable interactions. *Phys. Rev. X*, 5, Jun 2015. DOI: 10.1103/PhysRevX.5.021026.

[217] Barry Bradlyn, Jennifer Cano, Zhijun Wang, MG Vergniory, C Felser, Robert Joseph Cava, and B Andrei Bernevig. Beyond dirac and weyl fermions: Unconventional quasiparticles in conventional crystals. *Science*, 353(6299), 2016. DOI: 10.1126/science.aaf5037.

[218] A Klümper, A Schadschneider, and J Zittartz. Matrix product ground states for one-dimensional spin-1 quantum antiferromagnets. *EPL (Europhysics Letters)*, 24(4), 1993. DOI: 10.1209/0295-5075/24/4/010.

[219] Ian Affleck, Tom Kennedy, Elliott H. Lieb, and Hal Tasaki. Rigorous results on valence-bond ground states in antiferromagnets. *Phys. Rev. Lett.*, Aug 1987. DOI: 10.1103/PhysRevLett.59.799.

[220] Ian Affleck, Tom Kennedy, Elliott H Lieb, and Hal Tasaki. Valence bond ground states in isotropic quantum antiferromagnets. In *Condensed matter physics and exactly soluble models*. Springer, 1988. DOI: 10.1007/978-3-662-06390-3_19.

[221] K. Wierschem and K. S. D. Beach. Detection of symmetry-protected topological order in aklt states by exact evaluation of the strange correlator. *Phys. Rev. B*, 93, Jun 2016. DOI: 10.1103/PhysRevB.93.245141.

[222] Frank Pollmann, Erez Berg, Ari M. Turner, and Masaki Oshikawa. Symmetry protection of topological phases in one-dimensional quantum spin systems. *Phys. Rev. B*, 85, Feb 2012. DOI: 10.1103/PhysRevB.85.075125.

[223] Sergey Bravyi, Libor Caha, Ramis Movassagh, Daniel Nagaj, and Peter W. Shor. Criticality without frustration for quantum spin-1 chains. *Phys. Rev. Lett.*, 109, Nov 2012. DOI: 10.1103/PhysRevLett.109.207202.

[224] Zhao Zhang, Amr Ahmadain, and Israel Klich. Novel quantum phase transition from bounded to extensive entanglement. *Proceedings of the National Academy of Sciences*, 114(20), 2017. DOI: 10.1073/pnas.1702029114.

[225] Eleonora Nagali, Linda Sansoni, Lorenzo Marrucci, Enrico Santamato, and Fabio Sciarrino. Experimental generation and

characterization of single-photon hybrid ququarts based on polarization and orbital angular momentum encoding. *Phys. Rev. A*, 81, May 2010. DOI: 10.1103/PhysRevA.81.052317.

[226] Harald Niggemann, Andreas Klümper, and Johannes Zittartz. Quantum phase transition in spin-3/2 systems on the hexagonal lattice—optimum ground state approach. *Zeitschrift für Physik B Condensed Matter*, 104(1), 1997. DOI: 10.1007/s002570050425.

[227] S Alipour, S Baghbanzadeh, and V Karimipour. Matrix product representations for spin-(1/2) and spin-(3/2) spontaneous quantum ferrimagnets. *EPL (Europhysics Letters)*, 84(6), 2009. DOI: 10.1209/0295-5075/84/67006.

[228] Julia M. Link, Igor Boettcher, and Igor F. Herbut. d-wave superconductivity and bogoliubov-fermi surfaces in rarita-schwinger-weyl semimetals. *Phys. Rev. B*, 101, May 2020. DOI: 10.1103/PhysRevB.101.184503.

[229] MA Ahrens, A Schadschneider, and J Zittartz. Exact ground states of spin-2 chains. *EPL (Europhysics Letters)*, 59(6), 2002. DOI: 10.1209/epl/i2002-00126-5.

[230] Maksym Serbyn, Dmitry A Abanin, and Zlatko Papić. Quantum many-body scars and weak breaking of ergodicity. *Nature Physics*, 17(6), 2021. DOI: 10.1038/s41567-021-01230-2.

[231] Sanjay Moudgalya, Nicolas Regnault, and B. Andrei Bernevig. Entanglement of exact excited states of affleck-kennedy-lieb-tasaki models: Exact results, many-body scars, and violation of the strong eigenstate thermalization hypothesis. *Phys. Rev. B*, 98, Dec 2018. DOI: 10.1103/PhysRevB.98.235156.

[232] Sanjay Moudgalya, Stephan Rachel, B. Andrei Bernevig, and Nicolas Regnault. Exact excited states of nonintegrable models. *Phys. Rev. B*, 98, Dec 2018. DOI: 10.1103/PhysRevB.98.235155.

[233] Soonwon Choi, Christopher J. Turner, Hannes Pichler, Wen Wei Ho, Alexios A. Michailidis, Zlatko Papić, Maksym Serbyn, Mikhail D. Lukin, and Dmitry A. Abanin. Emergent SU(2) dynamics and perfect quantum many-body scars. *Phys. Rev. Lett.*, 122, Jun 2019. DOI: 10.1103/PhysRevLett.122.220603.

[234] Naoyuki Shibata, Nobuyuki Yoshioka, and Hosho Katsura. Onsager's scars in disordered spin chains. *Phys. Rev. Lett.*, 124, May 2020. DOI: 10.1103/PhysRevLett.124.180604.

[235] Cheng-Ju Lin and Olexei I. Motrunich. Exact quantum many-body scar states in the rydberg-blockaded atom chain. *Phys. Rev. Lett.*, 122, Apr 2019. DOI: 10.1103/PhysRevLett.122.173401.

[236] F. Troiani. Entanglement swapping with energy-polarization-entangled photons from quantum dot cascade decay. *Phys. Rev. B*, 90, Dec 2014. DOI: 10.1103/PhysRevB.90.245419.

[237] Michael Zopf, Robert Keil, Yan Chen, Jingzhong Yang, Disheng Chen, Fei Ding, and Oliver G. Schmidt. Entanglement swapping with semiconductor-generated photons violates Bell's inequality. *Phys. Rev. Lett.*, 123, Oct 2019. DOI: 10.1103/PhysRevLett.123.160502.

[238] Jian-Wei Pan and Anton Zeilinger. Greenberger-Horne-Zeilinger-state analyzer. *Phys. Rev. A*, 57, Mar 1998. DOI: 10.1103/PhysRevA.57.2208.

[239] János A Bergou. Discrimination of quantum states. *Journal of Modern Optics*, 57(3), 2010. DOI: 10.1080/09500340903477756.

[240] N. Bent, H. Qassim, A. A. Tahir, D. Sych, G. Leuchs, L. L. Sánchez-Soto, E. Karimi, and R. W. Boyd. Experimental realization of quantum tomography of photonic qudits via symmetric informationally complete positive operator-valued measures. *Phys. Rev. X*, 5, Oct 2015. DOI: 10.1103/PhysRevX.5.041006.

[241] Carlton M Caves, Christopher A Fuchs, and Rüdiger Schack. Unknown quantum states: the quantum de finetti representation. *Journal of Mathematical Physics*, 43 (9), 2002. DOI: 10.1063/1.1494475.

[242] A. Hayashi, M. Horibe, and T. Hashimoto. Mean king's problem with mutually unbiased bases and orthogonal latin squares. *Phys. Rev. A.*, May 2005. DOI: 10.1103/PhysRevA.71.052331.

[243] Oliver Schulz, Ruprecht Steinhübl, Markus

Weber, Berthold-Georg Englert, Christian Kurtsiefer, and Harald Weinfurter. Ascertaining the values of σ_x, σ_y, and σ_z of a polarization qubit. *Phys. Rev. Lett.*, 90, Apr 2003. DOI: 10.1103/PhysRevLett.90.177901.

[244] Berthold-Georg Englert, Christian Kurtsiefer, and Harald Weinfurter. Universal unitary gate for single-photon 2-qubit states. *Physical Review A*, 63, Feb 2001. DOI: 10.1103/PhysRevA.63.032303.

[245] Cheng-Qiu Hu, Jun Gao, Lu-Feng Qiao, Ruo-Jing Ren, Zhu Cao, Zeng-Quan Yan, Zhi-Qiang Jiao, Hao Tang, Zhi-Hao Ma, and Xian-Min Jin. Experimental test of tracking the king problem. *Research*, 2019, Dec 2019. DOI: 10.34133/2019/3474305.

[246] T. B. Pittman, B. C. Jacobs, and J. D. Franson. Demonstration of nondeterministic quantum logic operations using linear optical elements. *Phys. Rev. Lett.*, 88, Jun 2002. DOI: 10.1103/PhysRevLett.88.257902.

[247] Stuart M Marshall, Alastair RG Murray, and Leroy Cronin. A probabilistic framework for identifying biosignatures using pathway complexity. *Philosophical Transactions of the Royal Society A: Mathematical, Physical and Engineering Sciences*, 375 (2109), 2017. DOI: 10.1098/rsta.2016.0342.

[248] Stuart M Marshall, Cole Mathis, Emma Carrick, Graham Keenan, Geoffrey JT Cooper, Heather Graham, Matthew Craven, Piotr S Gromski, Douglas G Moore, Sara Walker, et al. Identifying molecules as biosignatures with assembly theory and mass spectrometry. *Nature Communications*, 12(1), 2021. DOI: 10.1038/s41467-021-23258-x.

[249] Matthias J Bayerbach, Simone E D'Aurelio, Peter van Loock, and Stefanie Barz. Bell-state measurement exceeding 50% success probability with linear optics. *Science Advances*, 9(32), 2023. DOI: 10.1126/sciadv.adf4080.

[250] D Blume. Few-body physics with ultracold atomic and molecular systems in traps. *Reports on Progress in Physics*, 75, mar 2012. DOI: 10.1088/0034-4885/75/4/046401.

[251] Daniel E. Parker, Xiangyu Cao, Alexander Avdoshkin, Thomas Scaffidi, and Ehud Altman. A universal operator growth hypothesis. *Phys. Rev. X*, 9, Oct 2019. DOI: 10.1103/PhysRevX.9.041017.

[252] Mario Krenn, Robert Pollice, Si Yue Guo, Matteo Aldeghi, Alba Cervera-Lierta, Pascal Friederich, Gabriel dos Passos Gomes, Florian Häse, Adrian Jinich, Akshat Kumar Nigam, et al. On scientific understanding with artificial intelligence. *Nature Reviews Physics*, 2022. DOI: 10.1038/s42254-022-00518-3.

[253] Terry Rudolph. Terry vs an ai, round 1: Heralding single-rail (approximate?) 4-ghz state from squeezed sources. *arXiv*, 2023. DOI: 10.48550/arXiv.2303.05514.

Chapter 3

Deep Quantum Graph Dreaming

This chapter is based on the following publication.

Jaouni, Tareq, Sören Arlt, Carlos Ruiz-Gonzalez, Ebrahim Karimi, Xuemei Gu, and Mario Krenn. "Deep Quantum Graph Dreaming: Deciphering Neural Network Insights into Quantum Experiments." *Machine Learning: Science and Technology 5 (1)* (2024): 015029

DOI: https://doi.org/10.1088/2632-2153/ad2628

3.1 Overview

As we have seen in Chapter 2, we can employ the PyTheus framework to find graph-theoretic, experimental solutions to various quantum optical phenomena. Going beyond the question of experimental implementation, one may inquire if it is possible to discover new physics through the solutions of such frameworks. This question has been posited since the conception of Melvin [26], which performs a topological search on arrangements of optical elements. Through Melvin's solutions, scientists were able to uncover a new paradigm for entanglement generation [32], and new schemes for multipartite quantum gates [40]. However, the discovery of new science was impeded by the stochastic processes from which these solutions arise, as well as the inherent difficulty in interpreting arrangements of optical elements; altogether, this required weeks of tedious simplifications of the solutions. To this end of finding more interpretable solutions which facilitates new scientific discoveries, we have already seen the improvements which PyTheus provides. It has enabled the discovery of a new kind of multiphoton interference [41] and, as we will see in Chapter 4,

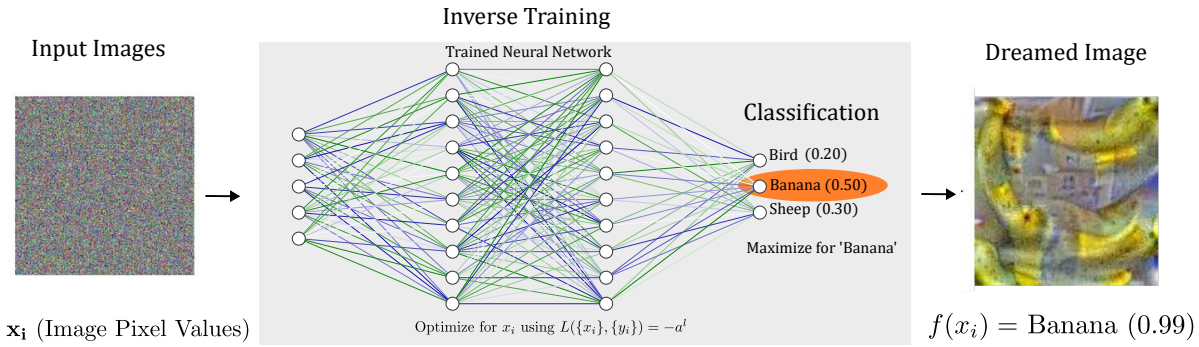

Figure 3.1: **Illustration behind deep dreaming approach**. We consider a neural network that has been trained to assign onto an input image a classification label. During inverse training, the weights and biases of a trained neural network are frozen completely. The optimization routine is instead applied to the input image itself. The approach, therefore, searches for the image which maximizes the activation of a particular neuron. Dreamed image taken from [1].

an experimental scheme that, for the first time, solves the Mean King's Problem in higher dimensions.

In our efforts to uncover more novel scientific insights from the computer, we may be interested in understanding the logic behind its discoveries. To this end, we may leverage XAI techniques from *computer vision techniques* that probes into what an artificial neural network learns about quantum experiments. The application of neural networks has already shown promise to solve various tasks in quantum physics [42, 43, 44], though their inscrutability frustrates the scientist looking to interpret the neural network's logic. The application of XAI has been successful towards rediscovering physics built upon centuries of work [45, 46], and in discovering interpretable representations on the correlation of quantum experiments in entanglement [47].

Here, we consider the *deep dreaming* as was introduced in [1] and applied to guide the optimization of quantum circuits [48] and molecules [49] to target property, to rediscover the thermodynamic arrow of time [50], and to verify the classification of entanglement spectra of many-body quantum systems [51]. Figure 3.1 illustrates the concept when applied to a neural network trained for image classification. The tunable parameters of the neural network are first optimized via *forward training*, in which the neural network is trained on many examples of quantum experiments. Once this training is done, we sample an input vector $\mathbf{x}$ from the dataset and *inverse train* the network. Unlike the forward process, the

network's parameters are no longer tuned. Instead, the input vector itself is transformed such that the activation of the neural network is maximized. The end result of the process is a transformed input vector that reflects what the neural network is most interested in seeing. This can be applied to any point at the network. For example, at the output layer, the intermediate steps of the mutation process gives us a snapshot of the learned startegies which the network employs to achieve a given task. One can also inverse train on the neurons of any hidden layer of the network. The dreamed output tends to reveal abstract features of the input image on which the network is seeing, which allows us to discern what features does the network identifies from $\mathbf{x}$ in the formulation of its prediction.

3.2 Neural Network Primer

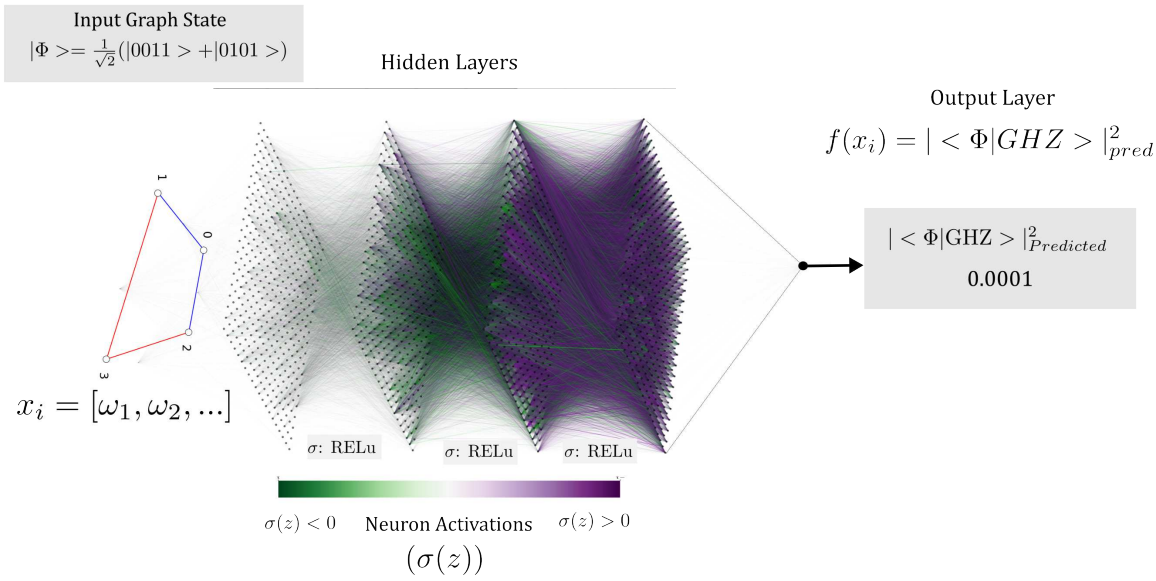

Figure 3.2: **An example of a feed-forward neural network.** We illustrate a $[400^4]$ neural network that is trained to make predictions on the fidelity of an input quantum graph, represented with edge weights $\omega_1, \omega_2, ...$, with respect to the GHZ state. The particular architecture shown consists of an input layer, 4 hidden layers, each with 400 neurons, and an output layer consisting of one neuron. In between the hidden layers of the network are nonlinear activation functions which transforms the neural network inputs z.

We now present a brief introduction to neural networks. In the most general sense, neu-

ral networks are mathematical functions $f : \mathbb{R}^m \to \mathbb{R}^n$ that take as input $\mathbf{x} = (x_1.x_2, ..., x_m)$ and outputs a vector $\mathbf{y} = (y_1, y_2, ..., y_n)$, which we also refer to as the neural network's predicted value, $\mathbf{f}(\mathbf{x_i})$. In this work, we concern ourselves with feed-forward neural networks, an example of which is shown in Figure 3.2. For a more comprehensive introduction into the subject at large, see e.g [52, 53]

3.2.1 Anatomy

The most basic unit of the neural network is the neuron. Let $x_1, x_2...$ here represent the immediate inputs to the neuron, then the output of the j^{th} neuron, also referred to as the *neuron activation* is given by

$$a_j = \sigma(\sum_i w_i x_i + b) = \sigma(z). \tag{3.1}$$

Where the inputs of the neuron have corresponding real-valued weights $\{w_i\}$, $b \in \mathbb{R}$ is a bias parameter attributed to the neuron, σ is a nonlinear activation function, and we can refer to $z = \sum_i w_i x_i + b$. As we will see, different choices of the activation function can affect the rate at which the neural network learns at its different parts. In our case, we are most concerned with the Rectified Linear Unit (ReLU) nonlinear activation function, which is defined as

$$\sigma_{ReLU}(z) = max(z, 0). \tag{3.2}$$

A neural network consists of clusters of neurons that are arranged in one or more *layers*. The input vector to the neural network, $\mathbf{x}$ goes through an input layer consisting of a number of neurons. This produces a corresponding amount of neuron activations, which are fed into the second layer, also referred to as a *hidden layer*. This process continues until the final, or *output layer*, which outputs the $\mathbf{y}$ vector. The network is fully connected in the sense that each neuron in a hidden layer receives the activations of all the neurons in the preceding layer.

3.2.2 Forward Training

The activations of each neuron in the network can be described in terms of randomly initalized, *tunable* parameters θ, which consists of weights $\{w_i\}$ and bias b. We optimize these

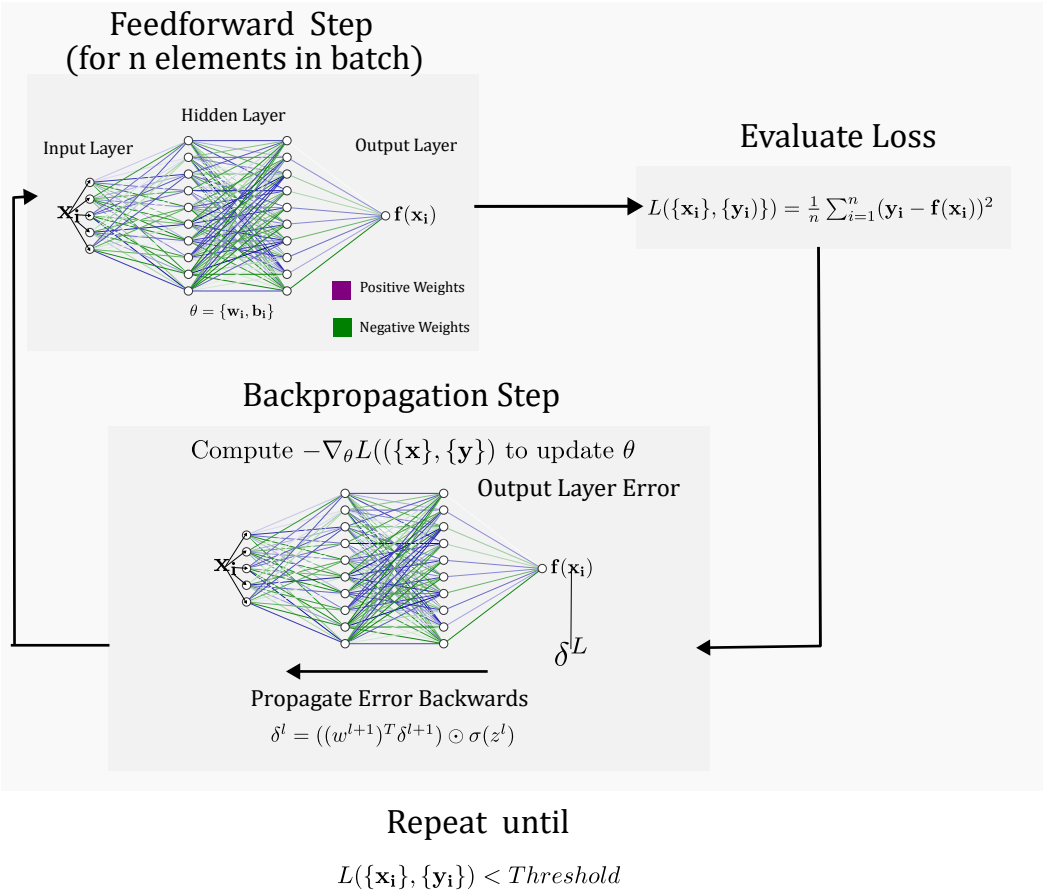

Figure 3.3: **Summary of forward training routine.** The tunable parameters of the network – weights and biases – are randomly initialized and undergo an optimization process. In each iteration, we evaluate error between the network's prediction of the output, $f(\mathbf{x_i})$, and the true value y_i. Towards minimizing the loss, we perform gradient descent by evaluating via back-propagation over the entire network the rate in which each tuneable parameter changes the loss. This process continues until some threshold is reached.

parameters of the neural network through *forward training*. We prepare datasets consisting of various input-output pairs $(\mathbf{x}_i, \mathbf{y}_i)$. These examples are then fed onto the neural network, which produces an output $\mathbf{f}(\mathbf{x_i})$. We then evaluate the prediction's closeness with respect to the true output $\mathbf{y}_i$ using a *loss function*. One example of a loss function with which we concern ourselves is the *mean squared error* (MSE). Suppose that we have n input-output

pairs, or *training examples*, then the MSE is defined as

$$L(\mathbf{x}, \mathbf{y}) = \frac{1}{n} \sum_{i=1}^{n} (\mathbf{y_i} - \mathbf{f}(\mathbf{x_i}))^2. \tag{3.3}$$

We proceed to tune our parameters in θ towards minimizing this loss function via *gradient descent*. Specifically, we compute $-\nabla_\theta L((\mathbf{x}, \mathbf{y})$, so that θ is updated in the opposite direction of the gradient. This update can take place once the entire set of training examples have been evaluated, but we can also choose to partition the set into *batches* and perform the update once each batch is evaluated. This is also known as *mini-batch* or *stochastic gradient descent*, and is quicker to compute.

The gradients corresponding to each one of the weight and bias parameters can be computed efficiently via *back-propagation*: In essence, we compute the 'error' of the neural network at the output layer, δ^L, which we can define as the rate of change of the loss function with respect to the weighted neuron inputs within the layer

$$\delta^l = \frac{\partial L}{\partial z^l}, \tag{3.4}$$

where $z^l = (z_1^l, z_2^l, ...)$ is a vector encapsulating all of the neuron weighted inputs in the output layer. Knowledge of the output layer error, along with the weights connected to the output layer, allows us to compute the errors of all the preceding layers in a process known as backpropagation. The gradients of the weights and biases corresponding to each layer of the network are then directly related to the errors of the layers according to

$$\frac{\partial L}{\partial b^l} = \delta^l, \frac{\partial L}{\partial w^l} = \sigma(z^{l-1})\delta^l \tag{3.5}$$

Where $b^l = (b_1^l, b_2^l, ..., b_j^l)$ and

$$w^l = \begin{bmatrix} w_{00} & w_{01} & ... \\ w_{10} & ... & ... \\ ... & ... & ... \end{bmatrix} \tag{3.6}$$

,

respectively, refer to the bias vector and weight matrix associated to each layer; the components of these vectors are those specific to the j^{th} neuron of the layer.

Machine Learning: Science and Technology

Deep quantum graph dreaming: deciphering neural network insights into quantum experiments

IOP Publishing Mach. Learn.: Sci. Technol. 5 (2024) 015029 https://doi.org/10.1088/2632-2153/ad2628

MACHINE LEARNING
Science and Technology

PAPER

Deep quantum graph dreaming: deciphering neural network insights into quantum experiments

Tareq Jaouni[1,2,*], Sören Arlt[1], Carlos Ruiz-Gonzalez[1], Ebrahim Karimi[1,2], Xuemei Gu[1] and Mario Krenn[1,*]

[1] Max Planck Institute for the Science of Light, Erlangen, Germany
[2] Nexus for Quantum Technologies, University of Ottawa, K1N 6N5, ON, Ottawa, Canada
[*] Authors to whom any correspondence should be addressed.

E-mail: tjaou104@uottawa.ca and mario.krenn@mpl.mpg.de

Keywords: neural network interpretability, deep dreaming, quantum physics

OPEN ACCESS

RECEIVED
4 October 2023

REVISED
20 December 2023

ACCEPTED FOR PUBLICATION
31 January 2024

PUBLISHED
15 February 2024

Abstract

Despite their promise to facilitate new scientific discoveries, the opaqueness of neural networks presents a challenge in interpreting the logic behind their findings. Here, we use a eXplainable-AI technique called *inception* or *deep dreaming*, which has been invented in machine learning for computer vision. We use this technique to explore what neural networks learn about quantum optics experiments. Our story begins by training deep neural networks on the properties of quantum systems. Once trained, we 'invert' the neural network—effectively asking how it imagines a quantum system with a specific property, and how it would continuously modify the quantum system to change a property. We find that the network can shift the initial distribution of properties of the quantum system, and we can conceptualize the learned strategies of the neural network. Interestingly, we find that, in the first layers, the neural network identifies simple properties, while in the deeper ones, it can identify complex quantum structures and even quantum entanglement. This is in reminiscence of long-understood properties known in computer vision, which we now identify in a complex natural science task. Our approach could be useful in a more interpretable way to develop new advanced AI-based scientific discovery techniques in quantum physics.

1. Introduction

Neural networks have been demonstrably promising towards solving various tasks in quantum science [1–3]. One notorious frustration concerning neural networks, however, lays in their inscrutability: modern architectures often contain millions of trainable parameters, and it is not readily apparent what role that they each play in the network's prediction. We may, therefore, inquire about what learned concepts from the data that the network utilizes to formulate its prediction, an important prerequisite in achieving scientific understanding [4]. This has since motivated the development of eXplainable-AI (XAI), which interprets how the network comes up with its solutions [5–8]. These developments have spurred physicists to address the problem of interpretability, resulting in the rediscovery of long-standing physics concepts [9, 10], the identification of phase transitions in quantum many-body physics [11–14], the compression of many-body quantum systems [15], and the study on the relationship between quantum systems and their entanglement properties [16, 17].

Here, we apply neural networks in the design of quantum optical experiments. The growing complexity of quantum information tasks has since motivated the design of computational methods capable of navigating the vast combintorical space of possible experimental designs that involve unintuitive phenomena [18]. To this end, scientists have developed automated design and machine learning routines [19], including some that leverage genetic algorithms [20, 21], active learning approaches [22] and the optimization of parameterized quantum circuits [23–25]. One may inquire if we may be able to learn new physics from the discoveries made by such algorithms. For instance, the computer algorithm Melvin [19], which topologically searches for arrangements of optical elements, has led to the discovery of new concepts

such as the generation of entanglement by path identity [26] and the creation of multipartite quantum gates [27]. However, the interpretability of these solutions is obfuscated by the stochasticity of the processes that create them as well as the unintuitiveness of their representations. The recent invention of THESEUS [24], and its successor PYTHEUS [25] addresses this through the topological optimization of highly interpretable, graph-based representation of quantum optical experiments. This has already enabled new scientific discoveries, such as a new form of multi-photon interference [28], and novel experimental schemes for high-dimensional quantum measurement [29].

To this point, the extraction and generalization of new concepts has largely been confined to analyzing the optimal solutions discovered by these algorithms. However, we may inquire if we can learn more physics by probing the rationale behind the computer's discoveries. Little attention has hitherto been given towards the application of XAI techniques on neural networks trained on quantum experiments, which may allow us to conceptualize what our algorithm has learned. In so doing, we may guide the creation of AI-based design techniques for quantum experiments that are more reliable and interpretable.

In this work, we present an interpretability tool based on the inceptionism technique in computer vision, better known as deep dreaming [30]. This technique has been applied to iteratively guide the automated design of quantum circuits [31] and molecules [32] towards optimizing a target property; it has also been applied in [33] to verify the reliability of a network trained to classify the entanglement spectra of many-body quantum systems. More importantly, it also lets us visualize what physical insights has the neural network gained from the training data. This lets us better discern the strategies applied throughout automated design processes, as well as to verify physical concepts rediscovered by the network, such as the thermodynamic arrow of time [34].

Here, we adapt this approach to quantum graphs. We train a deep neural network to predict properties of quantum systems, then inverse the training to optimize for a target property. We observe that the inverse training dramatically shifts the initial distribution of properties. We also show that, by visualizing the evolution of quantum graphs during inverse training, we are able to conceptualize the learned strategies applied by the neural network. We probe the network's rationale further by inverse training on the intermediate layers of the network. We find that the network learns to recognize simple features in the first layers and then builds up more complicated structures in later layers. Altogether, we synthesize a complete picture of what the trained neural network sees. We, therefore, posit that our tool may aid the design of more interpretable and reliable computer-inspired schemes to design quantum optics experiments.

2. Methodology

2.1. Graphs and quantum experiments

As developed in [24, 25, 35–37], we may represent quantum optical experiments in terms of colored, weighted, undirected multigraphs. This representation can be extended to integrated photonics [38–41] and entanglement by path identity [26, 42, 43]. The vertices of the graph represent photon paths to detectors, whereas edges between any two vertices, a and b, indicate correlation between two photon paths. We may assign an amplitude to them by introducing edge weights $\omega_{a,b}$, and we may assign the photons' internal mode number through different edge colorings. Each vertex inherits a color from the colored edge, defining the state of each photon.

Here, we consider graph representations of four-qubit, two-dimensional experiments dealing with state creation. Specifically, we consider graphs with vertices $V = \{0, 1, 2, 3\}$ and mode numbers 0 and 1 which we represent by coloring the edges blue and red respectively. Each graph, therefore, consists of 24 possible edges with real-valued edge weights between 1 and -1. We may determine the particular quantum state $|\Phi(\omega)\rangle$, where $\Phi(\omega)$ is the graph's weight function defined according to equation (2) in [25]. Specifically, we write

$$\Phi(\omega) = \sum_m \frac{1}{m!} \left(\sum_{e \in E(G)} \omega(e) x^\dagger(e) y^\dagger(e) + \text{h.c.} \right)^m , \tag{1}$$

where $E(G)$ is the set of edges of the graph G, $x^\dagger(e)$ and $y^\dagger(e)$ are creation operators of photons, which are represented as vertices x and y of edge e, and $h.c.$ is the hermitian conjugate, which includes annihilation terms. The quantum state can then be realized physically by applying the weight function to the vacuum state as $|\Phi(\omega)\rangle = \Phi(\omega)|\text{vacuum}\rangle$. On the whole, the neural network finds a way to decompose the quantum state into PMs of a graph. This is useful because we can experimentally implement arbitrary graphs in the laboratory, and the quantum state emerges as the coherent superposition of PMs.

We condition the creation of each term in the state on subsets of edges which contains every vertex in the graph exactly once, otherwise known as the PMs of the graph. This appears in $\Phi(\omega)$ as $m = 2$ order terms

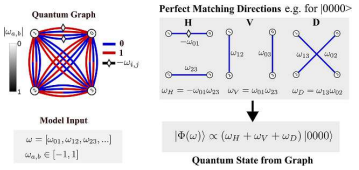

Figure 1. Brief overview of quantum graphs. In this work, we consider *complete* graph representations of two-dimensional, quadripartite quantum graphs. We let $\omega_{a,b}$ denote the weight of the edge connecting vertex a to vertex b. The weight's magnitude is indicated by the transparency of the edge and the presence of a diamond signifies a negative edge weight. The creation of every possible ket in the joint Hilbert space $\mathcal{H}$ is conditioned on the coherent superposition of the three possible types of perfect matchings (PMs), which are distinguished in terms of their direction. By considering the superposition of every PM, we obtain the quantum graph's state $|\Phi(\omega)\rangle$.

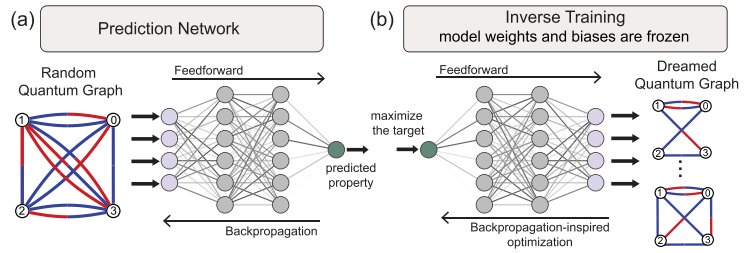

Figure 2. Quantum graph deep dreaming. (a) The weights and biases of a feed-forward neural network are continually updated during training to predict a property such as fidelity of a given input random quantum experiment represented by a graph. (b) In the deep dreaming process, the weights and biases of the network are frozen, and an initial input graph is fed onto the input layer of the neural network. The weights of an initial input graph are updated iteratively to maximize the activation of the output neuron of the feed-forward network, which gives the network's prediction on the aforementioned property. We expect that, when we feed the dreamed graph at the end of the process onto the neural network, the output activation is maximized.

and, physically, corresponds to conditioning one photon on each detector, a common technique in quantum optics. For each term, we can define three possible PMs, each distinguished by their 'directionality', which we show in figure 1. We obtain the amplitude of the term through the sum of weights of the three PMs, which are themselves determined by the product of edge weights. We permit multiple edges between the vertices to allow for the the superposition of different states. Applying this procedure for every possible ket in the joint Hilbert space $\mathcal{H} = \mathbb{H}_2 \otimes \mathbb{H}_2 \otimes \mathbb{H}_2 \otimes \mathbb{H}_2$, we may obtain the state $|\Phi(\omega)\rangle$. Larger, D-dimensional quantum systems consisting of n photons can be represented as a weighted graph with up to $D^2 \times \frac{n(n-1)}{2}$ edges.

2.2. Training

Figure 2 illustrates the basic workflow behind the dreaming process. A feed-forward neural network is first trained on the edge weights ω of a complete, quadripartite, two-dimensional quantum graph in order to make predictions on certain properties of the corresponding quantum state $|\Phi(\omega)\rangle$. We randomly initialize ω over a uniform distribution $[-1, 1]$. The neural network's own weights and biases are optimized for this task via mini-batch gradient descent and the mean squared error (MSE) loss function.

We consider the state fidelity $|\langle\Phi(\omega)||\psi\rangle|^2$ with respect to two well-known classes of multipartite entangled states within the joint Hilbert space $\mathcal{H}$. First, the Greenberger–Horne–Zeillinger (GHZ) State [44], $|\psi\rangle = |\mathrm{GHZ}\rangle$, where

$$|\mathrm{GHZ}\rangle = \frac{1}{\sqrt{2}}\left(|0000\rangle + |1111\rangle\right), \tag{2}$$

and, second, the W-state [45], $|\psi\rangle = |W\rangle$, where

$$|W\rangle = \frac{1}{\sqrt{2}}\left(|1000\rangle + |0100\rangle + |0010\rangle + |0001\rangle\right). \tag{3}$$

In addition, we also consider a measure of quantum state entanglement resulting from a graph—the concurrence [46]. Let A_1, A_2, A_3, A_4 each denote the subsystems of the joint quadripartite Hilbert space to which $|\Phi(\omega)\rangle$ is defined. Then assuming the pure state $\rho = |\Phi(\omega)\rangle\langle\Phi(\omega)|$, we may write

$$C(\rho) = \sum_{\mathcal{M}} C_{\mathcal{M}}(\rho) = \sum_{\mathcal{M}} \sqrt{2\left(1 - \mathrm{tr}\left(\rho_{\mathcal{M}}^2\right)\right)} \tag{4}$$

where $C(\rho)$ is the concurrence, $\mathcal{M}$ refers to a bipartitioning or 'split' of the subsystems into two disjoint subsystems (for example, $|0000\rangle = |0\rangle \otimes |000\rangle$ refers to a bipartitioning of subsystems into sets $\{A_1\}$ and $\{A_2, A_3, A_4\}$) and $\mathrm{tr}(\rho_{\mathcal{M}}^2)$ is the reduced density matrix obtained by tracing out $\mathcal{M}$. Each term in the sum of equation (4), then, corresponds to a different bipartitioning of subsystems. In this work, we train our networks to make predictions on the mean of $\mathrm{tr}(\rho_{\mathcal{M}}^2)$ across all biparitions $\mathcal{M}$, $\overline{\mathrm{tr}(\rho_{\mathcal{M}}^2)}$. Furthermore, for all cases considered, the network is trained on examples with a property value below a threshold of 0.5 to ensure that the network is not memorizing the best solutions in each case. This threshold remains fixed for cases involving the GHZ- and W- state fidelities and the value of $\overline{\mathrm{tr}(\rho_{\mathcal{M}}^2)}$. During this generation of the training data set, if examples are beyond the threshold, they are rejected.

Once convergence in the training has been achieved, we then execute the deep dreaming protocol to extract insights on what the neural network has learned. Given an arbitrary input graph, we select a neuron in the trained neural network. Then, we maximize the neuron's activation by updating the input graph via gradient ascent. In this stage, the weights and biases of the neural network are frozen, and we instead optimize for the edge weights of the input graph. During each iteration of the process, we calculate the loss—here, the negative of the network's activation—by evaluating the network's prediction with the intermediate, input graph. At the end of the process, the graph mutates into a configureation which most excites the neuron. However, this may not entirely represent all that the neuron over-interprets from the input graph, as it has been shown in [47] that individual neurons can be trained to recognize various possible features of the input. Therefore, to uncover all that the neuron sees, we repeat this procedure multiple times with different input quantum graphs.

3. Results

3.1. Dreaming on the output layer

Towards attaining a general idea of what the neural network has learned about select properties for the quantum state $|\Phi(\omega)\rangle$, we first apply the deep dreaming approach on the output layer. Figure 3(a) illustrates the mutation of an input graph by applying the deep dreaming approach on a $[400^3,10]$ (three hidden layers of 400 neurons, one hidden layer of 10 neurons) neural network, which has been trained to predict either the GHZ-state or the W-state fidelity. We also apply this approach on a $[800^7]$ neural network architecture, which has been trained to predict the mean value of $\mathrm{Tr}(\rho_{\mathcal{M}}^2)$. While dreaming, we task our network to find configureations which maximizes the property value. It should be stressed that, in particular, the optimal configureation that maximizes $\overline{\mathrm{tr}(\rho_{\mathcal{M}}^2)}$ minimizes the concurrence; we, therefore, anticipate the dreamed graph to correspond to a maximally separable state. Conversely, tasking the network to minimize $\overline{\mathrm{tr}(\rho_{\mathcal{M}}^2)}$ will influence it to dream graphs that realize maximally entangled states.

We obtain $|\Phi(\omega)\rangle$ from the reconstructed, mutated graph and recompute its true property value in each step. In all cases, we find that the graph evolves steadily towards the maximum property value. We repeat this procedure for 1000 different quantum graphs and plot the distribution of each graphs' initial versus dreamed fidelities in figure 3(b). In all three cases, we observe that the network consistently finds distinct examples with a property value outside the initial distribution's upper bounds. This demonstrates our approach's potential to discover novel quantum graphs which optimizes a specific quantum state property. The distribution of dreamed values of $\overline{\mathrm{tr}(\rho_{\mathcal{M}}^2)}$ is much more narrow than the dream distribution of either the GHZ- or W- state fidelities. This is due to the fact that a wide variety of states demonstrates separability across various $\mathcal{M}$ and, therefore, possess a high value of $\overline{\mathrm{tr}(\rho_{\mathcal{M}}^2)}$, whereas the only states which maximizes the GHZ/W state fidelities are the GHZ/W states themselves. Furthermore, the activation vastly exceeds the usual upper bounds of the property being predicted. This is due to the fact that, as the input graph mutates, the edge weights increase without bound and become unnormalized. Thus, in the end, we compute the normalization of all quantum states.

The intermediate steps of the dreaming process allow us to discern what strategies the neural networks are applying to a given optimization task. In figure 4, we summarize the evolution of different initial graphs during inverse training for different targets. In figure 4(a), we observe that the neural network tries to activate the $|0000\rangle$ and $|1111\rangle$ states either by creating PM of these terms in unused directions—the input graph had no PM in that direction previously—or by completing them with the assistance of an existing PM

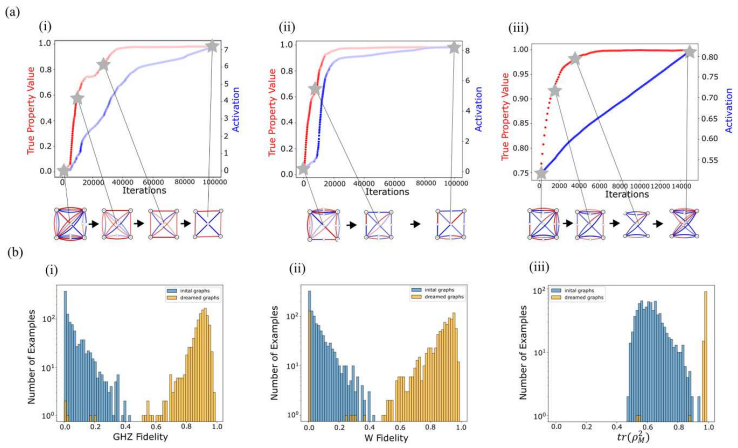

Figure 3. Dreaming results for on the output layer of different neural network architectures. (a) Plot of the evolution of an arbitrary input graph's activation, shown in blue, and true property value, shown in red, when we task the network to discover quantum graphs satisfying different optimization tasks. Specifically, we task the $[400^3, 10]$ network to find quantum graphs maximizing (i) the GHZ- state and (ii) W-state fidelities, and task the $[800^7]$ network to find graphs maximizing (iii) $\mathrm{tr}(\overline{\rho^2_{\mathcal{M}}})$. For each case, we show the intermediate steps of the input graphs' evolution to its dreamed counterpart and only show edges whose weights are above a threshold of 0.4. We, therefore, illustrate steps of the quantum graphs' evolution throughout each dreaming process. These intermediate steps reveal that, in inverse-training, edges of PMs which do not positively contribute to the target property are mitigated. (b) Distribution of initial vs. dreamed fidelities with respect to (i) the GHZ state and (ii) the W-state, as well as (iii) the mean value of $\mathrm{tr}(\rho^2_{\mathcal{M}})$. We observe that most dreamed examples exceed the upper bound of the original dataset, attesting to our tool's ability to find quantum graphs that are novel to the original dataset.

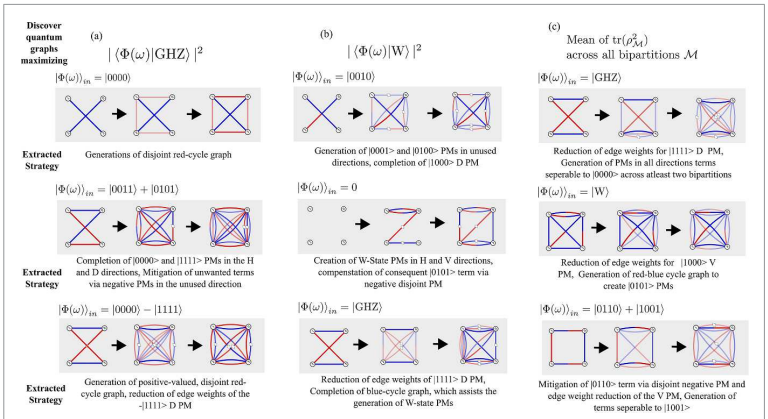

Figure 4. Extracted strategies from the evolution of certain states when dreaming on the output layer of the neural network. We discern the strategies employed by the inverse training routine when applied to a network tasked to optimize (a) the GHZ-State Fidelity, (b) the W-State Fidelity, and (c) the mean value of $\mathrm{tr}(\rho^2_{\mathcal{M}})$ by considering several initialisations for each case. For each graph, we only show edges with weights greater than 0.3. We find that the network attempts to construct perfect matchings (PMs) of terms which positively contribute to the property value and whose weights add up to 1. Conversely, we find that the network eliminates unwanted terms by either directly reducing the edge weights of the PM corresponding to that term, or by introducing negative, disjoint perfect matchings of that term. For (c), we observe that the network 'selects' a term in the initial state to be minimized, then creates terms that are separable across two or more bipartitions with respect to the remaining states.

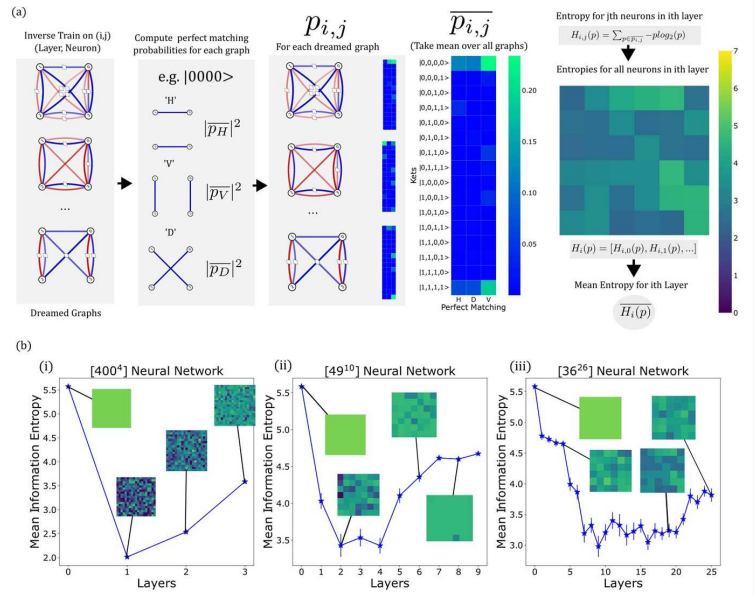

Figure 5. Information entropy throughout each different neural network architecture. (a) Workflow behind computing the mean information entropy for each layer of the trained neural network. We dream with multiple input graphs on each neuron in the neural network. To account for the diversity of structures that a neuron is interested in seeing, we compute the mean probability amplitudes for every possible perfect matching corresponding to each ket. We thereby observe the overall graph, which the neuron sees best. We may then compute the information entropy of each neuron, $H_{i,j}(p)$, and the mean information entropy of the layer, $\overline{H_{i,j}(p)}$. This gives us a measure of the complexity of structures seen by the neural network. As conveyed in the different $p_{i,j}$ for each dreamed graph, we note the variety of structures which the network over-interprets; this illustrates the multifactedness of the neurons. (b) Mean information entropy plots for the (i) $[400^4]$ (ii) $[49^{10}]$ and (iii) $[36^{26}]$ neural network architectures. A general trend that we may discern in all three cases is that the mean information entropy converges to a minimum in the lower layers and then gradually increases as we go deeper. We may attribute this to the intuition that the network initially learns to recognize simpler structures, then learns increasingly complicated ones as we go deeper within the network.

in some direction, as is seen in particular with the $|\Phi(\omega)\rangle = |0011\rangle + |0101\rangle$ initialization. The dreaming process creates these PMs such that their weights add up to 1. In circumstances where the initial graph starts with unwanted terms, or when the network unavoidably creates these terms while dreaming, the network attempts to eliminate them either by directly lowering the edge weights' magnitudes or by introducing negative weight PMs in different directions. We see this trend continue when the network is tasked with maximizing the W-state fidelity, as shown in figure 4(b), albeit instead in favouring the activation of the $|1000\rangle, |0100\rangle, |0010\rangle$, and $|0001\rangle$ states. In figure 4(c), the network attempts to maximize the separability of the initial, maximally entangled state by first eliminating one term from the initial state via edge-weight minimization or through negative PMs, then creating PMs of additional terms which are separable with respect to the intermediate graph state across two or more bipartitions. Through our deep dreaming approach, we have shown that the network learns about creating states through the graph representation in order to consistently achieve optimal values for select properties of the quantum state. We remark that, for each state property, the network was able to ascertain the configureations which maximizes them while only seeing configureations having property values below 0.50. This strongly suggests that the network is achieving its tasks from physical insights, rather than by memorizing the best examples.

3.2. Interpretability of neural network structure

We apply the deep dreaming approach on the neurons of its hidden layers to gain insight into the neural network's internal model, which generalizes well beyond the training data. We summarize the insights that we extract through our routine in figure 5. To showcase the universality of our approach, we consider several

different neural network architectures—the $[400^4]$, $[49^{10}]$ and $[36^{26}]$ networks—that have each been trained to predict the GHZ-state fidelity. For each network, we dream on the ith neuron in the jth hidden layer with 20 input graphs to best capture all of the possible structures exciting the neuron.

We take particular interest in how the complexity of the dreamed graphs evolves with the network depth. We obtain the greatest amount of information about our quantum graphs by considering all of the different ways, as seen through the graphs' PMs, that a ket is realized. We, therefore, attribute to each dreamed graph a 3×16 array, $p_{i,j}$, consisting of the probabilities of all possible PMs; through this, we gain insight into the state created by the graph, as well as all PM directions being used to that purpose. As we go deeper into the neural network, we observe that the dreamed graphs activate a greater number of PM directions and kets, which reflects the increasing complexity of structures the neural network has learned to recognize. We also verify the multifaceted nature of the neurons: different input graphs are observed to result in dreamed graphs that recreate different input states. As we see in the third inset of figure 5(a), the neuron may over-interpret parts of the graph that best creates the $|0000\rangle$ term, or it may either over-interpret different possible PM directions for $|0000\rangle$, or parts of the graph which instead realize the $|1111\rangle$ term.

We may quantify the complexity of structures recognized throughout the network with the information entropy $H_{i,j}$. We take the mean value of $p_{i,j}$ across all of the dreamed graphs, then use it to compute $H_{i,j}$ through the procedure outlined in appendix C. Repeating this procedure across all hidden layer neurons, we may then determine the average entropy observed across the jth layer, which gives us a general metric of the complexity of structures being recognized. We plot the trend of $\overline{H_{i,j}}$ observed across all three neural network architectures in figure 5(b). Intuitively, we expect that a deep neural network first learns to recognize simple structures, then more abstract features with network depth. Indeed, we observe consistently that, from an initial peak, the information entropy drops to its lowest values at the earlier layers, before gradually increasing near the end of the neural network. This certifies the universal assertion that the network identifies simple features of the input graph, such as edges that form one or two PMs to states, before forming more complicated graphical structures in the deeper layers that features a greater set of PMs.

4. Outlook

In this article, we showcase preliminary results for adapting the deep dreaming approach to quantum optical graphs for deep neural networks on different target quantities. We apply our routine to ascertain the strategies employed by the neural network on its predictive task by dreaming on the output layer and throughout the network. Crucially, we demonstrate that the trained neural network builds a non-trivial model of the quantum state properties produced by a quantum experiment, and we find that the deep dreaming approach does remarkably well in finding novel examples outside of the initial dataset. Lastly, in applying our approach to the hidden layers of the neural network, we find that the network gradually learns to recognize increasingly complicated structures, and that the individual neurons are multifaceted in the possible structures that excites them. In future work, further transparency of the learned representations can be possibly attained by applying regularization techniques such as α-norm [48], jitter [30], or by dreaming on the mean of a set of input graphs [47] to converge towards more interpretable solutions. It will also be interesting to see if we can obtain further insights by directly modifying the weights and biases of the neural network. Above all, we may also apply these tools to larger graphs with more dimensions and explore different applications beyond state creation, such as Quantum Measurements and Quantum Communication.

Thanks to their relative simplicity, the quadripartite graphs have been a good testing case for our inception approach, and the knowledge we extract from them can be used in other systems. Larger graphs and new targets will provide a novel and deeper understanding of quantum optics experiments as well as inspire new research. We foresee that our approach can be used to extend frameworks for automated setup design [4, 19, 25] as well as in generative molecular algorithms [32, 49] which adapt a surrogate neural network model. Through our approach, we can better decipher what these frameworks have learned about the underlying science, and understand the intermediate strategies taken towards a target configureation.

Data availability statement

The data that support the findings of this study are openly available at the following URL/DOI: https://github.com/artificial-scientist-lab/deepGraphDreaming.

Acknowledgments

T J and E K acknowledge the support of the Canada Research Chairs (CRC) and Max Planck-University of Ottawa Centre for Extreme and Quantum Photonics.

Appendix A

A.1. Training details

We generate 20 million input-output pairs using the digital discovery framework PyTheus [25]. Each input is a one-dimensional array consisting of the 24 real-valued edge weights which corresponds to the quantum graph, and the output is the property value of the graph's corresponding state, $|\Phi(\omega)\rangle$. The network is then forward-trained on these examples with a mini-batch size of 5000 and a 95:5 train-test split. We utilize a learning rate scheduler that is initially set 1×10^{-3} (1×10^{-5} for the $[36^{26}]$ training architecture) and is gradually decreased in factors of 0.95 if, after every 25 training epochs, the test MSE does not change significantly. The network is run until convergence in the test MSE is maintained for over 400 training epochs. Table A1 lists the network architectures considered and the corresponding training results for each network. Between the networks' hidden layers, We employ the ReLU nonlinear activation function for all of our architectures except for the $[36^{26}]$ network, in which the ELU activation function with $\alpha = 0.1$ was used. The networks were encoded using PyTorch [50], and we employ the Adam optimizer [51] for both the forward and inverse training steps. A hyperparameter search was carried out on the number of neurons, N, in the generic neural network architecture $[N^4]$ towards predicting the GHZ-State fidelity. We considered architectures with $N = 10, 25, 40, 100, 200,$ and 400. The hyperparameter search stopped once satisfactory improvements in the test MSE with respect to the simplest model considered were attained, which was achieved with $N = 400$ neurons. We found this architecture to be satisfactory for the purposes of predicting the W-State Fidelity, but not the value of $\mathrm{tr}(\overline{\rho^2_{\mathcal{A}}})$, which prompted us to consider instead the $[800^7]$ neural network. Table A2 showcases the results of our hyperparameter search.

Table A1. Training Details of all Neural Network Architectures featured in this work. Each architecture is listed in the format $[N_1, N_2, \ldots N_l]$, where N_i refers to the number of neurons of the ith hidden layer.

NN Architecture	Test MSE	Training Epochs
$[400^4]$	2.48×10^{-6}	2550
$[800^7]$	2.95×10^{-6}	2300
$[49^{10}]$	3.60×10^{-4}	2300
$[36^{26}]$	6.24×10^{-4}	2700
	4.12×10^{-6} (GHZ)	
$[400^3, 10]$	6.89×10^{-6} (W)	4200 (Both)

Table A2. Hyperparameter search on the number of neurons, N, in the neural network architecture $[N^4]$ towards predicting GHZ-state fidelity. We show the minimal test MSE achieved after convergence.

NN Architecture	Test MSE
$[10^4]$	2.63×10^{-4}
$[25^4]$	8.33×10^{-4}
$[40^4]$	3.97×10^{-4}
$[100^4]$	7.02×10^{-5}
$[200^4]$	5.24×10^{-6}
$[300^4]$	2.47×10^{-6}
	1.53×10^{-6} (GHZ)
$[400^4]$	5.98×10^{-4} (Concurrence)

We perform inverse training on the jth neuron in layer i each of our trained networks' architecture by employing gradient ascent on random input graphs towards maximizing the neuron's activations. This is done by transferring all of the trained networks' parameters up to and including the $(i-1)$th layer. The ith layer, which now forms the output layer of this intermediate network, consists solely of neuron j. We then sample randomly from a dataset consisting of 1 million input graphs and perform the dreaming routine for

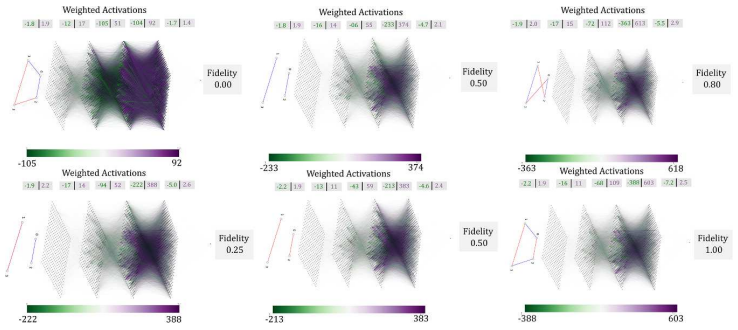

Figure A1. Plots of the *globally normalized* weighted activation for the $[400^4]$ neural network architectures when trained to predict the fidelity of the GHZ state. The plots are computed by taking the product of the trained neural network weights with the activations of the network when asked to predict $|\langle\Phi(\omega)\rangle\text{GHZ}|^2$ for various states $|\Phi(\omega)\rangle$. Towards best visualizing each network, we filter out edges whose weighted activations are below a threshold of 0.05. We find that different PM directions and colourings change which neurons are activated in the intermediate layers, whereas the corresponding state's fidelity changes the magnitude of activations observed throughout the network. The different kinds of neuron activation patterns give us insight into how the neural network conceives its prediction.

100 000 iterations and a fixed learning rate of 1×10^{-4} when the network is tasked to optimize the GHZ- and W- state fidelities. For a single input graph, we observe inverse training times of approximately 5 min (0.003 seconds per iteration) for fidelity optimization tasks and 4 min (0.016 seconds per iteration) for concurrence minimization. We therefore dream with 15 000 iterations to compensate for the increased complexity of the architecture. Inverse training was done on an AMD Ryzen 5 4500U @ 2.38 GHZ CPU. It is possible to shorten the inverse training time by increasing the learning rate and implementing an early stopping criterion conditioned on the property value. For example, by increasing the learning rate to 1×10^{-3} and by stopping the dreaming process if, after 1000 iterations, the test MSE does not experience a change greater than 1×10^{-7}, the task of dreaming towards maximal GHZ- state fidelities finished after roughly 5000 iterations.

Appendix B. Neural network activation plots

Figure A1 displays the weighted activation patterns for the trained $[400^4]$ neural network architecture when tasked to make predictions on quantum graphs over a range of fidelity values. We observe that the activation patterns change depending on the kinds of PMs featured by the input graph. In tandem with our deep dreaming approach, we envision that we can reverse engineer what the neural network is observing in its computation of the GHZ-state fidelity by examining the activation patterns and through knowledge of what each individual neuron is precisely seeing.

Appendix C. Quantifying the quantum graph complexity

The complete Hilbert space $\mathcal{H} = \mathbb{H}_2 \otimes \mathbb{H}_2 \otimes \mathbb{H}_2 \otimes \mathbb{H}_2$ on which $|\Phi(\omega)\rangle$ is defined consists of 16 possible states. In the formulation of quantum graphs estabilshed in section 2.1, the probability amplitude of any quantum state $|\psi\rangle \in \mathcal{H}$ can be obtained via the weights of the three possible PMs which realize the state. The weights for each PM are obtained as follows,

$$p_{|\psi\rangle} = p_H^{|\psi\rangle} + p_V^{|\psi\rangle} + p_D^{|\psi\rangle} \tag{C1}$$

where

$$p_H^{|\psi\rangle} = |\omega_{01}\omega_{23}|^2 \tag{C2}$$

$$p_V^{|\psi\rangle} = |\omega_{03}\omega_{12}|^2 \tag{C3}$$

$$p_D^{|\psi\rangle} = |\omega_{02}\omega_{13}|^2 \tag{C4}$$

and $0 \leqslant |\omega_{a,b}|^2 \leqslant 1$, $a, b \in \{0, 1, 2, 3\}$ denote the weight of an edge with vertices a,b for the endpoint.

Repeating this procedure for every ket in $\mathcal{H}$, we obtain a 3×16 array of probabilities $p_{i,j}$ for the ith neuron of the jth hidden layer. We may think of the graphs' complexity in terms of the sum of probabilities that different possible events—here, the PMs corresponding to each quantum state—may occur. The overall complexity of structures observed by our neuron can, therefore, be quantified by calculating $\overline{p_{i,j}}$ over all of our representations, and computing the information entropy.

$$H_{i,j} = \sum_{p \in \overline{p_{i,j}}} -p \log_2(p) \tag{C5}$$

We may iterate with this procedure across all of the neurons in the jth layer, yielding an array of information entropies out of which the mean information entropy of the layer, $\overline{H_j}$, may be obtained. This gives us an overall measure of the complexity of structures being observed at every point in the neural network.

ORCID iDs

Tareq Jaouni https://orcid.org/0009-0006-5661-2403
Carlos Ruiz-Gonzalez https://orcid.org/0000-0003-0545-360X
Ebrahim Karimi https://orcid.org/0000-0002-8168-7304

References

[1] Dawid A, Arnold J, Requena B, Gresch A, Płodzień M, Donatella K, Nicoli K A, Stornati P, Koch R and Büttner M 2022 Modern applications of machine learning in quantum sciences (arXiv:2204.04198)
[2] Krenn M, Landgraf J, Foesel T and Marquardt F 2023 Artificial intelligence and machine learning for quantum technologies *Phys. Rev.* A **107** 010101
[3] Carleo G, Cirac I, Cranmer K, Daudet L, Schuld M, Tishby N, Vogt-Maranto L and Zdeborová L 2019 Machine learning and the physical sciences *Rev. Mod. Phys.* **91** 045002
[4] Krenn M *et al* 2022 On scientific understanding with artificial intelligence *Nat. Rev. Phys.* **4** 761
[5] Doran D, Schulz S and Besold T R 2017 *What Does Explainable ai Really Mean? A New Conceptualization of Perspectives* (arXiv:1710.00794)
[6] Tjoa E and Guan C 2021 A survey on explainable artificial intelligence (XAI):towards medical XAI *IEEE Trans. Neural Netw. Learn. Syst.* **32** 4793
[7] Burkart N and Huber M F 2021 A survey on the explainability of supervised machine learning *J. Artif. Intell. Res.* **70** 245
[8] Samek W, Wiegand T and Müller K-R 2017 Explainable artificial intelligence: understanding, visualizing and interpreting deep learning models (arXiv:2204.04198)
[9] Iten R, Metger T, Wilming H, del Rio L and Renner R 2020 Discovering physical concepts with neural networks *Phys. Rev. Lett.* **124** 010508
[10] Wetzel S J, Melko R G, Scott J, Panju M and Ganesh V 2020 Discovering symmetry invariants and conserved quantities by interpreting siamese neural networks *Phys. Rev. Res.* **2** 033499
[11] Dawid A, Huembeli P, Tomza M, Lewenstein M and Dauphin A 2021 Hessian-based toolbox for reliable and interpretable machine learning in physics *Mach. Learn. Sci. Technol.* **3** 015002
[12] Dawid A, Huembeli P, Tomza M, Lewenstein M and Dauphin A 2020 Phase detection with neural networks: interpreting the black box *New J. Phys.* **22** 115001
[13] Käming N, Dawid A, Kottmann K, Lewenstein M, Sengstock K, Dauphin A and Weitenberg C 2021 Unsupervised machine learning of topological phase transitions from experimental data *Mach. Learn.: Sci. Technol.* **2** 035037
[14] Wetzel S J and Scherzer M 2017 Machine learning of explicit order parameters: from the ising model to su(2) lattice gauge theory *Phys. Rev.* B **96** 184410
[15] Rocchetto A, Grant E, Strelchuk S, Carleo G and Severini S 2018 Learning hard quantum distributions with variational autoencoders *npj Quantum Inf.* **4** 28
[16] Flam-Shepherd D, Wu T C, Gu X, Cervera-Lierta A, Krenn M and Aspuru-Guzik A 2022 Learning interpretable representations of entanglement in quantum optics experiments using deep generative models *Nat. Mach. Intell.* **4** 544
[17] Frohnert F and van Nieuwenburg E 2024 Explainable representation learning of small quantum states *Mach. Learn.: Sci. Technol.* **5** 015001
[18] Krenn M, Erhard M and Zeilinger A 2020 Computer-inspired quantum experiments *Nat. Rev. Phys.* **2** 649
[19] Krenn M, Malik M, Fickler R, Lapkiewicz R and Zeilinger A 2016 Automated search for new quantum experiments *Phys. Rev. Lett.* **116** 090405
[20] Nichols R, Mineh L, Rubio J, Matthews J C F and Knott P A 2019 Designing quantum experiments with a genetic algorithm *Quantum Sci. Technol.* **4** 045012
[21] O'Driscoll L, Nichols R and Knott P A 2019 A hybrid machine learning algorithm for designing quantum experiments *Quantum Mach. Intell.* **1** 5
[22] Valcarce X, Sekatski P, Gouzien E, Melnikov A and Sangouard N 2023 Automated design of quantum-optical experiments for device-independent quantum key distribution *Phys. Rev.* A **107** 062607
[23] Arrazola J M, Bromley T R, Izaac J, Myers C R, Brádler K and Killoran N 2019 Machine learning method for state preparation and gate synthesis on photonic quantum computers *Quantum Sci. Technol.* **4** 024004
[24] Krenn M, Kottmann J S, Tischler N and Aspuru-Guzik A 2021 Conceptual understanding through efficient automated design of quantum optical experiments *Phys. Rev.* X **11** 031044
[25] Ruiz-Gonzalez C, Arlt S, Petermann J, Sayyad S, Jaouni T, Karimi E, Tischler N, Gu X and Krenn M 2023 Digital discovery of 100 diverse quantum experiments with PyTheus *Quantum* **7** 1204
[26] Krenn M, Hochrainer A, Lahiri M and Zeilinger A 2017 Entanglement by path identity *Phys. Rev. Lett.* **118** 080401

[27] Gao X, Erhard M, Zeilinger A and Krenn M 2020 Computer-inspired concept for high-dimensional multipartite quantum gates *Phys. Rev. Lett.* **125** 050501
[28] Arlt S, Ruiz-Gonzalez C and Krenn M 2022 Digital discovery of a scientific concept at the core of experimental quantum optics (arXiv:2210.09981)
[29] Jaouni T, Gao X, Arlt S, Krenn M and Karimi E 2023 Experimental solutions to the high-dimensional mean king's problem *Opt. Quantum* **1** 49–54
[30] Mordvintsev A, Olah C and Tyka M 2015 Inceptionism: going deeper into neural networks (available at: https://ai.googleblog.com/2015/06/inceptionism-going-deeper-into-neural.html)
[31] Lifshitz R 2022 Quantum deep dreaming: a novel approach for quantum circuit design (arXiv:2211.04343)
[32] Shen C, Krenn M, Eppel S and Aspuru-Guzik A 2021 Deep molecular dreaming: inverse machine learning for de-novo molecular design and interpretability with surjective representations *Mach. Learn.: Sci. Technol.* **2** 03LT02
[33] Schindler F, Regnault N and Neupert T 2017 Probing many-body localization with neural networks *Phys. Rev.* B **95** 245134
[34] Seif A, Hafezi M and Jarzynski C 2021 Machine learning the thermodynamic arrow of time *Nat. Phys.* **17** 105
[35] Krenn M, Gu X and Zeilinger A 2017b Quantum experiments and graphs: multiparty states as coherent superpositions of perfect matchings *Phys. Rev. Lett.* **119** 240403
[36] Gu X, Erhard M, Zeilinger A and Krenn M 2019a Quantum experiments and graphs II: quantum interference, computation and state generation *Proc. Natl Acad. Sci.* **116** 4147
[37] Gu X, Chen L, Zeilinger A and Krenn M 2019b Quantum experiments and graphs. III. High-dimensional and multiparticle entanglement *Phys. Rev.* A **99** 032338
[38] Ding Y, Llewellyn D, Faruque I, Paesani S, Bacco D, Rottwitt K, Laing A, Thompson M, Wang J and Oxenløwe L K 2020 Integrated quantum photonics on silicon platform *Optical Fiber Communication Conf. (OFC) 2020* (Optica Publishing Group) p W4C.6
[39] Feng L-T, Guo G-C and Ren X-F 2020 Progress on integrated quantum photonic sources with silicon *Adv. Quantum Technol.* **3** 1900058
[40] Pelucchi E *et al* 2022 The potential and global outlook of integrated photonics for quantum technologies *Nat. Rev. Phys.* **4** 194
[41] Bao J, Fu Z, Pramanik T, Mao J, Chi Y, Cao Y, Zhai C, Mao Y, Dai T and Chen X 2023 Very-large-scale integrated quantum graph photonics *Nat. Photon.* **1** 1204
[42] Qian K, Wang K, Chen L, Hou Z, Krenn M, Zhu S and Ma X-S 2023 Multiphoton non-local quantum interference controlled by an undetected photon *Nat. Commun.* **14** 1480
[43] Feng L-T, Zhang M, Liu D, Cheng Y-J, Guo G-P, Dai D-X, Guo G-C, Krenn M and Ren X-F 2023 On-chip quantum interference between the origins of a multi-photon state *Optica* **10** 105
[44] Greenberger D M, Horne M A and Zeilinger A 1989 Going beyond bell's theorem *Bell's Theorem, Quantum Theory and Conceptions of the Universe* (Springer) pp 69–72
[45] Cabello A 2002 Bell's theorem with and without inequalities for the three-qubit Greenberger-Horne-Zeilinger and W states *Phys. Rev.* A **65** 032108
[46] Wootters W K 2001 Entanglement of formation and concurrence *Quantum Inf. Comput.* **1** 27
[47] Nguyen A, Yosinski J and Clune J 2016 Multifaceted feature visualization: uncovering the different types of features learned by each neuron in deep neural networks (arXiv:1602.03616)
[48] Simonyan K, Vedaldi A, and Zisserman A 2013 Deep inside convolutional networks: visualising image classification models and saliency maps (arXiv:1312.6034)
[49] Hoogeboom E, Satorras V G, Vignac C and Welling M 2022 Equivariant diffusion for molecule generation in 3d *Int. Conf. on Machine Learning* (PMLR) pp 8867–87
[50] Paszke A, Gross S, Massa F, Lerer A, Bradbury J, Chanan G, Killeen T, Lin Z, Gimelshein N and Antiga L *et al* 2019 Pytorch: an imperative style, high-performance deep learning library *Advances in Neural Information Processing Systems* vol 32
[51] Kingma D P and Ba J 2014 Adam: a method for stochastic optimization (arXiv:1412.6980)

Chapter 4

High-Dimensional Quantum Communication

This chapter is based on the following publication.

Jaouni, Tareq, Xiaoqin Gao, Sören Arlt, Mario Krenn, and Ebrahim Karimi. "Experimental Solutions to the High Dimensional Mean King's Problem." *Optica Quantum 1 (2)* (2023): 49 - 54

DOI: https://doi.org/10.1364/OPTICAQ.502451

4.1 Overview

First introduced by Vaidman, Aharanov, and Albert [39], the Mean King's Problem tasks one communicating party, Alice, with retrodicting a projective measurement made by the Mean King. At its most fundamental level, the protocol is outlined in the following matter

1. Alice prepares a quantum system $|\psi\rangle$ using any mode of the particle (e.g. silver atom) in any way she chooses.
2. the King receives Alice's state and makes a PVM on $|\psi\rangle$ in a basis of his choosing specified by the Heisenberg-Weyl operators. Ideally, this leaves the state in an eigenstate $|m\rangle_k$ with probability $\frac{1}{D}$

3. Alice retrieves her state back from the King and performs one more experiment on $|m\rangle_k$. Alice must then guess correctly that the Mean King has measured the eigenstate $|m\rangle_k$, else she suffers a cruel fate at His hands.

The original authors revealed that Alice can always escape the Mean King's cruelty using the following trick: Alice entangles onto her system an ancillary qubit, thereby realizing the generalized bell state $|B_{0,0}\rangle$. She sends one qubit to the King, while keeping her ancilla to herself. Having received the measured qubit from the King, Alice then performs a joint measurement in the basis of the specialized Vaidman-Albert-Aharanov (VAA) states. With knowledge of the King's measurement basis, Alice can use the results of her joint measurement to retrodict with certainty the King's measurement outcome.

Though initially posed as a two-dimensional problem, wherein Alice is tasked to divine the Mean King's measurement on a spin-1/2 particle, the MKP has since been generalized to higher dimensions [54, 55, 56], and harder variants to the problem have also emerged [57, 58]. There also exists experimental proposals to the two-dimensional case using single photons in two physical degrees of freedom [58, 59]. However, to date, there does not yet exist experimental proposals for those higher-dimensional solutions. We may attribute this to the non-triviality of Alice's joint measurement in the VAA state basis. In the sections to follow, we aim to develop the solution to the Mean King's Problem for any dimension where D is prime. We describe in detail how Alice can leverage the esoteric properties of quantum entanglement to solve the Mean King's Problem with complete certainty.

4.2 Linear Optical Elements

Let us consider a beam that is described by the state $|\psi_i\rangle$. A **linear optical element (LOE)** is one that takes as input a beam such as $|\psi_i\rangle$ and produces an output beam $|\psi_f\rangle$. The element outputs a beam in a linear fashion such that e.g. superposition of input beams are preserved. More specifically, let $\hat{U} \propto \sum_i c_{u,v} |u\rangle \langle v|$ describe the action of the element on the input beam, then the output state is given by.

$$|\psi_{out}\rangle = \widehat{U} |\psi_{in}\rangle \tag{4.1}$$

Figure 4.1 demonstrates the set of LOEs considered in this work. The explicit action of these states to which we adhere to are outlined in Appendix 5.

Different LOEs can act on different photonic DOFs. For this thesis, we are particularly concerned with those that act on the photon's *path mode* and *polarization*. In the former

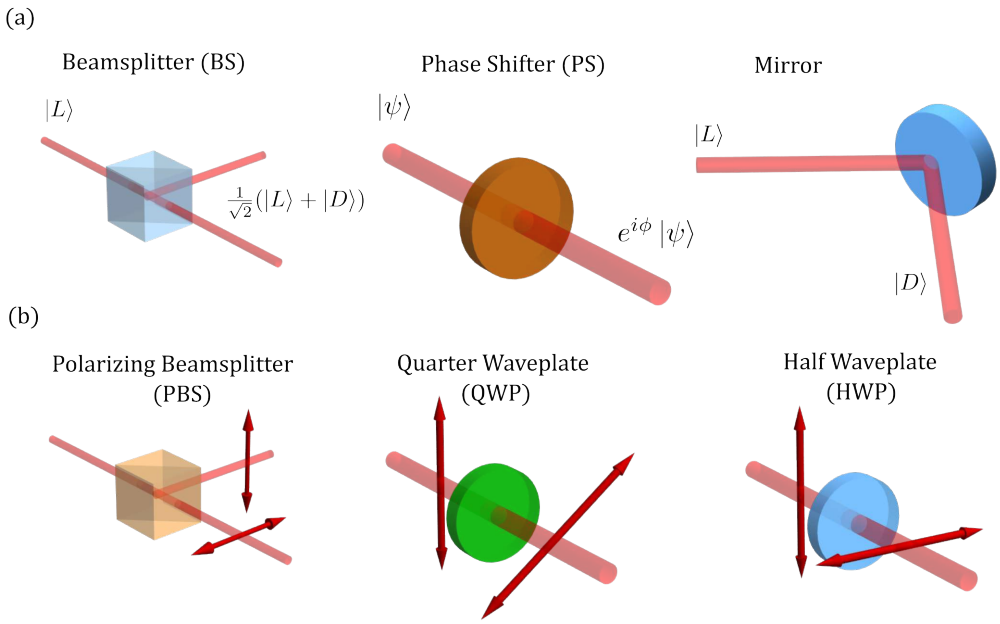

Figure 4.1: **LOEs affecting (a) spatial and (b) polarization mode DOFs.** We let $|L\rangle$ and $|D\rangle$ represent the spatial modes of the photon going down and to the left, respectively.

case, we may describe the photon in terms of the states $|L\rangle$ and $|D\rangle$, where L and D refers to the state of traveling to the left or downwards with respect to the optical element. In the latter case, the photon is described in terms of horizontal ($|H\rangle$) and vertical ($|V\rangle$) polarizations.

4.3 Mutually Unbiased Bases

Let $A = \{|\alpha_i\rangle\}_{i=0}^{D-1}$ and $B = \{|\beta_i\rangle\}_{i=0}^{D-1}$ represent two D-dimensional orthonormal bases, where D is a prime-powered number p^m. We say that they are mutually unbiased if for any states $|\alpha\rangle_i$ and $|\beta\rangle_j$ we have

$$|\langle\alpha_i|\beta_j\rangle|^2 = \frac{1}{D}. \tag{4.2}$$

In other words, if we prepare a state perfectly in one of the two Mutually Unbiased

Bases (MUB) and we then choose to project onto another MUB, then we obtain a measurement outcome $d \in 0, 1, ..., D-1$ with equal probability. In the context of quantum cryptography, an eavesdropper projecting onto an MUB that does not contain the initial state would yield no additional information. Beyond this particular context, MUB motivate the construction of the generalized bell states $|B_{0,0}\rangle$, two-qudit analogues to the familiar bell states. In addition to their application in areas such as Quantum Dense Coding [60], Quantum Cloning[61], and Quantum Entanglement Swapping [62], they also have a critical bearing in Alice's scheme against the Mean King's Problem.

Motivated towards finding MUB in arbitrarily high dimensions. We provide a proof by explicit construction using a set of Abelian subgroups known as the generalized Pauli operators for dimensions $D = p \neq 2$. Having developed the formulation of eigenstates for $D+1$ MUB, we then introduce the key states involved in doing the Mean King's Problem.

4.3.1 Proof by Explicit Construction

4.3.1.1 The Unitary Shift Operator

Let $\{|n\rangle\}_{n=0}^{D-1}$ refer to the computational basis in D dimensions. We introduce the dual basis, $\{|\hat{n}\rangle\}_{n=0}^{D-1}$ by taking the discrete quantum fourier transform

$$|\hat{n}\rangle = \frac{1}{\sqrt{D}} \sum_{k=0}^{D-1} |k\rangle \, \gamma_D^{-nk},$$

where $\gamma_D = e^{\frac{2i\pi}{D}}$ refers to the D^{th} root of unity. Let $|j\rangle$ refer to some element in the computational basis, We note that

$$\begin{aligned} |\langle j|\hat{n}\rangle| &= \left| \frac{1}{\sqrt{D}} \sum_{k=0}^{D-1} \langle j|k\rangle \, \gamma_D^{-nk} \right| \\ &= \frac{1}{\sqrt{D}} \sum_{k=0}^{D-1} \delta_{j,k} \\ &= \frac{1}{\sqrt{D}}. \end{aligned} \tag{4.3}$$

Thus, they are mutually unbiased with respect to one another.
Motivated in our pursuit to obtain more MUB, we assert them each to be eigenstates of cyclic operators $\hat{X}$ and $\hat{Z}$

$$\begin{aligned} \hat{X}\left|\hat{n}\right\rangle &= \gamma_D^n \left|\hat{n}\right\rangle \\ \hat{Z}\left|k\right\rangle &= \gamma_D^k \left|k\right\rangle . \end{aligned} \tag{4.4}$$

Following their cyclically, we require that $\hat{X}^D = \hat{Z}^D = 1$. We observe that their action is to shift by one the eigenstates of the complementary basis. Consider, for example

$$\begin{aligned} \left\langle n\right| \hat{Z} &= \frac{1}{\sqrt{D}} \sum_{k=0}^{D-1} \gamma_D^{nk} \left\langle k\right| \hat{Z} \\ &= \frac{1}{\sqrt{D}} \sum_{k=0}^{D-1} \gamma_D^{-(n+1)k} \left\langle k\right| \\ &= \left\langle n+1\right| . \end{aligned} \tag{4.5}$$

and, therefore, $\left\langle n\right| \hat{Z} = \left\langle n+1\right|$. From above, it also follows that $\left\langle D-1\right| \hat{Z} = \left\langle 0\right|$, corroborating the cyclically of the operator action. Similarly, we have that

$$\begin{aligned} \hat{X}\left|k\right\rangle &= \left|k+1\right\rangle , \\ \hat{X}\left|D-1\right\rangle &= \left|0\right\rangle . \end{aligned} \tag{4.6}$$

4.3.1.2 Heisenberg-Weyl Group

In D dimensions, the *D+1* operators from the Heisenberg-Weyl group are constructed out of the products of the the unitary shift operators. They are defined as

$$\hat{X}, \hat{Z}, \hat{X}\hat{Z}, \hat{X}\hat{Z}^2, ..., \hat{X}\hat{Z}^m. \tag{4.7}$$

We let $\left|k\right\rangle_m$ denote the k^{th} eigenstate of the operator $\hat{X}\hat{Z}^m$. In terms of the computational basis, they are defined as

$$|k\rangle_m = \frac{1}{\sqrt{D}} \sum_{j=0}^{D-1} \gamma_D^{k(D-j)-ms_j} |j\rangle \,, \tag{4.8}$$

where $s_j = \sum_{n=j}^{D-1} n$. The corresponding eigenvalue can be obtained as follows,

$$\begin{aligned}
\hat{X}\hat{Z}^m |k\rangle_m &= \frac{1}{\sqrt{D}} \sum_{j=0}^{D-1} \gamma_D^{k(D-j)-ms_j} \hat{X}\hat{Z}^m |j\rangle \\
&= \frac{1}{\sqrt{D}} \sum_{j=-1}^{D-1} \gamma_D^{k(D-j)-ms_j} \gamma_D^{mj} |j+1\rangle \\
&= \frac{1}{\sqrt{D}} \sum_{j'=0}^{D-1} \gamma_D^{k(D-(j'-1))-ms_{j'-1}+m(j-1)} |j'\rangle \\
&= \frac{\gamma_D^k}{\sqrt{D}} \sum_{j'=0}^{D-1} \gamma_D^{k(D-(j'))-ms_{j'}} |j'\rangle = \gamma_D^k |k\rangle_m
\end{aligned} \tag{4.9}$$

$$, \tag{4.10}$$

which, therefore, shows that $\hat{X}\hat{Z}^m |k\rangle_m = \gamma_D^k |k\rangle_m$.

4.3.1.3 The Proof

We now proceed to prove the existence of *D+1* MUB, each of which corresponding to a member $\hat{X}\hat{Z}^m$ of the Heisenberg-Weyl operators. We introduce the following theorem.

Theorem: Let $\{|j\rangle_a\}_{j=0}^{D-1}$ be any orthonormal basis. Let $\hat{B}$ be a D-dimensional cyclic operator whose action is described as $B|j\rangle_a = |\gamma_j| \, |j+1\rangle_a$ for $j \in 0, 1, ..., D-2$ and $|\gamma_j| \leq 1$ and $B|D-1\rangle_a = |\gamma_{D-1}| \, |0\rangle_a$. Let $\{|j\rangle_B\}_{j=0}^{D-1}$ refer to the basis corresponding to the operator $\hat{B}$, then $\{|j\rangle_a\}$ and $\{|j\rangle_B\}$ are mutually unbiased with respect to one another.

Proof: We have

$$\begin{aligned}
|\langle k_b|0_a\rangle| &= \left|\gamma_D^k \langle k_b| \hat{B}^\dagger |0_a\rangle\right| \\
&= |\lambda_0 \langle k_b|1_a\rangle| = |\langle k_b|1_a\rangle|.
\end{aligned} \tag{4.11}$$

This shows that $|\langle k_b|0_a\rangle| = |\langle k_b|1_a\rangle|$. By repeatedly applying this procedure, we can show that $|\langle k_b|1_a\rangle| = |\langle k_b|2_a\rangle| = |\langle k_b|3_a\rangle| = \ldots$

Now, we require that

$$\begin{aligned} \sum_{j=0}^{D-1} |\langle k_b|j_a\rangle|^2 &= 1 \\ \rightarrow D|\langle k_b|j_a\rangle|^2 &= 1 \\ \rightarrow |\langle k_b|j_a\rangle| &= \frac{1}{\sqrt{D}}, \end{aligned} \tag{4.12}$$

where j and k are both arbitrary, completing the proof. Towards applying this theorem onto the Heisenberg-Weyl operators, we must first ascertain their action on each other's bases. We compute,

$$\begin{aligned} \hat{X}\hat{Z}^n |k\rangle_m &= \frac{1}{\sqrt{D}} \sum_{j=0}^{D-1} \gamma_D^{k(D-j)-ms_j} \hat{X}\hat{Z}^n |j\rangle \\ &= \frac{1}{\sqrt{D}} \sum_{j=0}^{D-1} \gamma_D^{k(D-j)-ms_j-nj} |j+1\rangle \\ &= \frac{1}{\sqrt{D}} \sum_{j'=0}^{D-1} \gamma_D^{k(D-j'-1)-ms_{j'-1}-n(j'-1)} |j'\rangle \\ &= \frac{\gamma_D^{k+m-n}}{\sqrt{D}} \sum_{j'=0}^{D-1} \gamma_D^{(k+m-n)(D-j')-ms_{j'}} |j'\rangle \\ &= \gamma_D^{k+m-n} |k+m-n\rangle_m . \end{aligned}$$

In other words, since $|\gamma_D|^n = 1$ when raised by any power n, we can apply the previous theorem to show that $|\langle k_m|k_n\rangle| = \frac{1}{\sqrt{D}}$ for two bases $\{|k\rangle_m\}_{k=0}^{D-1}$ and $\{|k\rangle_n\}_{k=0}^{D-1}$ from the Heisenberg-Weyl groups. We have thus proven the pairwise mutually unbiasedness from the bases, and have therefore shown the existence of $D+1$ mutually unbiased bases.

Research Article Vol. 1, No. 2 / 25 December 2023 / Optica Quantum 49

OPTICA QUANTUM

Experimental solutions to the high-dimensional mean king's problem

Tareq Jaouni,[1,*] Xiaoqin Gao,[1,3] Sören Arlt,[2] Mario Krenn,[2] and Ebrahim Karimi[1,2]

[1] Nexus for Quantum Technologies, University of Ottawa, K1N 6N5, ON, Ottawa, Canada
[2] Max Planck Institute for the Science of Light, Erlangen, Germany
[3] xgao5@uottawa.ca
[*] tjaou104@uottawa.ca

Received 3 August 2023; revised 17 November 2023; accepted 17 November 2023; published 13 December 2023

Vaidman, Aharanov, and Albert [Phys. Rev. Lett. 58(14), 1385 (1987)] put forward a puzzle called the mean king's problem (MKP) that can be solved only by harnessing quantum entanglement. Prime-powered solutions to the problem have been shown to exist, but they have not yet been experimentally realized for any dimension beyond two. We propose a general first-of-its-kind experimental scheme for solving the MKP in prime dimensions (D). Our search is guided by the digital discovery framework Pytheus, which finds highly interpretable graph-based representations of quantum optical experimental setups; using it, we find specific solutions and generalize to higher dimensions through human insight. As proof of principle, we present a detailed investigation of our solution for the three-, five-, and seven-dimensional cases. We obtain maximum success probabilities of 82.3%, 56.2%, and 35.5%, respectively. We therefore posit that our computer-inspired scheme yields solutions that implement Alice's strategy with quantum advantage, demonstrating its promise for experimental implementation in quantum communication tasks.

https://doi.org/10.1364/OPTICAQ.502451

1. INTRODUCTION

The mean king's problem (MKP) is a quantum puzzle originally posed by Vaidman, Albert, and Aharanov [1] that chronicles how one may leverage the properties of quantum entanglement to ascertain the values of the non-commutable Pauli operators σ_x, σ_y, and σ_z from a spin-1/2 particle. The problem is described as follows: a physicist (Alice) prepares a quantum system to her whims and sends it to a mean king, who secretly performs projection-valued measurement (PVM) on one of the Pauli spin operators. The king then allows Alice to perform one more experiment, after which he reveals which operator he measured and challenges her to guess his measurement outcome correctly. As we will further elaborate upon in Section 2, the authors reveal that Alice can escape the mean king's cruelty with a theoretical success probability of 100% by entangling her particle onto an ancillary particle, which she tends to do in secret, and by choosing to perform a projective valued measurement of her own for her final experiment.

The MKP has since been adapted to various contexts [2–4]. Crucially, it has been shown that the author's original trick can also be extended to prime [5] and prime-powered [6–10] dimensions when the mean king makes his measurement in a maximal set of mutually unbiased bases (MUBs); it has also been shown [11] to exist in composite dimensions (e.g., in $D = 6$ and $D = 10$) when one allows positive operator-valued measurements (POVMs) to be performed instead. The applicability of the MKP has also been considered in quantum key distribution (QKD) [12–14]. Here, the same protocol can be used to agree on a shared secret key made of a string of dits (d-dimensional bits).

Considering the possible applications of the MKP, it is interesting to implement it experimentally. Quantum optical setups which implement the two-dimensional mean king's problem have been proposed [15,16]; In particular, Schulz *et al.* proposed an experimental realization for the two-dimensional mean king's problem by using entanglement with two degrees of freedom (DOFs), polarization, and spatial mode of a single photon. Their experimental setup would have the mean king Bob imitate a PVM by transforming the input state onto one of several possible choices of eigenstates. It achieved an experimental success probability of 95.6%. An experimental implementation of the tracking the king problem, a variant to the MKP in which the mean king does not disclose to Alice his measurement basis, has also been proposed [17], achieving reasonable success probabilities of 81.3%. However, there does not yet exist an experimental proposal for higher dimensions which, particularly within the context of QKD, shows promise due to its robustness to environmental noise [18–20]. The difficulty in experimentally implementing the MKP in higher dimensions is due to the final

2837-6714/23/020049-06 Journal © 2023 Optica Publishing Group

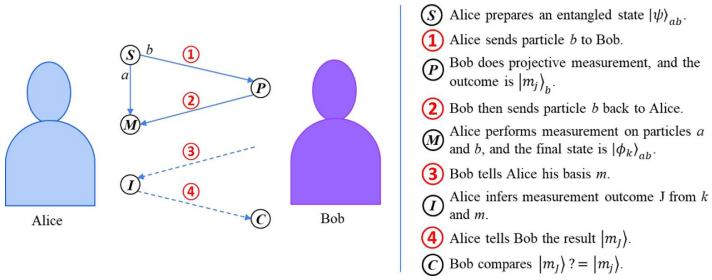

Fig. 1. Step-by-step process of Alice's solution to the MKP. She escapes the mean king's cruelty by entangling and keeping an ancilla secret from the photon she sends to the king. Upon performing a PVM, the king returns Alice's original photon. She then measures both of her photons based on the VAA states, to which the result of her measurement unravels to her the king's measurement result. Over a classical channel, the king reveals to Alice his measurement basis, and Alice, in turn, answers with her guess.

step, in which Alice must measure the non-trivial basis of D^2 Vaidman–Albert–Aharanov (VAA) states.

This paper illustrates a computer-inspired approach that yields experimental setups for the MKP in arbitrarily high dimensions using entangled two-photon states. We exploit the highly interpretable, graph-theoretical representation of quantum optical experiments [21,22]. We determine the correct solution using the AI-based framework Pytheus [23] for two and three dimensions, then generalize from these solutions to higher dimensions using human insight. Our experimental solutions can be implemented using linear optical elements and can be realized using any photonic DOF. We demonstrate that our setups' success probabilities significantly exceed classical odds of $\frac{1}{D}$, implicating the quantum advantage of our approach.

2. HIGH-DIMENSIONAL MKP CONCEPT

Figure 1 shows Alice's protocol for solving the high-dimensional mean king's problem. We follow the approach in [6], and confine our study to $D = p > 2$ dimensions, where p is a prime number. The solution may also be adapted to $D = p^n$ (or prime-powered) dimensions by working in arithmetic defined by the dimension's corresponding finite field [7].

Alice's stratagem to escape the mean king's cruelty works as follows. At step S (Send), Alice prepares two entangled photons, labeled a and b for Alice and Bob, in a generalized Bell state according to

$$|\psi\rangle_{ab} = |B_{0,0}\rangle_{a,b} = \frac{1}{\sqrt{D}} \sum_{j=0}^{D-1} |\overline{m_j}\rangle_a |m_j\rangle_b, \tag{1}$$

where $\{|m_j\rangle\}_j^{D-1}$ is the jth element of the mth MUB in D-dimensional Hilbert space, and the conjugate ket, $|\overline{\psi}\rangle$, is defined for any two states $|\psi\rangle$ and $|\phi\rangle$ according to Eq. (3.2) ($|\phi\rangle\langle\psi| \leftrightarrow |\overline{\psi}\rangle|\phi\rangle$) in [7],

$$|\overline{\psi}\rangle = \sum_{j=0}^{D-1} |j\rangle\langle j|\psi\rangle^*. \tag{2}$$

This convention allows us to choose any MUB in the construction of $|\psi\rangle_{ab}$.

While keeping photon a for herself, Alice advances to the Projection (P) stage. She sends photon b to the mean king, who performs a projection-valued measurement (PVM) on the photon in one of $D + 1$ possible mutually unbiased bases (MUBs) and yields an outcome $j = 0, 1, \ldots, D - 1$. This collapses the overall state to $|m_j\rangle_{a,b} = |\overline{m_j}\rangle_a |m_j\rangle_b$, where $|m_j\rangle$ refers to the jth eigenstate in the mth MUB.

After having received photon b back from the king, Alice moves to the Measure (M) stage: she must now retrodict the king's measurement result $|m_j\rangle_b$. To achieve this with complete certainty, Alice performs a simultaneous measurement of both photons based on the VAA states. These are defined as

$$|\phi_k\rangle = -|B_{0,0}\rangle_{a,b} + \frac{1}{\sqrt{D}} \sum_{m=0}^{D} |m_{f_k(m)}\rangle_{a,b}, \tag{3}$$

where $f_k(m)$ is a mapping function uniquely defined for each VAA state which maps the king's possible measurement bases to Alice's estimate of his outcome. Following [6], the mapping function can be defined as a constructor for a set of $D + 1$ mutually orthogonal Latin squares:

$$f_k(m) = \begin{cases} (m \times i - j) \mod D & \text{if } m < D, \\ i & \text{if } m = D, \end{cases} \tag{4}$$

where (i, j) are indices corresponding to an entry in the mth Latin square. These indices are obtained via the decomposition $k = jD + i$.

Having completed her measurement, the king now discloses his measurement basis to Alice over a classical channel and awaits Alice's response. The VAA states have the crucial property that

$$\langle\phi_k|m_j\rangle_{a,b} = \frac{1}{\sqrt{D}} \delta_{j,f_k(m)}. \tag{5}$$

In other words, for each of the king's measurement results, there exists a disjoint subset of VAA states, $\{|\phi_k\rangle\}_{|m_j\rangle_b}$, which encompasses Alice's possible measurement outcomes. Therefore, regardless of which outcome she obtains within this subset, Alice always guesses $|m_j\rangle_b$, and ends up escaping the mean king's cruelty with a success probability of 1.

3. WORK PRINCIPLE

We search for experimental realizations of the MKP using

an algorithm based on a graph-theoretical representation of quantum linear optical setups [21,22]. We ascertain the graph-theoretical solutions' general form using Pytheus [23], then translate them into experimental setups using the procedure outlined in Section 1 of Supplement 1. We conceive our graph-theoretical representations such that one VAA state coincides with two detectors in our setup. Surprisingly, however, we also find it possible to project onto other VAA states by adding additional detectors where a beam splitter joins two paths, and we observe loss, increasing the number of possible two-fold detection events associated with each VAA state.

We then optimize the setup further to project across the entire VAA basis by employing a post-processing optimization algorithm on the phase shifters of our setup. We may compute the success probability p_V that, given the input VAA state $|\phi_k\rangle$, Alice concludes that she measures $|\phi_k\rangle$ using the procedure outlined in Section 2 of Supplement 1. We then tune the phase shifters $\varphi = (\varphi_1, \varphi_2, \ldots)$ in our setup by employing the Broyden–Fletcher–Goldfarb–Shanno (BFGS) algorithm [24] with a loss function defined as

$$L(\varphi) = -p_V(\varphi). \tag{6}$$

We run the algorithm for 1000 iterations with random initialization of the phases to account for the multimodality of the parameter space. We then quantify our setups' performance regarding the MKP success probability, p_M, that Alice can successfully retrodict the mean king's measurement result.

4. RESULTS

4.1. 3D MKP

We obtain the graph corresponding to the 3D VAA measurement, shown in Fig. 2(a), using Pytheus [23,25]. We choose the third VAA state to be our target:

$$|\phi_k\rangle = \frac{1}{\sqrt{3}}(|00\rangle + \alpha(|01\rangle + |20\rangle) + \beta(|01\rangle + |20\rangle) + \gamma|12\rangle + \delta|21\rangle) + \beta(|12\rangle) + \gamma(|21\rangle)), \tag{7}$$

where $\omega = e^{-i2\pi/3}$, $\alpha = (2\omega^2 + \omega)/3$, $\beta = (\omega^2 + 2\omega)/3$, $\gamma = (\omega + 2)/3$ and $\delta = (2 + \omega^2)/3$.

Figure 2(a) shows the corresponding experimental setup. The action of the setup on the initial state is given in the operator form $\widehat{M}(\varphi)$ as

$$\begin{bmatrix} a_0 \\ a_1 \\ a_2 \\ b_0 \\ b_1 \\ b_2 \end{bmatrix} = \begin{bmatrix} \varphi_1 & i\varphi_1 & i\varphi_1 & -\varphi_1 & 0 & 0 & i\varphi_1 \\ -\varphi_3 & 0 & i\varphi_3 & 0 & \varphi_3 & 0 & 0 \\ 0 & i\varphi_5 & 0 & \varphi_5 & 0 & i\varphi_5 & 0 \\ i\varphi_2 & \varphi_2 & -\varphi_2 & i\varphi_2 & 0 & 0 & \varphi_2 \\ i\varphi_4 & 0 & \varphi_4 & 0 & i\varphi_4 & 0 & 0 \\ 0 & -\varphi_6 & 0 & i\varphi_6 & 0 & \varphi_6 & 0 \end{bmatrix} \begin{bmatrix} c_0 \\ d_0 \\ 1_0 \\ 2_0 \\ 3_0 \\ 4_0 \\ 5_0 \end{bmatrix}. \tag{8}$$

We report the success probabilities of Alice's measurement for each MUB in Table 1. After optimization, we compute a success probability of 91.7% for the m=0 basis, 73.0% for the m=1 basis, 69.7% for the m=2 basis, and 63.5% for the m=3 basis. Altogether, this results in an average success probability of 74.5%. However, the overall success probability of Alice's MKP measurement depends on the exact set of MUBs chosen by the king. In particular, the maximum success probability of 82.3% is achieved when Bob only chooses the first two MUBs.

We provide a possible experimental setup that realizes the three-dimensional MKP in Fig. 3. Taking inspiration from [26], an ultraviolet (UV) laser is pumped toward a collection of beam displacers and half-wave plates (HWPs) which projects the incident photons' polarization onto $|H\rangle + |V\rangle$. This results

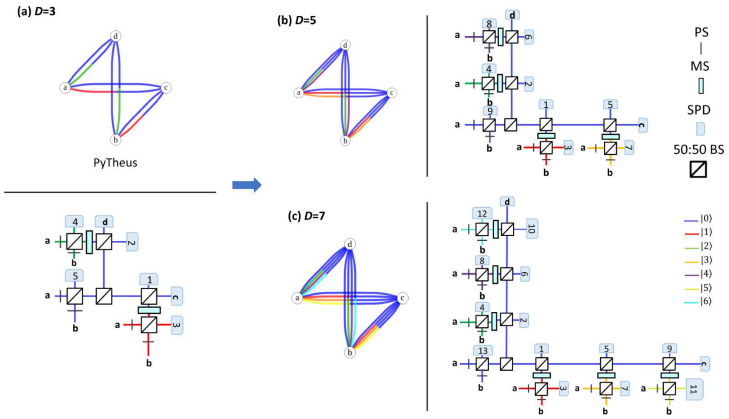

Fig. 2. High-dimensional MKP concept. Quantum optical graphs and their corresponding experimental translation for high-dimensional MKP. We show experimental setups corresponding to schemes for (a) three-dimensional, (b) five-dimensional, and (c) seven-dimensional MKP. We determine the three-dimensional graph-theoretical solution shown in panel (a) via the digital discovery framework Pytheus . Then, we carry out the experimental translation by creating direct paths from incident photons to detectors. Additional loss detectors, N_0 where $N \in \mathbf{N}$, are placed at the exit ports of the beam splitters to provide us with additional information. The three-dimensional solution does not allow simultaneous clicks for higher-order photon modes; we may exploit this idea to ascertain the solutions for arbitrarily high dimensions easily. BS, beam splitter; PS, phase shifter; MS, mode shifter; SPD, single-photon detector.

Table 1. MKP Success Probability (p_M) for Different Dimensions

D	m=0	m=1	m=2	m=3	m=4	m=5	m=6	m=7
3	91.7%	73.0%	69.7%	63.5%	-	-	-	-
5	61.3%	34.4%	51.0%	50.7%	29.9%	32.9%	-	-
7	40.8%	27.5%	27.9%	22.7%	26.5%	30.2%	29.0%	28.1%

in three beams pumping into a type-II β-barium borate (BBO) crystal. It yields three correlated photon pairs, which we may then split through an action of a polarizing beam splitter (PBS); therefore, we encode the photons' dimensionality using the path mode DOF, while the polarization DOF is used to help achieve certain transformations onto the state. In particular, Bob uses it to achieve his PVM onto an eigenstate of his choosing, using the input configuration provided in [27] and the wave plate angle configurations provided in Supplement 1. To ensure the photons' indistinguishability, Alice and Bob's polarizations are matched via the action of the HWP before being sent to the VAA analyzer described above.

At the cost of increasing complexity, improving upon the average success probability of the VAA measurement further by considering all of the three possible graph-theoretical solutions that we can obtain for the three-dimensional MKP is possible. The 3^2 VAA states in three dimensions can be partitioned into three disjoint sets: one set contains VAA states with kets $|00\rangle$, but not $|11\rangle$ or $|22\rangle$. The other sets feature states that satisfy a cyclic permutation of this condition (e.g., $|11\rangle$, but not $|00\rangle$ or $|22\rangle$). Consequently, each subset is represented by a different graph-theoretical solution, where simultaneous clicks are conditioned on photons in the same mode. By implementing all three graph-theoretical solutions together, using the recipe described above, we observe a noticeable increase in the success probability.

4.2. MKP in Higher Dimensions

We make the following inference to generalize our computer-inspired solution for the three-dimensional case to higher dimensions: the VAA state given in Eq. (3) has seven of the nine possible two-qutrit ket states, which determines the set of allowed two-detector click patterns. Crucially, we cannot have a two-fold detector click if both qutrits are of the same higher-order mode (i.e., $|11\rangle$ *or* $|22\rangle$). In the graph representation, this means that we cannot have perfect matchings realizing the kets $|11\rangle$ or $|22\rangle$, in which each would consist of one edge representing a higher-order mode (1 or 2) between vertices a and one of the detector vertices c or d, and another edge of the same mode between vertices b and a different detector vertex. As this is a quality that is shared among the VAA states for D dimensions – by our construction, the first five VAA states in five dimensions have $|00\rangle$, but not $|11\rangle$, $|22\rangle$, $|33\rangle$, or $|44\rangle$, for example – we can build upon the graph-theoretical solution in three dimensions by adding higher order edges which go from both input mode vertices to *one* output mode detector. It allows us to obtain generalizations of our graph-theoretical solution to arbitrarily high dimensions.

We demonstrate this idea with a couple of examples: Fig. 2(b) showcases the experimental solution in five dimensions. As before, the input modes a_i, b_i for $i \in \{0, 1, 2, 3, 4\}$ are transformed into the detector modes c_0, d_0 as well as the loss detector modes $1_0, 2_0, \ldots, 9_0$ via the operator $\widehat{M(\varphi)}$, with $\varphi = (\varphi_1, \varphi_2, \ldots, \varphi_{10})$. The MKP success probabilities for the six MUBs in 5D are (in order): 61.3%, 34.4%, 51.0%, 50.7%, 29.9%, and 32.9%. Averaged out over all bases yields a success probability of 43.4%. In particular, we achieve a maximal success probability of 56.8% if the king solely chooses to measure on MUBs of m=0 and m=2, significantly exceeding the classical success probability.

We iterate upon this idea further by considering the seven-dimensional construction, as shown in Fig. 2(c). For the eight possible MUBs that the mean king may choose, we report an average success probability of 29.1%, with a maximal success probability of 35.5% if the king chooses the bases m=0 and m=5. We detail the success probabilities of Alice's measurement on the complete set of MUBs in each high-dimensional case in Table 1.

We remark that our success probabilities are lower than the theoretical limit of 1. We attribute this chiefly to our use of linear optical elements in our setup. In principle, the graph-theoretical solution configured for one particular state realizes a projective measurement on that state with 100% success probability. However, if we consider successful measurements only on the coincidence of detectors c and d, the success probability will significantly be reduced. The drop in success probability is due to the presence of linear optics (beam splitters), which introduce loss. We make best use of this loss by using it as an additional source of information, allowing us to extend our measurement to other states in the VAA basis. We provide a detailed explanation about the effects of using linear optical elements on the MKP success probability in Section 3 of Supplement 1.

To this point, we have illustrated how to obtain experimental setups for three high-dimensional cases of MKP. By using the abovementioned idea behind generalizing the graph-theoretical solution, we may access ever higher dimensions, allowing us to tap into their increased information capacity and noise robustness benefits. The higher dimensional realizations described before and any other arbitrarily high dimensional variant of the MKP can also be realized using the general experimental setup described in Section 5 of Supplement 1.

5. CONCLUSION

By leveraging graph-theoretical representations of quantum optical experiments, we describe a scheme to formulate quantum optical realizations of Vaidman, Albert, and Aharanov's quantum thought experiment for arbitrarily high dimensions. As a proof of principle, we propose how one may design experimental setups for three-dimensional, five-dimensional, and seven-dimensional cases. Considering every possible choice of MUB by the king, we report maximal success probabilities of 82.3%, 56.2%, and 35.5%, respectively, which demonstrates the quantum advantage of our approach.

In our experimental scheme, we only use linear optical elements, which are easily accessible in any optics lab. The number of elements we use scales linearly with the dimension of the system. Encompassing these two points, our experimental scheme is realizable in higher dimensions. Our experimental scheme works for the path degree of freedom, but also works for other degrees of freedom, e.g., orbital angular momentum. We anticipate that the success probabilities of our measurement can be further improved by adapting nonlinear elements in lieu of beam splitters, which are the principal sources of loss in our experimental setups. We foresee our experimental solutions facilitating

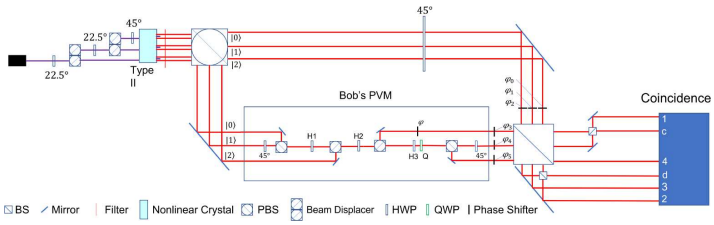

Fig. 3. Experimental setup. Example setup that exploits path mode encoding to realize the MKP protocol for three dimensions. Alice exploits the polarization degree of freedom to produce three pump beams that, following SPDC, create three correlated photon pairs. Alice's photon is sent toward the VAA analyzer, while Bob imitates a PVM onto his photon to the eigenstate of his choosing before being sent to the VAA analyzer. PBS, polarizing beam splitter; H1–H3, half-wave plates (HWPs); Q, quarter-wave plate (QWP).

the near-term implementation of MKP in quantum communication tasks, in particular, quantum key establishment. Bub [14] and Werner [12] both suggest protocols in which Bob and Alice develop a shared secret key by communicating their results over a classical channel. Up to the known errors of our experimental setups, the disagreement of even one bit implicates the presence of an eavesdropper.

Our scheme illustrates another case in which artificial intelligence (AI) and human insight work in tandem [28,29]. As the representation of our solutions lends itself to interpretability, we were able to extract insight into the nature of our solutions through the solution to the three-dimensional case and generalize it to solve the more complicated problem of high-dimensional MKP. We hope this work gives further credence to a future in which AI- and human-based intuition work together to discover new science [30].

Funding. The Joint Centre for Extreme Photonics; The High Throughput and Secure Networks Challenge Program at the National Research Council of Canada; Canada Research Chairs.

Acknowledgments. The authors would like to thank Khabat Heshami and Alicia Sit for their valuable discussions, as well as Manuel Ferrer for his help in the current version of the analysis code. This work was supported by the Canada Research Chairs (CRC), the High Throughput and Secure Networks (HTSN) Challenge Program at the National Research Council of Canada, and the Joint Centre for Extreme Photonics (JCEP).

Disclosures. The authors declare no conflict of interest.

Data Availability. Data and code underlying the results presented in this paper can be found in [31].

Supplemental document. See Supplement 1 for supporting content.

REFERENCES

1. L. Vaidman, Y. Aharonov, and D. Z. Albert, "How to ascertain the values of σ_x, σ_y, and σ_z of a spin- *1/2* particle," Phys. Rev. Lett. **58**(14), 1385–1387 (1987).
2. A. Botero and Y. Aharonov, "The "mean king's problem" with continuous variables,", arXiv, arXiv:0710.2952 (2007).
3. M. Yoshida, G. Kimura, T. Miyadera, H. Imai, and J. Cheng, "Solution to the mean king's problem using quantum error-correcting codes," Phys. Rev. A **91**(5), 052326 (2015).
4. M. Reimpell and R. F. Werner, "A meaner king uses biased bases," Phys. Rev. A **75**(6), 062334 (2007).
5. B.-G. Englert and Y. Aharonov, "The mean king's problem: Prime degrees of freedom," Phys. Lett. A **284**(1), 1–5 (2001).
6. A. Hayashi, M. Horibe, and T. Hashimoto, "Mean king's problem with mutually unbiased bases and orthogonal latin squares," Phys. Rev. A **71**(5), 052331 (2005).
7. T. Durt, B.-G. Englert, I. Bengtsson, and K. Zyczkowski, "On mutually unbiased bases," Int. J. Quantum Inform. **08**(04), 535–640 (2010).
8. M. Revzen, "Geometrical view of the mean king problem,", arXiv, arXiv:1205.5406 (2012).
9. A. Klappenecker and M. Roetteler, "New tales of the mean king," arXiv, arXiv:quant-ph/0502138 (2005).
10. K. Bar and J. Vicary, "A 2-categorical analysis of complementary families, quantum key distribution and the mean king problem," Electron. Proc. Theor. Comput. Sci. **172**, 316–332 (2014).
11. G. Kimura, H. Tanaka, and M. Ozawa, "Solution to the mean king's problem with mutually unbiased bases for arbitrary levels," Phys. Rev. A **73**(5), 050301 (2006).
12. A. H. Werner, T. Franz, and R. F. Werner, "Quantum cryptography as a retrodiction problem," Phys. Rev. Lett. **103**(22), 220504 (2009).
13. H. Azuma and M. Ban, "The intercept/resend and translucent attacks on the quantum key distribution protocol based on the pre- and post-selection effect," Int. J. Quantum Inform. **19**(01), 2150010 (2021).
14. J. Bub, "Secure key distribution via pre- and postselected quantum states," Phys. Rev. A **63**(3), 032309 (2001).
15. O. Schulz, R. Steinhübl, M. Weber, B.-G. Englert, C. Kurtsiefer, and H. Weinfurter, "Ascertaining the values of σ_x, σ_y, and σ_z of a polarization qubit," Phys. Rev. Lett. **90**(17), 177901 (2003).
16. B.-G. Englert, C. Kurtsiefer, and H. Weinfurter, "Universal unitary gate for single-photon 2-qubit states," Phys. Rev. A **63**(3), 032303 (2001).
17. C.-Q. Hu, J. Gao, L.-F. Qiao, R.-J. Ren, Z. Cao, Z.-Q. Yan, Z.-Q. Jiao, H. Tang, Z.-H. Ma, and X.-M. Jin, "Experimental test of tracking the king problem," Research **2019**, 1–6 (2019).
18. M. D. Al-Amri, D. L. Andrews, and M. Babiker, *Structured Light for Optical Communication* (Elsevier, 2021).
19. F. Bouchard, K. Heshami, D. England, R. Fickler, R. W. Boyd, B.-G. Englert, L. L. Sánchez-Soto, and E. Karimi, "Experimental investigation of high-dimensional quantum key distribution protocols with twisted photons," Quantum **2**, 111 (2018).
20. B. Da Lio, D. Cozzolino, N. Biagi, Y. Ding, K. Rottwitt, A. Zavatta, D. Bacco, and L. K. Oxenløwe, "Path-encoded high-dimensional quantum communication over a 2-km multicore fiber," npj Quantum Inf. **7**(1), 63 (2021).
21. X. Gu, M. Erhard, A. Zeilinger, and M. Krenn, "Quantum experiments and graphs II: Quantum interference, computation, and state generation," Proc. Natl. Acad. Sci. U. S. A. **116**(10), 4147–4155 (2019).
22. M. Krenn, X. Gu, and A. Zeilinger, "Quantum experiments and graphs: Multiparty states as coherent superpositions of perfect matchings," Phys. Rev. Lett. **119**(24), 240403 (2017).
23. C. Ruiz-Gonzalez, S. Arlt, J. Petermann, S. Sayyad, T. Jaouni, E. Karimi, N. Tischler, X. Gu, and M. Krenn, "Digital discovery of 100 diverse quantum experiments with PyTheus," arXiv, arXiv:2210.09980 (2022).
24. J. N. S. J. Wright, *Numerical Optimization* (Springer, 2006).

25. M. Krenn, J. Kottmann, N. Tischler, and A. Aspuru-Guzik, "Conceptual understanding through efficient inverse-design of quantum optical experiments," Phys. Rev. X **11**(3), 031044 (2021).
26. X.-M. Hu, C. Zhang, Y. Guo, F.-X. Wang, W.-B. Xing, C.-X. Huang, B.-H. Liu, Y.-F. Huang, C.-F. Li, G.-C. Guo, X. Gao, M. Pivoluska, and M. Huber, "Pathways for entanglement-based quantum communication in the face of high noise," Phys. Rev. Lett. **127**(11), 110505 (2021).
27. Y.-H. Luo, H.-S. Zhong, M. Erhard, X.-L. Wang, L.-C. Peng, M. Krenn, X. Jiang, L. Li, N.-L. Liu, C.-Y. Lu, A. Zeilinger, and J.-W. Pan, "Quantum teleportation in high dimensions," Phys. Rev. Lett. **123**(7), 070505 (2019).
28. M. Krenn, M. Malik, R. Fickler, R. Lapkiewicz, and A. Zeilinger, "Automated search for new quantum experiments," Phys. Rev. Lett. **116**(9), 090405 (2016).
29. M. Krenn, M. Erhard, and A. Zeilinger, "Computer-inspired quantum experiments," Nat. Rev. Phys. **2**(11), 649–661 (2020).
30. M. Krenn, R. Pollice, S. Y. Guo, M. Aldeghi, A. Cervera-Lierta, P. Friederich, G. dos Passos Gomes, F. Häse, A. Jinich, A. Nigam, Z. Yao, and A. Aspuru-Guzik, "On scientific understanding with artificial intelligence," Nat. Rev. Phys. **4**(12), 761–769 (2022).
31. T. Jaouni, X. Gao, S. Arlt, M. Krenn, and E. Karimi, "Mkpy: Python framework for analysing the high-dimensional mean king's problem," GitHub (2023), https://github.com/TareqJ1000/meanKing.

Chapter 5

Conclusions

In closing, we have presented a theoretical investigation on the link between quantum optical experiments and graph theory. We present a proof of principle for the automated setup paradigm, PyTheus, which exploits this link to find highly interpretable representations of quantum optical experiments. Through this unified insight into humans and machines, we discover 100 intriguing quantum experiments to various tasks. We also frame our investigation in the context of scientific discovery to demonstrate the high interpretability of the quantum graphs' formalism. Notably, we present preliminary results for an interpretability tool that probes into the physical rationale of neural networks in order to understand what they learn about quantum experiments, and we conceive a proof of principle scheme for experimental setups which implements with quantum advantage the extensively studied, high-dimensional solutions to the MKP.

In Chapter 2, we pedagogically introduce the formalism of quantum graphs. We explain how to access the information held by quantum graphs in terms of their weight function, and highlight their application for state creation and quantum measurements, among others. Furthermore, we introduce the Python-based, digital framework PyTheus, which facilitates the search for new quantum experiments through inverse design; starting from a complete graph, we topologically optimize it towards a target state or property. As a proof of principle, we set a goal to search for one hundred quantum experiments for various tasks, from the creation of quantum states in entanglement research and quantum simulators to new protocols in quantum communication and quantum computing. We even show that PyTheus can help verify certain involving combinatorical measures such as the assembly index [63]. This is by no means a comprehensive account of everything that can be discovered by PyTheus, and we hope that scientists may use it to find quantum experiments to yet unexplored tasks in QIP. Furthermore, we anticipate that the quantum graphs' ease of

interpretability in terms of common, tabletop optical elements will lead to their near-term implementation by experimental groups worldwide. We draw attention to the recent work of Bao et al. [31], which presents preliminary results for a reconfigurable linear optical device utilizing 'very-large-scale integrated nanophotonic circuits' to implement quantum graphs. This presents an exciting platform to experimentally implement our quantum graphs. Finally, we remark that, for some of our solutions, we were able to extract the physical concepts contained therein, such as a new form of multiphoton inference [41]. This strongly attests to our tools' ability to contribute to scientific understanding [64].

In the following chapters, we focus on the possibility of discovering new physics through quantum graphs. In Chapter 3, we use an XAI technique known as *deep dreaming*, which enables us to visualize what feedforward neural networks learn about quantum optical experiments. Specifically, we first train neural networks to predict properties of quantum systems, then "invert" the training, prompting the network to gradually imagine a quantum experiment that excites it. When we apply this technique on the network's output layer, which produces its prediction on one of the various possible target properties, we find that the network consistently shifts the initial value distribution and, observing the intermediate steps from the initial quantum graph to its final, "dreamed" analogue, we are able to conceptualize the learned strategies of the network. We also gain insight into how the neural network comes up with its solution by applying our technique to the intermediate layers of the network. Intriguingly, in the first layers, we find the network identifies simple structures, while deeper within the network, we observe more complicated quantum systems. We also find that the neurons in the network are trained to over-interpret various possible configurations in reminiscence to neuron multifacetedness [65]. We, therefore, are able to synthesize a complete picture of what neural networks see.

Ultimately, we anticipate that our tool may facilitate the creation of AI-based "oracles" in quantum physics, which are more interpretable and reliable. Specifically, we may consider automated routines in setup design, such as the aforementioned PyTheus, which adapts surrogate neural network models. We believe that our tool can be used to reliably guide the design of quantum experiments optimized for a target state or property, and to verify that the network achieves its goal using physical insight. We also remark that our tool adds another layer of interpretability to our quantum graph solutions: in addition to the solution itself, we also have insight into the rationale leading to it, which may itself unravel new science. We expect that we may enhance the interpretability of our dreams by applying regularization techniques [1, 65, 66], or by analyzing simplified variants of our neural networks derived from pruning strategies [67].

In Chapter 4, we chronicle a brand new ending to Alice's attempts to escape the Mean King's cruelty through a proof of principle for a new experimental scheme for high-

dimensional cases. We establish the theoretical foundation of Alice's stratagem to the Mean King's puzzle: the existence of $D+1$ MUBs for D prime, the initial, maximally entangled state that Alice must prepare, and the enigmatic VAA states over which Alice must measure. We then ask PyTheus to find an experimental setup that realizes the projection to one of the VAA states in three dimensions. We later find that we can extend our projection by adding detectors where a BS joins two paths and where loss is observed. From our graph-theoretical solution in two- and three-dimensions, we determine their underlying pattern, which we then use to generalize to higher dimensions. After fine-tuning our setup via post-processing, we find that Alice's success probability doubles over randomly guessing the King's measurement results: for three-, five- and seven- dimensions, Alice's success probabilities over the $D+1$ MUBs are estimated to be at 72.8%, 45.8%, and 34.8% respectively. This certifies that we are implementing the quantum advantage of Alice's solution.

We, therefore, lay the groundwork for first-of-their-kind experiments to the high-dimensional MKP, and anticipate their near-term implementation for tasks in quantum communication, notably in high-dimensional quantum key distribution as described by Bub [68] and Werner [69]. We also position our work as an example of how PyTheus can enable new discoveries in physics. We extract the physical basis from its discovery in a lower dimension and then use it to find viable generalizations in higher dimensions. We anticipate that our proof of principle can even be extended to composite dimensions by allowing Alice to perform projective operator-valued measurements (POVMs) and construct the VAA bases using *orthogonal arrays* as discussed in [56]. It will also be interesting to see if, through quantum graphs, one can find experimental solutions to modifications to the MKP, such as Tracking the King [58] and the Mean King's Problem with Biased Bases [57].

The discovery of new quantum phenomena necessitates the search for new experimental designs, particularly those which harness photons, that implement them. We, therefore, foresee the need for simple, interpretable representations that implement the conceptual core of such phenomena, as well as automated setup design routines to navigate the ocean of possible configurations. Through the works featured in this thesis, we not only posit that quantum graphs show promise towards making practical the physical realization of complex quantum phenomena, but that they can enable AI-based frameworks to inspire new ideas in the human scientist. We hope that this helps make a new wave of experimental research in quantum physics while, perhaps, unraveling yet-undiscovered quantum phenomena.

Bibliography

[1] A Mordvintsev, C Olah, and M Tyka. Inceptionism: Going Deeper into Neural Networks, jun 2015. Avaliable at https://ai.googleblog.com/2015/06/inceptionism-going-deeper-into-neural.html.

[2] Daniel M Greenberger, Michael A Horne, and Anton Zeilinger. Going beyond bell's theorem. In *Bell's theorem, quantum theory and conceptions of the universe*, pages 69–72. Springer, 1989.

[3] Marissa Giustina, Marijn A. M. Versteegh, Sören Wengerowsky, Johannes Handsteiner, Armin Hochrainer, Kevin Phelan, Fabian Steinlechner, Johannes Kofler, Jan-Åke Larsson, Carlos Abellán, Waldimar Amaya, Valerio Pruneri, Morgan W. Mitchell, Jörn Beyer, Thomas Gerrits, Adriana E. Lita, Lynden K. Shalm, Sae Woo Nam, Thomas Scheidl, Rupert Ursin, Bernhard Wittmann, and Anton Zeilinger. Significant-loophole-free test of bell's theorem with entangled photons. *Phys. Rev. Lett.*, 115:250401, Dec 2015.

[4] Sara Bartolucci, Patrick Birchall, Hector Bombin, Hugo Cable, Chris Dawson, Mercedes Gimeno-Segovia, Eric Johnston, Konrad Kieling, Naomi Nickerson, Mihir Pant, Fernando Pastawski, Terry Rudolph, and Chris Sparrow. Fusion-based quantum computation, 2021.

[5] Alán Aspuru-Guzik and Philip Walther. Photonic quantum simulators. *Nature Physics*, 8, 04 2012.

[6] Emanuele Polino, Mauro Valeri, Nicolò Spagnolo, and Fabio Sciarrino. Photonic quantum metrology. *AVS Quantum Science*, 2(2), 2020.

[7] Pieter Kok, William J Munro, Kae Nemoto, Timothy C Ralph, Jonathan P Dowling, and Gerard J Milburn. Linear optical quantum computing with photonic qubits. *Reviews of modern physics*, 79(1):135, 2007.

[8] Valerio Scarani, Helle Bechmann-Pasquinucci, Nicolas J Cerf, Miloslav Dušek, Norbert Lütkenhaus, and Momtchil Peev. The security of practical quantum key distribution. *Reviews of modern physics*, 81(3):1301, 2009.

[9] Frédéric Bouchard, Khabat Heshami, Duncan England, Robert Fickler, Robert W Boyd, Berthold-Georg Englert, Luis L Sánchez-Soto, and Ebrahim Karimi. Experimental investigation of high-dimensional quantum key distribution protocols with twisted photons. *Quantum*, 2:111, 2018.

[10] Xuemei Gu, Manuel Erhard, Anton Zeilinger, and Mario Krenn. Quantum experiments and graphs ii: Quantum interference, computation, and state generation. *Proceedings of the National Academy of Sciences*, 116(10):4147–4155, 2019.

[11] Xuemei Gu, Lijun Chen, Anton Zeilinger, and Mario Krenn. Quantum experiments and graphs. iii. high-dimensional and multiparticle entanglement. *Physical Review A*, 99(3):032338, 2019.

[12] Michael A. Nielsen and Isaac L. Chuang. *Quantum Computation and Quantum Information*. Cambridge University Press, 2000.

[13] Richard Jozsa. Fidelity for mixed quantum states. *Journal of modern optics*, 41(12):2315–2323, 1994.

[14] Fernando GSL Brandao, Matthias Christandl, Aram W Harrow, and Michael Walter. The mathematics of entanglement. *arXiv preprint arXiv:1604.01790*, 2016.

[15] Zhi-Xiang Jin, Yuan-Hong Tao, Yao-Ting Gui, Shao-Ming Fei, Xianqing Li-Jost, and Cong-Feng Qiao. Concurrence triangle induced genuine multipartite entanglement measure. *Results in Physics*, 44:106155, 2023.

[16] William K. Wootters. Entanglement of formation and concurrence. *Quantum Information & Computation*, 1(1):27–44, January 2001.

[17] Vineeth S Bhaskara and Prasanta K Panigrahi. Generalized concurrence measure for faithful quantification of multiparticle pure state entanglement using lagrange's identity and wedge product. *Quantum Information Processing*, 16(5):118, 2017.

[18] Frédéric Bouchard, Duncan England, Philip J Bustard, Khabat Heshami, and Benjamin Sussman. Quantum communication with ultrafast time-bin qubits, 2022.

[19] Benjamin Brecht, Dileep V Reddy, Christine Silberhorn, and Michael G Raymer. Photon temporal modes: a complete framework for quantum information science. *Physical Review X*, 5(4):041017, 2015.

[20] L. Allen, M. W. Beijersbergen, R. J. C. Spreeuw, and J. P. Woerdman. Orbital angular momentum of light and the transformation of laguerre-gaussian laser modes. *Phys. Rev. A*, 45:8185–8189, Jun 1992.

[21] Stephen M Barnett, Les Allen, Robert P Cameron, Claire R Gilson, Miles J Padgett, Fiona C Speirits, and Alison M Yao. On the natures of the spin and orbital parts of optical angular momentum. *Journal of Optics*, 18(6):064004, 2016.

[22] Robert Fickler, Geoff Campbell, Ben Buchler, Ping Koy Lam, and Anton Zeilinger. Quantum entanglement of angular momentum states with quantum numbers up to 10,010. *Proceedings of the National Academy of Sciences*, 113(48):13642–13647, 2016.

[23] Frédéric Bouchard, Alicia Sit, Felix Hufnagel, Aazad Abbas, Yingwen Zhang, Khabat Heshami, Robert Fickler, Christoph Marquardt, Gerd Leuchs, Robert w. Boyd, and Ebrahim Karimi. Quantum cryptography with twisted photons through an outdoor underwater channel. *Opt. Express*, 26(17):22563–22573, Aug 2018.

[24] Alicia Sit, Frédéric Bouchard, Robert Fickler, Jérémie Gagnon-Bischoff, Hugo Larocque, Khabat Heshami, Dominique Elser, Christian Peuntinger, Kevin Günthner, Bettina Heim, et al. High-Dimensional Intra-City Quantum Cryptography with Structured Photons. *Optica*, 4(9):1006–1010, 2017.

[25] Mario Krenn, Manuel Erhard, and Anton Zeilinger. Computer-inspired quantum experiments. *Nature Reviews Physics*, 2(11):649–661, 2020.

[26] Mario Krenn, Mehul Malik, Robert Fickler, Radek Lapkiewicz, and Anton Zeilinger. Automated search for new quantum experiments. *Physical Review Letters*, 116(9), mar 2016.

[27] Rosanna Nichols, Lana Mineh, Jesús Rubio, Jonathan CF Matthews, and Paul A Knott. Designing quantum experiments with a genetic algorithm. *Quantum Science and Technology*, 4(4):045012, 2019.

[28] Xavier Valcarce, Pavel Sekatski, Elie Gouzien, Alexey Melnikov, and Nicolas Sangouard. Automated design of quantum-optical experiments for device-independent quantum key distribution. *Physical Review A*, 107(6):062607, 2023.

[29] Mario Krenn, Xuemei Gu, and Anton Zeilinger. Quantum experiments and graphs: Multiparty states as coherent superpositions of perfect matchings. *Physical Review Letters*, 119(24), dec 2017.

[30] Xuemei Gu, Lijun Chen, Anton Zeilinger, and Mario Krenn. Quantum experiments and graphs. iii. high-dimensional and multiparticle entanglement. *Phys. Rev. A*, 99:032338, Mar 2019.

[31] Jueming Bao, Zhaorong Fu, Tanumoy Pramanik, Jun Mao, Yulin Chi, Yingkang Cao, Chonghao Zhai, Yifei Mao, Tianxiang Dai, Xiaojiong Chen, et al. Very-large-scale integrated quantum graph photonics. *Nature Photonics*, pages 1–9, 2023.

[32] Mario Krenn, Armin Hochrainer, Mayukh Lahiri, and Anton Zeilinger. Entanglement by path identity. *Physical review letters*, 118(8):080401, 2017.

[33] Mario Krenn, Jakob S Kottmann, Nora Tischler, and Alán Aspuru-Guzik. Conceptual understanding through efficient automated design of quantum optical experiments. *Physical Review X*, 11(3):031044, 2021.

[34] Wolfgang Dür, Guifre Vidal, and J Ignacio Cirac. Three qubits can be entangled in two inequivalent ways. *Physical Review A*, 62(6):062314, 2000.

[35] DN Klyshko. Multiphoton interference and polarization effects. *Physics Letters A*, 163(5-6):349–355, 1992.

[36] A. V. Burlakov, M. V. Chekhova, O. A. Karabutova, D. N. Klyshko, and S. P. Kulik. Polarization state of a biphoton: Quantum ternary logic. *Phys. Rev. A*, 60:R4209–R4212, Dec 1999.

[37] M. F. Z. Arruda, W. C. Soares, S. P. Walborn, D. S. Tasca, A. Kanaan, R. Medeiros de Araújo, and P. H. Souto Ribeiro. Klyshko's advanced-wave picture in stimulated parametric down-conversion with a spatially structured pump beam. *Phys. Rev. A*, 98:023850, Aug 2018.

[38] Reuben Aspden, Daniel Tasca, Andrew Forbes, Robert Boyd, and Miles Padgett. Experimental demonstration of klyshko's advanced-wave picture using a coincidence-count based, camera-enabled imaging system. *Journal of Modern Optics*, 61:547–551, 03 2014.

[39] Lev Vaidman, Yakir Aharonov, and David Z. Albert. How to ascertain the values of sigma$_x$, σ_y, and σ_z of a spin-1/2 particle. *Phys. Rev. Lett.*, 58:1385–1387, Apr 1987.

[40] Xiaoqin Gao, Manuel Erhard, Anton Zeilinger, and Mario Krenn. Computer-inspired concept for high-dimensional multipartite quantum gates. *Phys. Rev. Lett.*, 125:050501, Jul 2020.

[41] Sören Arlt, Carlos Ruiz-Gonzalez, and Mario Krenn. Digital discovery of a scientific concept at the core of experimental quantum optics. *arXiv preprint arXiv:2210.09981*, 2022.

[42] Anna Dawid, Julian Arnold, Borja Requena, Alexander Gresch, Marcin Płodzień, Kaelan Donatella, Kim A Nicoli, Paolo Stornati, Rouven Koch, Miriam Büttner, et al. Modern applications of machine learning in quantum sciences. *arXiv preprint arXiv:2204.04198*, 2022.

[43] Mario Krenn, Jonas Landgraf, Thomas Foesel, and Florian Marquardt. Artificial intelligence and machine learning for quantum technologies. *Phys. Rev. A*, 107:010101, Jan 2023.

[44] Giuseppe Carleo, Ignacio Cirac, Kyle Cranmer, Laurent Daudet, Maria Schuld, Naftali Tishby, Leslie Vogt-Maranto, and Lenka Zdeborová. Machine learning and the physical sciences. *Rev. Mod. Phys.*, 91:045002, Dec 2019.

[45] Hendrik Poulsen Nautrup, Tony Metger, Raban Iten, Sofiene Jerbi, Lea M Trenkwalder, Henrik Wilming, Hans J Briegel, and Renato Renner. Operationally meaningful representations of physical systems in neural networks. *Machine Learning: Science and Technology*, 3(4):045025, 2022.

[46] Raban Iten, Tony Metger, Henrik Wilming, Lídia Del Rio, and Renato Renner. Discovering physical concepts with neural networks. *Physical review letters*, 124(1):010508, 2020.

[47] Daniel Flam-Shepherd, Tony C. Wu, Xuemei Gu, Alba Cervera-Lierta, Mario Krenn, and Alán Aspuru-Guzik. Learning interpretable representations of entanglement in quantum optics experiments using deep generative models. *Nature Machine Intelligence*, 4(6):544–554, jun 2022.

[48] Romi Lifshitz. Quantum deep dreaming: A novel approach for quantum circuit design. *arXiv preprint arXiv:2211.04343*, 2022.

[49] Cynthia Shen, Mario Krenn, Sagi Eppel, and Alan Aspuru-Guzik. Deep molecular dreaming: Inverse machine learning for de-novo molecular design and interpretability with surjective representations. *Machine Learning: Science and Technology*, 2(3):03LT02, 2021.

[50] Alireza Seif, Mohammad Hafezi, and Christopher Jarzynski. Machine learning the thermodynamic arrow of time. *Nature Physics*, 17(1):105–113, 2021.

[51] Frank Schindler, Nicolas Regnault, and Titus Neupert. Probing many-body localization with neural networks. *Physical Review B*, 95(24):245134, 2017.

[52] Michael A Nielsen. *Neural networks and deep learning*, volume 25. Determination press San Francisco, CA, USA, 2015.

[53] Ian Goodfellow, Yoshua Bengio, and Aaron Courville. *Deep Learning*. MIT Press, 2016. http://www.deeplearningbook.org.

[54] Berthold-Georg Englert and Yakir Aharonov. The mean king's problem: prime degrees of freedom. *Physics Letters A*, 284(1):1–5, 2001.

[55] Akihisa Hayashi, Minoru Horibe, and Takaaki Hashimoto. Mean king's problem with mutually unbiased bases and orthogonal latin squares. *Physical Review A*, 71(5):052331, 2005.

[56] Gen Kimura, Hajime Tanaka, and Masanao Ozawa. Solution to the mean king's problem with mutually unbiased bases for arbitrary levels. *Physical Review A*, 73(5):050301, 2006.

[57] Michael Reimpell and Reinhard F Werner. Meaner king uses biased bases. *Physical Review A*, 75(6):062334, 2007.

[58] Cheng-Qiu Hu, Jun Gao, Lu-Feng Qiao, Ruo-Jing Ren, Zhu Cao, Zeng-Quan Yan, Zhi-Qiang Jiao, Hao Tang, Zhi-Hao Ma, and Xian-Min Jin. Experimental test of tracking the king problem. *Research*, 2019.

[59] Oliver Schulz, Ruprecht Steinhübl, Markus Weber, Berthold-Georg Englert, Christian Kurtsiefer, and Harald Weinfurter. Ascertaining the values of σ x, σ y, and σ z of a polarization qubit. *Physical review letters*, 90(17):177901, 2003.

[60] Thomas Durt. Quantum information, entanglement and relationships. *Cosmos*, 2(01):21–48, 2006.

[61] R F Werner. All teleportation and dense coding schemes. *Journal of Physics A: Mathematical and General*, 34(35):7081–7094, aug 2001.

[62] Jian-Wei Pan, Dik Bouwmeester, Harald Weinfurter, and Anton Zeilinger. Experimental entanglement swapping: Entangling photons that never interacted. *Phys. Rev. Lett.*, 80:3891–3894, May 1998.

[63] Stuart M Marshall, Cole Mathis, Emma Carrick, Graham Keenan, Geoffrey JT Cooper, Heather Graham, Matthew Craven, Piotr S Gromski, Douglas G Moore, Sara I Walker, et al. Identifying molecules as biosignatures with assembly theory and mass spectrometry. *Nature communications*, 12(1):3033, 2021.

[64] Mario Krenn, Robert Pollice, Si Yue Guo, Matteo Aldeghi, Alba Cervera-Lierta, Pascal Friederich, Gabriel dos Passos Gomes, Florian Häse, Adrian Jinich, AkshatKumar Nigam, et al. On scientific understanding with artificial intelligence. *Nature Reviews Physics*, 4(12):761–769, 2022.

[65] Anh Nguyen, Jason Yosinski, and Jeff Clune. Multifaceted feature visualization: Uncovering the different types of features learned by each neuron in deep neural networks. *arXiv:1602.03616*, 2016.

[66] Karen Simonyan, Andrea Vedaldi, and Andrew Zisserman. Deep inside convolutional networks: Visualising image classification models and saliency maps. *arXiv:1312.6034*, 2013.

[67] Jonathan Frankle and Michael Carbin. The lottery ticket hypothesis: Finding sparse, trainable neural networks. *arXiv:1803.03635*, 2018.

[68] Jeffrey Bub. Secure key distribution via pre-and postselected quantum states. *Physical Review A*, 63(3):032309, 2001.

[69] AH Werner, T Franz, and RF Werner. Quantum cryptography as a retrodiction problem. *Physical review letters*, 103(22):220504, 2009.

APPENDICES

Explict Form of the LOEs

We provide the explicit form of all the LOEs shown in Figure 4.1. Note that in particular that for all reflective elements, we choose to keep the $e^{i\pi/2}$ global phase. They are as follows:

Mirror:

$$\hat{U}_M \begin{bmatrix} |L\rangle \\ |D\rangle \end{bmatrix} = \begin{bmatrix} 0 & 1 \\ 1 & 0 \end{bmatrix} \begin{bmatrix} |L\rangle \\ |D\rangle \end{bmatrix} \tag{5.1}$$

Phase Shifter (PS): For a phase $\phi \in [0, 2\pi]$, we have.

$$\hat{U}_{PS} \begin{bmatrix} |L\rangle \\ |D\rangle \end{bmatrix} = e^{i\phi} \begin{bmatrix} |L\rangle \\ |D\rangle \end{bmatrix} \tag{5.2}$$

50:50 Beamsplitter:

$$\hat{U}_{BS} \begin{bmatrix} |L\rangle \\ |D\rangle \end{bmatrix} = \frac{1}{\sqrt{2}} \begin{bmatrix} 1 & e^{i\pi/2} \\ e^{i\pi/2} & 1 \end{bmatrix} \begin{bmatrix} |L\rangle \\ |D\rangle \end{bmatrix} \tag{5.3}$$

Polarizing Beamsplitter (PBS):

$$\hat{U}_{PBS} \begin{bmatrix} |H\rangle \\ |V\rangle \end{bmatrix} = \frac{1}{\sqrt{2}} \begin{bmatrix} 1 & 0 \\ 0 & e^{i\pi/2} \end{bmatrix} \begin{bmatrix} |H\rangle \\ |V\rangle \end{bmatrix} \tag{5.4}$$

Waveplate: Let

$$\hat{R}(\alpha) = \begin{bmatrix} \cos\alpha & -\sin\alpha \\ \sin\alpha & \cos\alpha \end{bmatrix} \tag{5.5}$$

denote the rotation operator over an angle $\alpha \in [0, 2\pi]$. We may describe the general waveplate with retardance δ according to

$$W(\delta) = \begin{bmatrix} e^{i\delta/2} & 0 \\ 0 & e^{-\delta/2} \end{bmatrix} \tag{5.6}$$

Note that we have chosen to ignore the global phase factor $e^{i\Delta/2}$, where $\Delta = \frac{2\pi}{\lambda}(n_e - n_o)d$ for input light wavelength λ, (extra)ordinary indices of refraction $n_{(e)o}$, and waveplate thickness d.

We may then write the waveplate operator, $W(\alpha, \delta)$, as

$$W(\alpha, \delta) = R(\alpha)W(\delta)R^{\dagger}(\alpha) \tag{5.7}$$

When $\delta = \pi$, we realize the action of a **half-waveplate (HWP)**. On the other hand, when $\delta = \pi/2$, we obtain the action of a **quarter-waveplate (QWP)**.